Biomedicine Radioengineering **Международный научно-прикладной журнал**

БИОМЕДИЦИНСКАЯ РАДИОЭЛЕКТРОНИКА

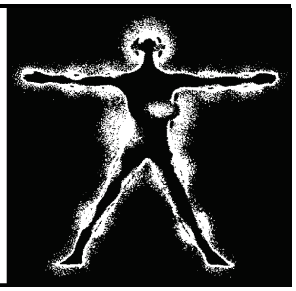

ISSN 1560-4136

6′ 2018

Выходит с 1998 г.

Включен в перечень ВАК

Proceedings of the 13th Russian German Conference on Biomedical Engineering
23.05.2018–25.05.2018, Aachen, Germany

Conference Chairs

Chair: Prof. Dr.-Ing. Dr. med. Steffen Leonhardt, Philips Chair for Medical Information Technology (MedIT), RWTH Aachen University, Germany

Co-Chair: Prof. Jaakko Malmivuo, PhD, Chair of Electronics and Medical Signal Processing (EMSP), Technische Universität Berlin, Germany

Scientific Committee

Prof. Hubertus Feußner, Technical University of Munich, Germany; Prof. Birgit Glasmacher, Leibniz Universität Hannover, Germany; Prof. Thomas Gries, RWTH Aachen University, Germany; Prof. Tobias Ortmaier, Leibniz Universität Hannover, Germany; Prof. Sergey Selishchev, National Research University of Electronic Technology, Moscow, Russia; Prof. Sergey I. Shchukin, Baumann Moscow State Technical University, Russia; Prof. Ludmila T. Sushkova, Vladimir State University, Russia; Prof. Zafar Yuldashev, Saint-Petersburg State Electrotechnical University LETI, Russia

The Russian Bavarian Conference on Biomedical Engineering (RBC) was founded 2005 in Munich. Thereafter, the conference established itself as a fruitful information exchange platform for researchers from Russia and Germany. The conference location alternated equally between cities in Russia and the southern part of Germany. After the successful 8th RBC conference in Moscow the steering committee decided to broaden the focus and establish a new conference: the Russian German Conference (RGC) on Biomedical Engineering. The goal is to serve as meeting point for information exchange and as venue for initiating bilateral Russian German research projects within the conference's scope. The first RGC on Biomedical Engineering took place in 2013 Hanover, Germany.

Previous conferences:

2016: 12th Russian-German Conference on Biomedical Engineering, 04–07.07.2016, Vladimir State University, Suzdal, Russia – Link to Proceedings
2015: 11th German-Russian Conference on Biomedical Engineering, 17–19.06.2015, RWTH Aachen University, Germany
2014: 10th German-Russian Conference on Biomedical Engineering, 25–27.06.2014, Saint Petersburg State Electrotechnical University «LETI», St. Petersburg, Russia
2013: 9th Russian-German Conference, 23–26.10.2013, Hanover, Germany
2010: 6th Russian-Bavarian Conference on Biomedical Engineering, 8–12.11.2010, Bauman Moscow State Technical University, Russia
2009: 5th Russian-Bavarian Conference on Biomedical Engineering, 01–04.07.2009, Munich, Germany
2008: 4th Russian Bavarian Conference on Biomedical Engineering, Moscow Institute of Electronic Technology, 07–11.07.2008 – Link to Proceedings
2007: 3rd Russian-Bavarian Conference on Biomedical Engineering, 02–03.07.2007, Friedrich-Alexander-University Erlangen-Nuremberg, Germany
2006: 2nd Russian-Bavarian Conference on Bio-Medical Engineering, 14–15.06.2006, Bauman Moscow State Technical University, Russia
2005: 1st Russian-Bavarian Conference on Bio-Medical Engineering, 13–14.10.2005, Munich, Germany

13-я Российско-Германская конференция по биомедицинской инженерии
23.05.2018-25.05.2018, Аахен, Германия

Организационный комитет

Руководство конференции:

Руководитель: проф. д.т.н, д.м.н., Steffen Leonhardth (С.К. Леонхард), зав. кафедрой информационных технологий в медицине, Рейнско-Вестфальский технический университет Ахена, Германия.

Заместитель: проф., к.т.н., Jaakko Malmivuo (Гакко Малмиво), Берлинский технический университет, кафедра электроники и обработки медицинских сигналов, Германия.

Научный комитет:

Проф. Hubertus FeuBner, Мюнхенский технический университет, Германия
Проф. Brigit Glasmacher (Бригит Гласмахер), Ганноверский университет имени Лейбница, Германия
Проф., Thomas Gries (Томас Гриз), Рейнско-Вестфальский технический университет Ахена, Германия
Проф. Tobias Ortmaier(Тобиас Артмаер), Ганноверский университет имени Лейбница, Германия
Проф. Селищев С.В., Национальный исследовательский университет Московский институт электронной техники, Россия
Проф. Щукин С.И., Московский государственный технический университет им. Баумана, Россия
Проф. Сушкова Л.Т., Владимирский государственный университет, России
Проф. Юлдащев З.М., Санкт-Петербургский государственный электротехнический университет ЛЭТИ, Россия

Российско-Баварская конференция по биомедицинской инженерии (РБК) была впервые проведена в 2005 г. в г. Мюнхене. С этого момента, конференция представляет собой продуктивную платформу для обмена информации учеными из России и Германии. Место проведения конференции чередовалось между городами России и южной части Германии. После успешной 8-й конференции РБК в Москве, руководящий комитет решил расширить информационное поле и организовать новую конференцию – Российско-Германскую конференцию. Основой задачей является организация встречи для обмена информацией, а также для инициирования российско-германских исследовательских проектов в рамках проводимой конференции. Первая Российско-Германская конференция впервые была проведена в 2013 г. в Германии в г. Ганновере.

Предыдущие конференции:

2016: 12-я Российско-Германская конференция по биомедицинской инженерии, 04.07. – 07.2016, Владимирский государственный университет, Суздаль, Россия
2015: 11-я Российско-Германская конференция по биомедицинской инженерии, 17.06 – 19.06.2015, Рейнско-Вестфальский технический университет Ахена, Германия
2014: 10-я Российско-Германская конференция по биомедицинской инженерии, Санкт-Петербургский государственный электротехнический университет ЛЭТИ, Санкт-Петербург, Россия
2013: 9-я Российско-Германская конференция, 23.10 – 26.10.2013, Ганновер, Германия
2010: 6-я Российско-Баварская конференция по биомедицинской инженерии, 08.11 – 12.11.2010, Московский государственный технический университет им. Н.Э. Баумана, Москва, Россия
2009: 5-я Российско-Баварская конференция по биомедицинской инженерии, 01.04 – 04.07.2009, Мюнхен, Германия
2008: 4-я Российско- Баварская конференция по биомедицинской инженерии, 07.07 – 11.07.2008. Московский институт электронной техники, Россия
2007: 3-я Российско- Баварская конференция по биомедицинской инженерии, 02.07 – 03.07.2007, Нюренбенрг, Германия
2006: 2-я Российско- Баварская конференция по биомедицинской инженерии, 14.06 – 15.06.2006, Московский государственный технический университет им. Н. Э. Баумана, Москва, Россия
2005: 1-я Российско- Баварская конференция по биомедицинской инженерии, 13.10 – 14.10.2005, Мюнхен, Германия

Contents
Содержание

2

Оценка влияния размера реверсивного шахматного паттерна и параметров биологического объекта на выделение зрительных вызванных потенциалов

Кувшинова И.С.[1], Дмитриев А.Н.[1]
МГТУ имени Н.Э. Баумана, Москва, Россия

Рассмотрена методика зрительной стимуляции с использованием различных размеров фотостимуляционной матрицы, позволяющая увеличить точность локализации нарушений функциональной активности зрительной коры. Цель работы – оценка параметров стимуляции на реверсивный шахматный паттерн и электрофизических параметров на амплитуду зрительных вызванных потенциалов.

Ключевые слова: зрительные вызванные потенциалы (ЗВП), реверсивный шахматный паттерн (РШП), режим стимуляции, светодиодная матрица, амплитуда диполя, толщина черепа.

Алгоритм выбора физической активности по данным акселерометра имплантируемого кардиостимулятора с функцией частотной адаптации

Кречетова А.В.[1], Комлева Л.С.[1], Тихомиров А.Н.[1]
МГТУ имени Н.Э. Баумана, Москва, Россия

Функция частотной адаптации улучшает качество жизни пациентов с имплантируемыми кардиостимуляторами. Однако, точность современных алгоритмов не является достаточной для полноценной жизни пациентов. Показан новый алгоритм для выбора физической активности по данным акселерометра.

Ключевые слова: частотная адаптация, кардиостимулятор, акселерометр.

Мультидиагностическое исследование послеоперационных когнитивных расстройств

Истомина Т.В.[1], Сафронов А.И.[2], Кривоногов Л.Ю.[3], Карпицкая С.А.[2], Крамм М.Н.[4], Косенок Н.Ю.[1], Шачнева Е.А.[3]
[1] Пензенский государственный технологический университет
[2] Пензенский институт повышения квалификации Министерства здравоохранения Российской Федерации
[3] Пензенский государственный университет
[4] Московский энергетический институт

Проведено исследование информативности компьютерной стабилографии совместно с электрокардиографией для изучения проявлений послеоперационной когнитивной дисфункции и поиска адекватной анестезии. Результаты исследований подтвердили возможность использования стабилографии в качестве источника количественных данных о когнитивной дисфункции и инструмента для оптимизации анестезии при лапароскопической холецистэктомии.

Ключевые слова: стабилография, электрокардиография, послеоперационная когнитивная дисфункция.

Оценка влияния силы прижатия электродной системы на сигналы нейромышечной активности

Брико А.Н., Чванова Ю.А., Кобелев А.В., Щукин С.И.
МГТУ имени Н.Э. Баумана, Москва, Россия

Представлено сравнение трех основных методов регистрации нейромышечной активности посредством регистрации электромиограммы, сигнала биоимпеданса и миотонического сигнала. Оценено влияния силы прижатия электродной системы на сигналы нейромышечной активности. Измерения проводились при изометрическом схватке на специальном стенде, конструкция которого описана в работе.

Ключевые слова: сигналы нейромышечной активности, электромиография, биоимпеданс, миотонический метод, сила прижатия электродов, изометрический схват, стенд схвата.

База видеоизображений лиц пациентов с расстройствами шизофренического спектра и контрольной группы

Латышева Е.Ю.[1], Пилипенко М.Н.[1], Бойко А.А.[1], Самородов А.В.[1], Омельченко М.А.[2], Румянцев А.О.[2], Иванова А.М.[2], Воловик Д.Д.[2]
[1] МГТУ имени Н.Э. Баумана, Москва, Россия
[2] НЦПЗ

Разработана база видеоизображений лиц пациентов, больных расстройствами шизофренического спектра, а также группы нормы. Данные заболевания характеризуются негативными симптомами в поведении, а именно в лицевой экспрессии. Описана процедура регистрации видеоизображений, указаны критерии отбора участников исследования, представлена оценка качества ручной аннотации базы.

Ключевые слова: изображение, лицо, база данных, шизофрения.

Университет Баффало, Баффало, США

Предложен метод неинвазивной оценки уровня глюкозы, основанный на двух способах измерения для увеличения точности. В ходе экспериментальных исследованиях *in-vitro* показано, что предложенный метод потенциально обладает наилучшими характеристиками среди аналогов. Для оценки уровня глюкозы использованы модели линейной регрессии и гауссова процесса, с последующим объединением результатов. Работа является основой для дальнейшего проведения экспериментов *in-vivo*.

Ключевые слова: оценка уровня глюкозы, спектроскопия в ближней инфракрасной области, эхо-импульсный ультразвук, линейная регрессия, гауссов процесс.

1

«Biomedicine Radioengineering», 2018, №5
(«Биомедицинская радиоэлектроника», 2018 г., №5)

Проведено исследование цитоплазматической электрической проводимости эритроцитов человека при разной температуре. Дана экспериментальная оценка объема клетки и содержания клеточной воды в зависимости от температуры, по которым был выполнен расчет цитоплазматической электрической проводимости. Показано, что цитоплазматическая электрическая проводимость эритроцитов может быть оценена независимо от исследования диэлектрических свойств клеток.

Ключевые слова: цитоплазматическая электропроводность, температурная зависимость, эритроциты, объем клетки.

Разработка алгоритма автоматического обнаружения ранней стадии воспаления мягких тканей пародонта на инфракрасных изображениях

Акуленко Л.О., Колпаков А.В.
МГТУ имени Н.Э. Баумана, Москва, Россия

Представлены результаты исследования эффективности методов сегментации очагов воспаления, а также результаты оценки качества алгоритма автоматического обнаружения очагов воспаления мягких тканей пародонта на инфракрасных изображениях.

Ключевые слова: воспаление пародонта, ранняя стадия, инфракрасные изображения, автоматическое обнаружение.

Алгоритм определения и ориентации одноосного приемника системы магнитного позиционирования

Геркен Е.А., Гречихин В.В.
Южно-Российский государственный политехнический университет (НПИ) имени М.И. Платова

Системы магнитного позиционирования включают подвижный приемник, осуществляющий измерение ортогональных компонент магнитного поля в исследуемой области. В работе реализован алгоритм определения положения и ориентации одноосного приемника в трехмерном пространстве в реальном времени. Показано, что габаритные размеры приемника могут быть минимизированы без потери точности измерения.

Ключевые слова: системы магнитного позиционирования, одноосный приемник, магнитный поток.

Математическое моделирование потоков электроаэрозолей при лечении ожогов

Карпухин В.А., Мустафина К.С., Климиашвили Г.С.
МГТУ имени Н.Э. Баумана, Москва, Россия

Обоснована актуальность разработки аппарата местной электроаэрозольной терапии ожогов, обеспечивающего направленный поток электроаэрозоля на ожог и позволяющего регулировать его скорость. Исследовано влияние параметров рабочей камеры на поток с целью повышения эффективности терапии. Разработаны геометрическая и математическая модели рабочей камеры. В результате вычислительного эксперимента определены параметры рабочей камеры, при которых достигается максимальный поток.

Ключевые слова: аэрозоль, электроаэрозоль, ожоги, моделирование.

Экспериментальное исследование механических свойств материалов для физического моделирования тканей

Хайдукова И.В., Беликов Н.В., Резванова А.М., Саврасов Г.В.
МГТУ имени Н.Э. Баумана, Москва, Россия

Метод физического моделирования позволяет более точно оценить влияние хирургического лечения на ткани по сравнению с аналитическим и конечным элементным моделированием. Наиболее точное моделирование механических свойств биологической ткани возможно путем выбора наиболее подходящего материала определенной концентрации. Исследована зависимость модуля Юнга от концентрации для желатина и силикона. Данные для всех концентраций были аппроксимированы. Результаты позволяют более точно выбирать необходимую концентрацию для моделирования конкретной ткани.

Ключевые слова: физическая модель, механические свойства, фантом, одноосное растяжение, силикон, желатин.

Подход к индивидуальному моделированию гемодинамики у пациента с учетом биомеханических свойств церебральной артерии

Фролов С.В.[1], Синдеев С.В.[1], Потлов А.Ю.[1], Липш Д.[2]
[1] Тамбовский государственный технический университет

«Biomedicine Radioengineering», 2018, № 7
(«Биомедицинская радиоэлектроника», 2018 г., №7)

"Biomeditsinskaya radioelektronika" (Biomedicine Radioengineering) is a scientific and technical journal devoted to biomedicine technologies and electromagnetic oscillations influence on biological objects. Established in 1998.
Полный список опубликованных в журналах статей, а также аннотации к ним Вы найдете на нашем сайте http://www.radiotec.ru

РАДИОТЕХНИКА

Учредитель ООО «Издательство «Радиотехника». Свидетельство о регистрации № 016200 от 10 июня 1997 г.
Сдано в набор 16.04.2017. Подписано в печать 10.05.2018. Печ. л. 8,75. Тираж 500. Изд. № 76.

107031, Москва, К-31, Кузнецкий мост, д. 20/6. Тел./факс +7(495)621-4837
info@radiotec.ru

Дизайн и допечатная подготовка ООО «САЙНС-ПРЕСС».
Отпечатано с предоставленных готовых файлов в полиграфическом центре ФГУП «Издательство «Известия». 127254, ул. Добролюбова, д. 6. Контактный телефон: (495)650-38-80. Заказ №

ISSN 1560-4136

Methods of investigation parameters of plasma of glow discharge lasers

A.S. Kiselev[1], E.A. Smirnov[1]
[1]Saint Petersburg Electrotechnical University "LETI", Professor Popov str. 5, Saint Petersburg, Russia
Contact: askiselev@etu.ru

Introduction

Gas-discharge devices are used widely in various fields of science and technology. The high prevalence of such devices is due to the wide variety of design solutions associated with the type of discharge flowing in the device. Among of such devices a special place is occupied by instruments with an extended positive column of a glow discharge. Glow discharge lasers belong to such devices. Glow discharge lasers are used actively for technological, metrological and medical purposes.

Gas-discharge lasers, including glow discharge lasers, are not only widespread but also quite complex devices in structure and manufacturing technology. From this point of view and taking into account the economic reality, it is quite logical to find ways to increase the service life of the gas-discharge lasers used, and to restore active elements in the event of complete loss of generation. The relatively short life of lasers makes this problem even more urgent. Possible reasons for the complete or partial failure of gas-discharge lasers are: a disturbance in the operation of the power source; increase in the level of losses in the optical resonator; reduction of amplifying in the active element of the laser. The service life of power supplies is much higher than that of active elements. In optical resonators, the main causes of a noticeable reduction in radiation power are the degradation and contamination of mirrors and Brewster's windows. The main reason for the failure of the active element is the degradation of the active medium due to the leakage of atmospheric gases, gas desorption by elements of construction, the absorption of the working gas by the shell, by the electrodes and their spray products, and the diffusion of the working gas through the envelope.

Glow discharge lasers, which include CO2 and He-Ne lasers, are used in surgery, ophthalmology, laser therapy. For the effective use of such lasers, one must know their behavior in dynamics. Also, due to the limited lifetime of such lasers, the question of replacing the gas mixture is very relevant.

Determination of the plasma parameters of a glow discharge is an important task in the design and analysis of the gas discharge devices [1]. Of particular interest is the determination of the parameters of the discharge occurring in long tubes, for example, in gas discharge lasers. One of the main characteristics that defines the behavior of the discharge gap in the circuit is the current-voltage characteristic (CVC). The CVC allows judging the state of the active environment, in particular, the degree of leakage of the atmospheric gases. In addition, the form of the CVC has a significant influence on the dynamic properties of the discharge.

Due to physical and constructive features, the laser radiation has a temporary instability due to the influence of various factors. Therefore glow discharge lasers are used in along with radiation power stabilization systems.

Instability of laser radiation parameters

Methods for stabilizing the power of laser radiation are classified on passive and active. In practice are used often active methods. Passive methods stabilizing do not take into account all the factors affecting the instability of the laser radiation power. Active stabilization methods assume negative feedback. One of the options for stabilizing the power of laser radiation is adjustment the pump level. In glow discharge lasers this process reduces to modulating the discharge current. Let us assume that at the time t the laser had a power level P_0 at a current I_0, which corresponds to the point A (fig. 1). Due to external influences, the energy characteristic of the laser can shift and this current will correspond to the power $P_0 + \delta P$ (point B). The principle of current stabilization of power consists in forced changing the discharge current by such a value δI so that the radiation power level again is equal to P_0 (point C).

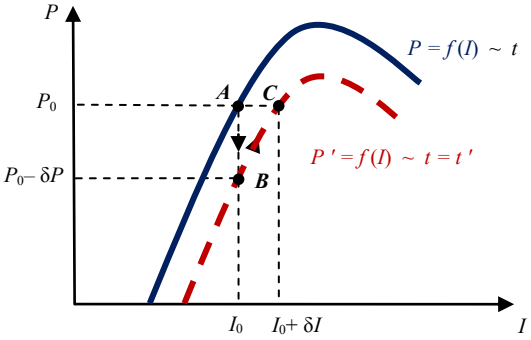

Figure 1: Explanation of the operation principle of the radiation power stabilization system

Method and equipment of experiment

To increase the accuracy of calculations of the plasma parameters of a positive column in this work was taken an attempt to refine the values of the accommodation coefficient. The idea of refining χ is based on the use of half experimental approach to the problem. Initially it was conducted a series of experiments to study the CVCs of the discharge gaps. In the experiments we used two models.

Layout 1 consisted of four discharge tubes with inner diameters of 1,1; 2; 3,4 and 5,2 mm, with movable anodes, transported by means of the magnetic actuators within the length of positive column 0,1...0,25 m (fig. 2).

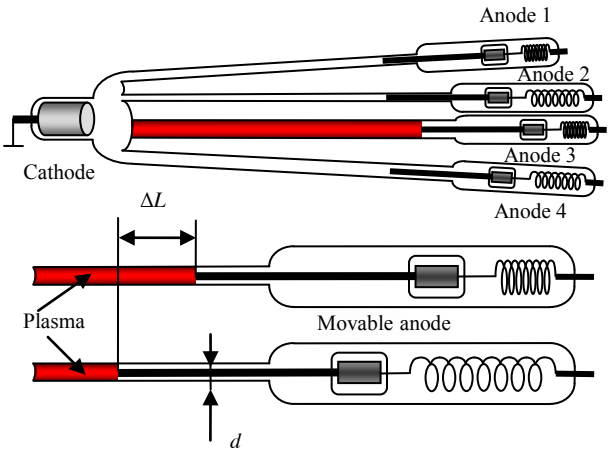

Figure 2: Layout 1 with a movable anodes

Layout 2 is a multianode tube with an inner diameter of 6,5 mm with the possible values of the active medium length 1,3; 1,12; 0,98; 0,78, 0,61; 0,47 and 0,35 m. In addition, layout 2 has an optical resonator and therefore the discharge gap can be used as the active medium of a He-Ne laser (fig. 3).

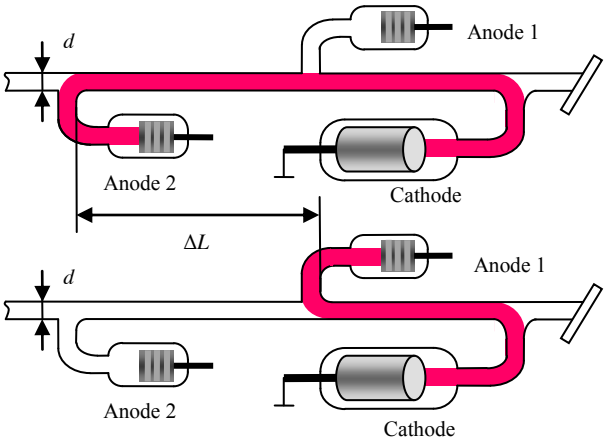

Figure 2: Layout 2 with several anodes

Layout 3 consisted of four discharge tubes with inner diameters of 3; 5; 10 and 15 mm, with fixed anodes (fig. 4).

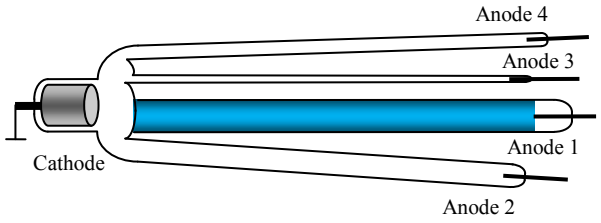

Figure 4: Layout 3 with fixed anodes

Layouts are connected with a vacuum pumping and filling system, which allows varying the gas content and operating pressure.

Equations of plasma parameters

The condition of the balance of charges for such a cylindrical plasma column can uniquely associate the average ionization frequency with coefficient of the ambipolar diffusion. Taking into account the expression for the ambipolar diffusion, frequency of ionization is defined as

$$\nu_i = \frac{b_i k (2,405)^2 T_e}{R^2 e}.$$

The average ionization rate can be written as

$$\nu_i = n_a \int_0^\infty q_i(U) \upsilon(U) f(U) dU,$$

where n_a – is the concentration of atoms; q_i – ionization cross section; $f(U)$ – Maxwell distribution function for electrons over energies. Approximations of the cross section of ionization for atoms and molecules were assumed linear. Thus, after integrating, was obtained an expression for the frequency of ionization [2]:

$$\nu_i = n_a \left(\frac{8kT_e}{\pi m_e}\right)^{0,5} \cdot \alpha_i \exp\left(\frac{-eU_i}{kT_e}\right)\left(U_i + \frac{2kT_e}{e}\right). \quad (1)$$

The transcendental equation (1) is applicable for the single component active media of the gas discharge lasers. For multicomponent gas mixtures the sum of ionization frequencies of all gases within the mixture should be used:

$$\sum_j \nu_i(j) = \frac{(2,405)^2 b_i k T_e}{R^2 e} = \frac{23,1 b_i k T_e}{e d^2}.$$

In these conditions, the average ion mobility of the gases can be calculated using the Blanc law.

Discharge CVC determines the behavior of the longitudinal potential gradient. The longitudinal potential gradient E_z in the positive column (PC) of a glow discharge is proportional to the square root of the accommodation coefficient χ of the electrons, which refers to the total energy of the electron W_e. The value of χ is important in the theory of a glow discharge PC: it characterizes the energy balance of the PC and connects the longitudinal potential gradient E_z with electronic temperature T_e [3]:

$$E_z = \frac{1,5 k T_e \sqrt{\chi}}{e \lambda_e},$$

where $\lambda_e = \lambda_{e0}/p$ – is the average free path length for electrons; p – gas pressure.

Function $\chi = f(T_e)$ can be found taking into account shares of energy lost by electrons in elastic and inelastic collisions:

$$\chi = \chi^{*} + \chi_a + \chi_w ,$$

where $\chi^{*} = 2m_e/M$ – is the average fraction of the energy lost by electron in the elastic collision; χ_a –average fraction of energy loss due to the excitation; χ_w – share of energy losses at the walls.

The described above technique was used as the basis for the program to calculate T_e. The program allows the choice of the laser type or the required gas mixture, and the display mode for the calculated information, definition of the constants and ranges of changes in the diameter of the discharge channel, the total and partial pressures of the gas components and gas temperature.

An important role in the analysis of the dynamic discharge resistance is played by the static CVC. As was said above, for the glow discharge lasers conditions the CVC has a decreasing character. In this case, the CVC can be approximated by an expression that includes the length of the discharge gap L and the longitudinal gradient of the potential E_z:

$$U_0 = U_k + aE_z L I^b ,$$

where U_k is the cathode voltage drop, which is determined by the pair of gas-cathode material; a, b - constants, depending on the kind of gas and discharge conditions. In this case, it is possible to introduce a static slope of the current-voltage characteristic:

$$\rho = dU / dI = abLE_z I^{b-1} .$$

The discharge conditions realized in glow discharge lasers correspond to the region of sharp drop in the CVC of the discharge gap. In such a case there is a transition stage from the electrons free diffusion to the ambipolar. To obtain expressions for the total dynamic resistance, one can use the method of small perturbations. In accordance with this method, the current and voltage of the discharge will, respectively, have the form: $U = U_0 + u$, $I = I_0 + i$. In these expressions I_0, U_0 are stationary values of the current and voltage at the discharge i, u are the variable components of the discharge current and voltage, where $u << U_0$, $i << I_0$.

Then the dynamic resistance will be determined by solving:

$$\frac{1}{I_0}\frac{\partial^2 i}{\partial t^2} + \frac{1}{I_1}\frac{di}{dt} + \frac{i}{I_2} = \frac{1}{U_0}\frac{\partial^2 u}{\partial t^2} + \frac{1}{U_1}\frac{du}{dt} + \frac{u}{U_2} .$$

Solution (1) was sought in the form:

$$Z_d = \frac{u_0}{i_0} e^{j\varphi} = \frac{I_0^{-1}(j\omega)^2 + I_1^{-1} j\omega + I_2^{-1}}{U_0^{-1}(j\omega)^2 + U_1^{-1} j\omega + U_2^{-1}} . \qquad (2)$$

Results

Using layouts, it is possible to carry out an experimental study of the current-voltage characteristics of a discharge for conditions characteristic of glow discharge lasers (fig. 5). The CVC characteristic is closely related to the longitudinal gradient potential of the discharge positive column.

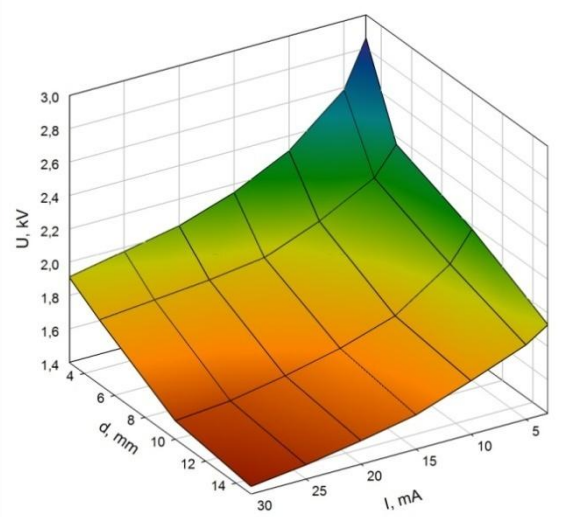

(a)

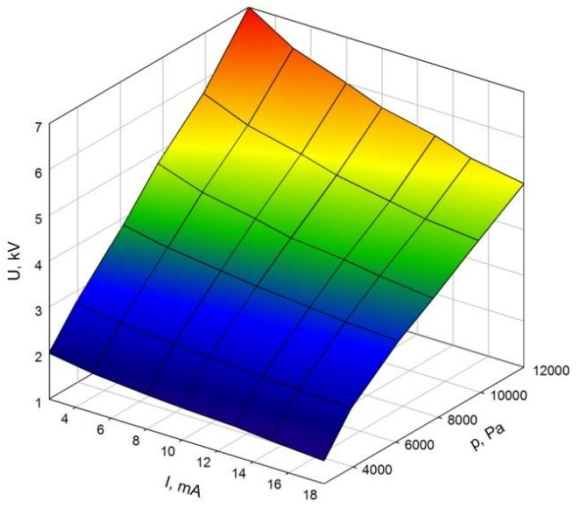

(b)

Figure 5. 3D-plots of current-voltage characteristics of the discharge: **(a)** in a carbon dioxide; **(b)** in a gas mixture CO_2:N_2:He=1:1:6

After transformation (2), an expression for the dynamic resistance of the glow discharge lasers is obtained, as the total AC resistance

$$Z_d = R(\omega) + jX(\omega) \qquad (3)$$

$$R = \frac{(I_2U_2)^{-1} + \omega^2\left[(I_1U_1)^{-1} - (I_2U_0)^{-1} - (I_0U_2)^{-1} + \frac{\omega^2}{I_0U_0}\right]}{U_2^{-2} - 2\omega^2(U_0U_2)^{-1} + \omega^2U_1^{-2} + \omega^4U_0^{-2}},$$

$$X = \frac{\omega\left[(I_1U_2)^{-1} + \omega^2(I_0U_1)^{-1} - (I_2U_1)^{-1} + \omega^2(I_1U_0)^{-1}\right]}{U_2^{-2} - 2\omega^2(U_0U_2)^{-1} + \omega^2U_1^{-2} + \omega^4U_0^{-2}},$$

where R and X is the active and reactive components of the impedance of the positive column; ω is the angular frequency. The remaining parameters depend on the discharge conditions.

To automate the process of analyzing the discharge impedance behavior, a program was developed in the MS Visual C # programming environment (fig. 6). It makes it

possible to calculate the active, reactive constituent, the impedance module, and also construct a hodograph of impedance. Before calculating the user, it is possible to select the type of gas mixture, specify the discharge conditions, the range of the discharge current and the frequency of the signal. The result of the calculation is the family of dependences of the impedance components on the frequency for different discharge currents. Each dependency family is located on a separate tab. The technique based on the use of expression (3) is the basis of the technique for modeling the impedance of plasma of glow discharge lasers.

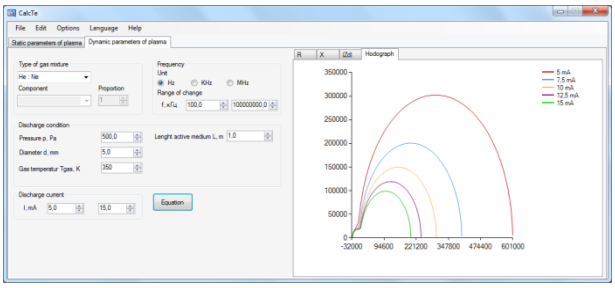

Figure 6: Program for modeling the dynamic resistance of glow discharge lasers

The results of calculating the dynamic resistance of the plasma obtained by using the developed program was analyze. At low modulation frequencies, the discharge plasma exhibits weakly inductive properties, and the impedance has a purely active value. Since under these conditions the CVC is of a falling nature, the active component of the discharge resistance $R(f, I)$ will have a negative value, and be determined by the operating point on the characteristic. With increasing frequency, the active resistance of the discharge reaches a constant value equal to the static discharge resistance. The dependence of the reactive component of the resistance $X(f, I)$ has a resonance character. At high modulation frequencies, the plasma does not have time to respond to external influences, so the reactive component of the impedance tends to zero. The advantage of the proposed method for calculating the impedance of the discharge of laser tubes is that it allows one to correctly assess the nature of the reactivity of the discharge, the presence of active resistance of both signs [4].

Conclusions

The result of the work is a set of experimental data, and theoretical models that allow calculating plasma parameters for glow discharge lasers. The calculation procedure was implemented in the form of a software package that allows performing analysis of static and dynamic plasma parameters. The results obtained can be used to develop systems for stabilizing the power of laser radiation. Also, the obtained data can be used to select the parameters of the gaseous mixture of glow discharge lasers when they are restored. These lasers can be used in medical equipment.

References

[1] Privalov V.E., Smirnov E.A. Stabilization of radiation power of glow discharge lasers and their application (review). Optical and mechanical industry. 1986. № 11, pages 52-60.

[2] Kiselev A.S., Smirnov E.A. Technique for calculating the parameters of a glow discharge plasma. Vacuum Technology and Technology. Vol. 24. No. 1, pages 56-59, 2014.

[3] Granovskii V.L. Electric current in a gas. Moscow: Science, 1971.

[4] Smirnov E.A. Dynamic characteristics of glow discharge in long tubes. News of SPbGETU "LETI". SPb .: Publishing house SPbGETU "LETI", 2013, №10, p. 6-10.

Acknowledgements

The authors of the article express their gratitude to the leadership of the Department of Electronic devices and equipment of the Saint Petersburg Electrotechnical University "LETI".

Study of the influence of the installation angle of the pedicular screw on its resistance to axial traction

Savrasov G.V.[1]., Sayfutdinova M.S.[1]., Makirov S.K.[2]., Makirov T.R.[2]

[1] Bauman Moscow state technical University, Moscow, Russia

[2] Central Clinical Hospital of the Russian Academy of Sciences, Moscow, Russia

Contact: sayfutdinova.marina@bk.ru

Introduction

Different spine diseases and injuries can damage the neural structures, leading to neurologic complications up to paresis and paralysis.. According to competent authors (Plane, 1988; Dove, 1989; Riebel, 1993; Crawford, 1994), unstable spinal fractures need a surgical treatment using ventral access and occur more then 20% of the total number of occasions. In current surgical practice, in order to reduce the pressure, the damaged spine are getting immovably fixed with a metal transpedicular system (TS), which consists of screws, beams, or plates. Screws are inserted in the body of a spinal bone above and below the damaged area along the lateral surface. After installing the required amount of components, screws are getting fastened together to form a stabilizing system. This method allows patients to sufficiently rehabilitate and return to an active full life.

This kind of restraint deteriorates due to periodic stress during its exploitation. There are several reasons: osteoporosis of the bone tissue; material of the implant system does not match the requirements for biocompatibility and bioinerticity; young's modulus of bone tissue and the young's modulus of the material of the implant structure are different.

In order to determine the maximum force of the screw's resistance during its axial extension, biomechanical tests were carried out using the pull-out scheme. Also, the goal was to determine the dependence of the traction load of the angle of inclination of the screw, installed in the spinal bone, and to evaluate the destruction of the spinal bone's body.

Materials and methods

For this study, pedicle Sryker screws (USA) were chosen; they have different geometric characteristics. The screws are an integral part of the TS, they are made of titanium alloy Ti-6Al-4V, it's composition is regulated by ISO 5832-3:1996. The vertebrae of the animals were selected as a bioobject. Structure and properties of bone tissue of the spinal bones of animals and human are similar [1-3], so the thoracic spine bone of the ram were prepared for the test - thawed at room temperature for 4-5 hours and treated with salt. To obtain the most comparable test results, vertebrae of the thoracic spine were used.

A dense cortical layer from the ventral side of the spinal bone of the ram was 1.20 mm thick, with the dorsal side of 0.88 mm thick. So that, the needle holes were made in the spinal bone bodies. The depth of breakdown was not more than 2-2,5 mm with a diameter of 1-1,5mm. The screw was installed into the hole and screwed into the spinal bone for the entire length of the thread of the leg, punching the cortical layer from the opposite side. The spinal bone with the screw was fixed in the grips of the Instron 3365 test machine so that the axis of the screw formed an angle with the axis of the load application - it was determined by means of its construction on the photo (Figure 1). Traverse speed 2mm / min.

Instron 3365 - universal testing system. We can use it to perform static testing, including tensile and compression applications.

According to ASTM F543 - 02 [4], the stress was applied vertically upwards along the X axis (Figure 2). Figure 3 shows the spinal bone in the grips of the test machine.

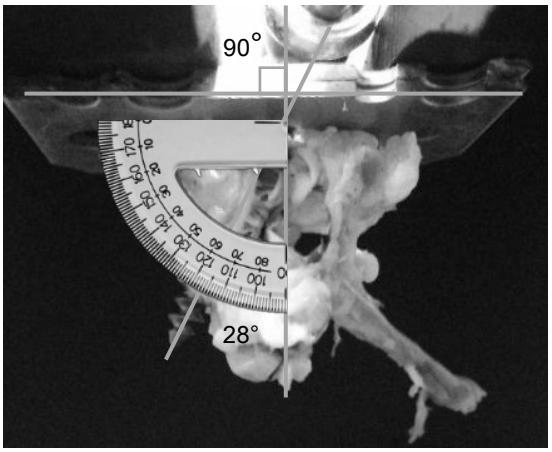

Figure 1: Position of the spinal bone with the screw in the grips of the test machine, determination of the angle of inclination.

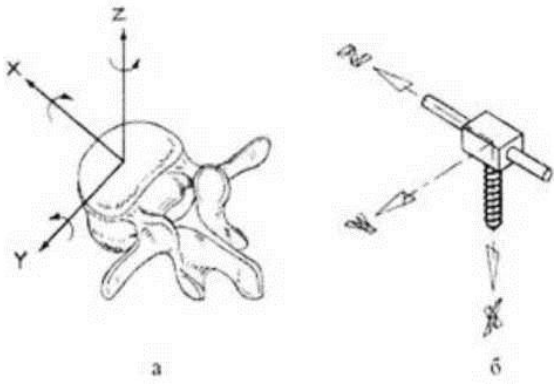

Figure 2: Global (a) and local (b) coordinate systems, which were used in the tests

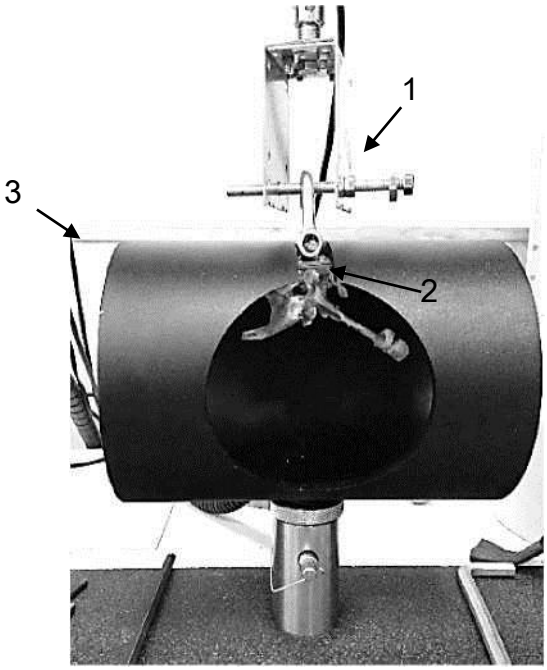

Figure 3: Vertebrae with a screw installed in the Instron grips before testing

1. – the clamp for pull-out the screws
2. – the screw inside the vertebra of an animal
3. – the clamp for fixation of vertebrae

Results

The dependence of the maximum load of traction on the angle of inclination of the screw relative to the axis of the applied force was determined. The screw is tested in the pull-out circuit. And the study of the influence of the geometric features of screws, which were mounted in the vertebra at an angle of 16 ± 2°, on their resistance to axial extension was held.

The results of the study were listed in the table 1. It shows the maximum forces for the axial extension of the screw and the inclination angles. So we can see that the strength of the resistance to axial traction decreases with an increase in the angle of inclination of the screw

Table 1: Angle of screw installation and maximum force for the screw

Characteristics / Test Number	*1*	*2*	*3*	*4*	*5*
Angle, deg.	28±0,5	18±0,5	14±0,5	13±0,5	5±0,5
Load, N	303 ±2	938 ±5	965 ±5	1073 ±5	1208 ±6

Conclusions

As a result of experimental studies it was found that the strength of the resistance to axial traction decreases with an increase in the angle of inclination of the screw. An increase in the angle of the screw installation by 9 ° led to a deterioration in the fixation and removal by 20% of the resistance to axial traction. The formed angle between the axis of the screw and the axis of its extension led to an increase in bone tissue damage.

An increase in the outer diameter of the screw leads to an increase the trauma of the vertebrae - vertebrae were cracked in tests when the screws were installed at an angle of more than 5 °.

References

[1] Chavassieux P. Effects of sodium fluoride on bone remodelling in ewes. / P. Chavassieux, P. Pastoureau, G.Boivin et. al. // Bone Miner Res, 1987. - №2: abstract 359.
[2] Pastroureau P. Effects of oophrectomy on biochemical and histological indices of bone turnover in ewes. / P. Pastroureau, M.E. Arlot, F. Caulin et. al. // J Bone Miner Res, 1989. - №4: S237.
[3] Wallach S. The bone «Quality» Problem. / Wallach S, Feinblatt J.D., Avioli L.V. // Calcified tissue international, 1992. - №51- p. 169-172.
[4] ASTM F 543 - 02 «Standard Specification and Test Methods for Metallic Medical Bone Screws». /100 Barr Harbor Drive, PO Box C700, West Conshohocken, PA 19428-2959.

The study of biomechanical characteristics of the venous wall after ultrasound exposure

A.S. Borde[1], G.V. Savrasov[1], A.V. Gavrilenko[2], A.G. Ivanova[2]

[1]Bauman Moscow State Technical University, Baumanskaya 2-ya ul. 5, Moscow, Russia

[2]Russian Scientific Surgery Center n.a. B. V. Petrovskiy, Abrikosovsky per. 2, Moscow, Russia
Contact: aenea.doerb@mail.ru

Introduction

Ultrasound ablation is one of the most perspective methods of surgical treatment of lower limbs varicose veins (LLVV). Currently, the ultrasound method is successfully used for hemorrhoids sclerosis [1].

Study of the structure of pathological venous wall after ultrasound exposure is an essential stage of ultrasound ablation technological parameters tests. The goal of this work is studying the possibility of using biomechanical characteristics as assessment criterion for evaluation of differences in pathological venous wall structure before and after ultrasound ablation.

Materials and Methods

Ultrasound ablation technological parameters tests was carried out on the samples prepared from the segments of the great saphenous vein (GSV) trunk, taken during saphenectomy in the Vascular Surgery Department of the Russian Scientific Surgery Center n.a. B. V. Petrovskiy. For the experiment were identified four groups with different modes of exposure to venous wall samples and a control group. Five groups were formed in total:
a) control group (C);
b) treatment with sclerosant solution for 60 seconds (S 60 sec);
c) contact ultrasound treatment for 60 seconds (U 60 sec);
d) ultrasound treatment with sclerosant solution for 30 seconds (U+S 30 sec);
e) ultrasound treatment with sclerosant solution for 60 seconds (U+S 60 sec).

After the stage of ultrasound ablation, the samples of the venous wall were tested for uniaxial stretching using the INSTRON 3365 machine in accordance with the method described in [2]. A series of experiments was performed in total on 110 samples of the venous wall in accordance with the developed technology, and also the histological research of the treated specimens in the Pathomorphological Department of the Russian Scientific Surgery Center n.a. B.V. Petrovskiy.

Biomechanical tests results processing was carried out in Matlab software package. During processing, the values of the maximum strain, ε_{max}, the maximum stress, σ_{max}, and the Young modulus, E, were determined for each sample (fig. 1).

Based on the presence of several comparison groups, the nonparametric tests of Kruskal-Wallis and Newman-Keuls were chosen as the statistical method of data analysis [3]. For the null hypothesis, it was assumed that the various modes of processing the GSV samples do not affect the biomechanical characteristics and the resulting differences are random.

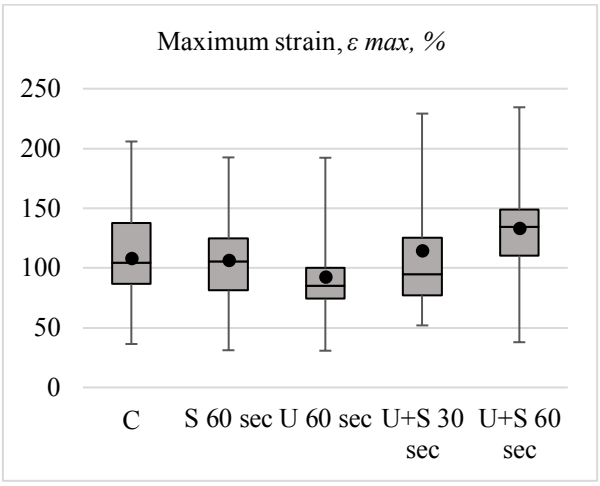

a)

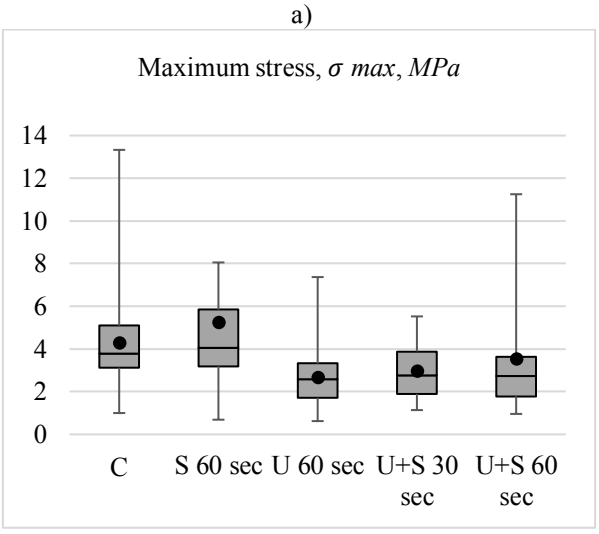

b)

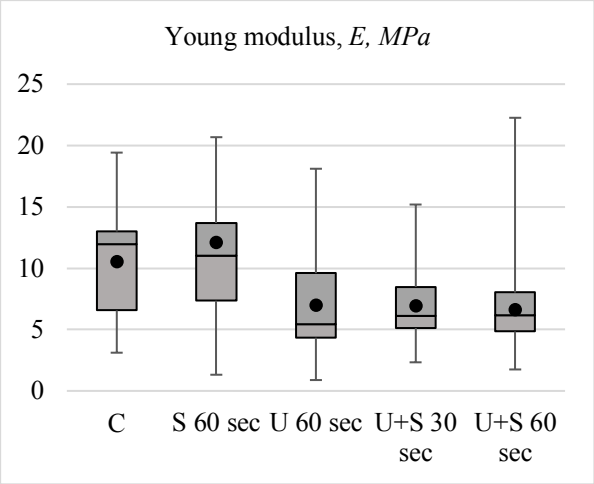

c)

Figure 1: Trends in the variation of biomechanical characteristics of the venous wall in dependence to exposure modes (see explanations in the text): a) the maximum strain; b) the maximum stress; c) the Young modulus.

Results

As a result of a multiple comparison of the GSV samples biomechanical characteristics under different modes of exposure by the Newman-Keuls test, statistically significant differences were found with p-value <0.01 between groups with different parameters of ultrasound exposure to the venous wall, a group of samples treated only with a sclerosant solution and a control group. Statistically significant differences were not found for the Young modulus of samples, treated by the contact ultrasound for 60 seconds (U 60 sec) and samples, treated by the ultrasound together with the sclerosant solution for 30 seconds (U+S 30 sec).

Conclusions

In the course of experimental studies, the influence of ultrasound on the biomechanical characteristics of the venous wall was evaluated. Based on the results of analysis of the obtained experimental data, it was shown the expediency of using biomechanical characteristics as a criterion for assessing the differences in the structure of the pathological venous wall before and after ultrasound ablation.

Using the obtained experimental data, ranges of biomechanical characteristics corresponding to different modes of exposure to venous wall can be determined. Thereby, biomechanical tests can be used as an alternative to histological studies.

References

[1] Soloviev O.L., Savrasov G.V., Soloviev A.O. Sclerosing treatment of hemorrhoids with ultrasound effect - 2002. - P. 1-10.

[2] Savrasov G.V., Bashlai A.P., Belikov N.V. Features of biomechanical studies in the pathological lesion of the blood vessels wall. // Digest of the 15th scientific and technical conference "Medico-technical technologies for the protection of health" (Portugal, Madeira Island, September 20-27, 2013). M: Publishing House: SRI RL Bauman Moscow State Technical University, 2013. P. 133-137.

[3] Glanc S. Medicobiological statistics. M.: Praktika 1999; 429 p.

SOLID ANGLE FRACTION IN SINGLE-PHOTON EMISSION TOMOGRAPHY

A.Yu. Lysenko, S.A. Tereshchenko

National Research University of Electronic Technology "MIET", Bld. 1, Shokin Square, Zelenograd, Moscow, Russia
Contact: lysenko-ay@yandex.ru

Introduction

Modern tomography is a powerful tool for visualization of internal structures of opaque objects [1-6]. Two classes of tomography are known: transmission computed tomography (TCT) and emission computed tomography (ECT). In TCT the object under investigation is irradiated by an external radiation. This radiation passed through the object and partially attenuated is registered by a detector. Initial information for a reconstruction, called projections, is formed in accordance with the detector data. The projections in TCT are Radon transform (RT) for a spatial distribution of the absorption coefficient. The absorption coefficient spatial distribution is formed by the inverse Radon transform (IRT).

In ECT the spatial distribution of radiation sources (radionuclide atoms) is reconstructed. The ECT exists in two main forms. First one is single-photon emission computed tomography (SPECT) and the second one is positron emission tomography (PET) [5]. In SPECT, single gamma quantum originating from a decay of radionuclide atom is registered. In PET the detector register a pair of gamma quanta that arises from the annihilation of a positron, which originates from a decay of radionuclide atom.

In ECT different factors affects detector data, e.g. radiation scattering, quantum statistics, motion artifacts, etc. Among these additional factors so-called solid angle fraction (SAF) [1, 3] is very interesting. SAF is due to the solid angle in which gamma quanta fall to the elementary detector from each elementary volume of the radiation source spatial distribution (fig. 1).

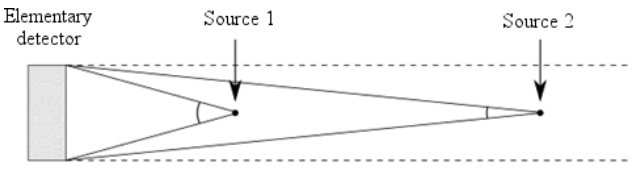

Figure 1: The factor of the solid angle fraction is proportional to the solid angle in which the radiation from an elementary source falls on an elementary detector

In SPECT the radiation is detected by plane position-sensitive detector (PSD) using heavy metal collimators. For SPECT the main physical process is the generation of radiation from the decay of radionuclide atoms. The radiation absorption, in contrary to TCT, is an additional objectionable factor that significantly deforms the detector results. Projections in SPECT are exponential Radon transform (ERT) for a spatial distribution of radiation sources rather than RT. The methods of ERT inversion were found only in 1979-1981 [8-10]. Therefore, to reconstruct the spatial distribution of radiation sources the inverse exponential Radon transform (IERT) is used. Before IERT was derived IRT was used for the reconstruction of the spatial distribution of radiation sources. To improve the quality of the reconstruction approximate methods were used for a correction of the radiation attenuation [1, 3].

Hereafter the influence of SAF to the quality of tomogram reconstruction is investigated depending on a size of the object and on the radius of the system. In addition the iterative algorithms are proposed for the correction of tomogram distortions in traditional reconstruction methods.

Materials and Methods

Let $s(x,y)$ be the spatial distribution of radiation sources in a fixed coordinate system (x,y), $s_\theta(\xi,\zeta)$ be the spatial distribution of radiation sources in a rotating coordinate system (ξ,ζ), which is rotated by an angle θ with respect to a fixed coordinate system. In SPECT the projections $p(\xi,\theta)$ taking into account SAF can be written in the following form (fig. 1a):

$$p(\xi,\theta)=\int_{l_1}^{l_2}\frac{s_\theta(\xi,\zeta)}{(R_1-\zeta)^2}e^{\mu\zeta}d\zeta. \qquad (1)$$

In (1), the factor $\frac{1}{(R_1-\zeta)^2}$ is the factor SAF for SPECT. Neglecting SAF it can be obtained

$$\tilde{p}(\xi,\theta)=\frac{1}{R_1^2}\int_{-\infty}^{+\infty}s_\theta(\xi,\zeta)e^{\mu\zeta}d\zeta=\frac{1}{R_1^2}\Re_e\{s(x,y)\}, \qquad (2)$$

where $\Re_e\{s(x,y)\}$ is the exponential Radon transform of the function $s(x,y)$. Therefore in SPECT in order to reconstruct the radiation sources spatial distribution the inverse exponential Radon transform $\Re_e^{-1}\{\bullet\}$ is used:

$$\tilde{s}(x,y)=R_1^2\Re_e^{-1}\{p(\xi,\theta)\}, \qquad (3)$$

where $\tilde{s}(x,y)$ is an estimation of the reconstructed function $s(x,y)$.

It is possible to estimate the influence of SAF comparing original $s(x,y)$ and reconstructed $\tilde{s}(x,y)$. It is interesting to investigate this influence depending on the maximum size of the object and on the radius R_1 of the plane PSD (fig. 2).

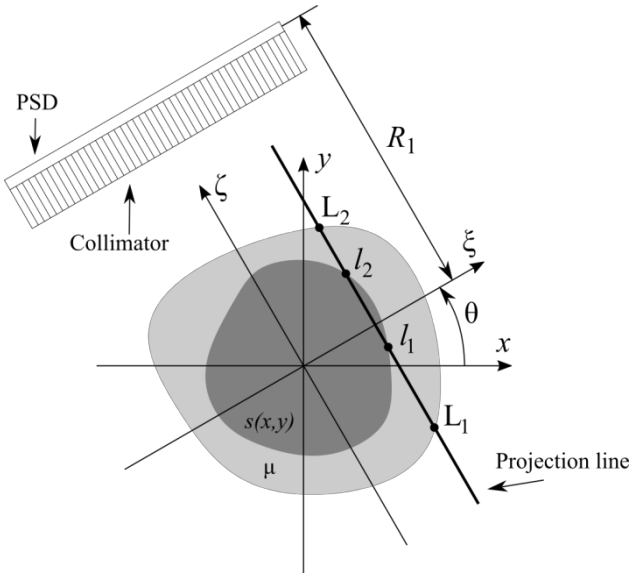

Figure 2: Scheme of measurements in SPECT: L_1, L_2 are the points of the projection line at outer boundaries of the object, l_1, l_2 are the points of the projection line at boundaries of the radiation sources distribution, R_1 is the radius of the plane PSD

To estimate the reconstruction quality a criterion U was chosen, which is the uniform deviation of the reconstructed distribution of radiation sources from the true one:

$$U = \frac{\sum_{i=1}^{N_x}\sum_{j=1}^{N_y}\left|s_{ij} - \tilde{s}_{ij}\right|}{\sum_{i=1}^{N_x}\sum_{j=1}^{N_y}\left|s_{ij}\right|}, \qquad (4)$$

where s_{ij} is the discrete version of the true spatial distribution $s(x_i, y_j)$ of the radiation sources at the point (x_i, y_j), $\tilde{s}_{ij}$ is the discrete version of the reconstructed spatial distribution $\tilde{s}(x_i, y_j)$ of the radiation sources at the point (x_i, y_j), N_x is the number of discrete image elements along the x-axis, and N_y is the number of discrete image elements along the y-axis.

The idea of iterative approaching to the solution of linear algebraic equations can be applied to integral algorithms in order to correct factors, which are not taken into account in the exponential Radon transform, for example, the SAF. In this case, the integral algorithm is used to obtain the next approximation. In this algorithm the zeroth approximation $\tilde{s}_0(x,y)$ is the image reconstructed with the IERT. Then approximate projections of the first order $p_1(\xi,\theta) = \Re_e\{\tilde{s}_0(x,y)\}$ are taking into account the SAF. The addition to the zeroth approximation is calculated with the difference between the initial projections $p(\xi,\theta)$ and approximate projections $p_1(\xi,\theta)$ as $\Delta s_1(x,y) = \Re_e^{-1}\{p(\xi,\theta) - p_1(\xi,\theta)\}$. The first approximation is calculated as $s_1(x,y) = s_0(x,y) + \Delta s_1(x,y)$. Further, it can be calculated approximate projections of the second order $p_2(\xi,\theta) = \Re_e\{\tilde{s}_1(x,y)\}$, the second-order addition $\Delta s_2(x,y) = \Re_e^{-1}\{p(\xi,\theta) - p_2(\xi,\theta)\}$, and the second approximation $s_2(x,y) = s_1(x,y) + \Delta s_2(x,y)$. Such iterations can be repeated an unlimited number of times. The criterion for the termination of the iterative process can be the smallness of the change in the tomogram in comparison with the previous iteration in accordance with criterion (4).

To improve the convergence of the iterative process, we can additionally use the idea of the correction matrix. This method was proposed for a correction of the radiation absorption in SPECT when the inverse exponential Radon transform had not been found [8]. In our case, the elements of the correcting matrix at each point of the object will characterize the distortions introduced not by radiation absorption, but by SAF.

In order to find a correction matrix, consider the reconstruction of a point radiation source with a unit intensity located at a point (x_0, y_0) with and without SAF. Then the initial distribution of radiation sources is $s_0(x,y) = \delta(x - x_0)\delta(y - y_0)$, where $\delta(\bullet)$ is the Dirac delta function. It can be obtained $p(\xi,\theta) = \frac{\delta(\xi - \xi_\theta^2)}{(R_2 - \zeta_\theta)^2} e^{\mu\zeta_\theta}$ for the projections with SAF and $\tilde{p}(\xi,\theta) = \frac{\delta(\xi - \xi_\theta^2)}{R_2^2} e^{\mu\zeta_\theta}$ for the projections without SAF, where $\xi_\theta = x_0\cos\theta + y_0\sin\theta$, $\zeta_\theta = -x_0\sin\theta + y_0\cos\theta$. Using the filtered back projection method with the filter function $h_1(\xi)$ for reconstruction it can be obtained for the reconstructed distribution at the point (x_0, y_0): $s(x_0, y_0) = h_1(0)\int_0^{2\pi} \frac{e^{\mu\zeta_\theta}}{(R_1 - \zeta_\theta)^2} d\theta$ with SAF and

$\tilde{s}(x_0, y_0) = \frac{h_1(0)}{R_1^2} \int_0^{2\pi} e^{\mu\zeta_\theta} d\theta$ without SAF. Let us define the element of the correction matrix at the point (x_0, y_0) as $c(x_0, y_0) = \frac{\tilde{s}(x_0, y_0)}{s(x_0, y_0)}$. Then for an arbitrary point (x_0, y_0):

$$c(x_0, y_0) = \frac{1}{R_1^2} \sum_{i=1}^{N} e^{\mu\zeta_{\theta_i}} \Bigg/ \sum_{i=1}^{N} \frac{e^{\mu\zeta_{\theta_i}}}{(R_1 - \zeta_{\theta_i})^2}, \quad (5)$$

where θ_i is the discrete value of the rotation angle θ and N is the number of discrete values of the rotation angle.

Results and Discussion

For our study the distributions of radiation sources were selected of two next types:

1) disk distribution with amplitude s_0, which is homogeneous in the interior of the circle with radius R_0 centered at the coordinate origin (fig. 3);

2) more complex distribution like Shepp-Logan phantom in the interior of the circle with the same radius R_0 (fig. 4).

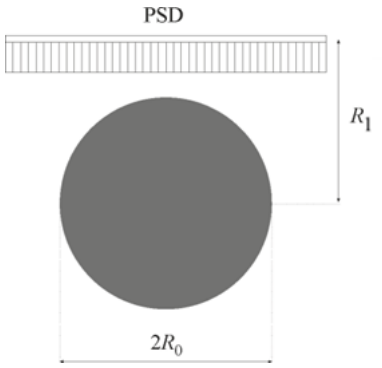

Figure 3: Disk distribution

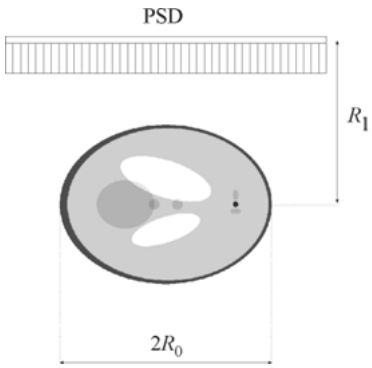

Figure 4: Distribution like Shepp-Logan phantom

The SAF factor influences significantly to the reconstruction accuracy in emission tomography. In general, taking into account SAF, the tomogram reconstruction accuracy is improved when the size of the object is decreasing and the PSD radius in SPECT is increasing. The influence of SAF is stronger for simpler objects compared more complex objects.

The proposed iterative method correcting SAF influence improves significantly the reconstruction accuracy. The tomogram reconstruction accuracy is greatly improved after 5-10 steps of the iterative algorithm. The use of the correction matrix accelerates the convergence of the iterative algorithm.

It is interesting that the value of the reconstruction error becomes even less than in the absence of the SAF factor. This is due to the fact that the iterative algorithm corrects not only the errors associated with SAF but also other errors in the implementation of the algorithm for the inverse exponential Radon transform itself. For example, these errors are sampling errors, the inaccurate regularization of the ill-posed inverse problem, etc.

Conclusions

The proposed algorithms can be used to improve the tomogram quality if tomograph native algorithms have been utilized for the reconstruction. Moreover, the obtained results can be used to develop new software for existing tomographs.

References

[1] Image Reconstruction from Projections: Implementation and Applications. Ed. by G.T. Herman. Springer-Verlag. New York, 1979.

[2] G.T. Herman. Image Reconstruction from Projections: The Fundamentals of Computerized Tomography. Academic Press. New York, 1980.

[3] G.A.Fedorov and S.A. Tereshchenko. Computed emission tomography. Energoatomizdat. Moscow, 1990. [In Russian].

[4] S.A. Tereshchenko. Methods of computed tomography. Fizmatlit. Moscow, 2004. [In Russian].

[5] Emission Tomography: The Fundamentals of PET and SPECT. Ed. by M.N. Wernick and J.N. Aarsvold. Elsevier Academic Press. San Diego, 2004.

[6] W.A. Kalender. Computed Tomography: Fundamentals, System Technology, Image Quality, Applications. John Wiley & Sons, London, 2011.

[7] S.A, Tereshchenko, Lysenko A.Yu. and D.A. Potapov. Solid Angle Fraction in Single Photon Emission Computed Tomography. Meditsinskaya Fizika (Medical Physics), 2:38–46, 2017. [In Russian]

[8] L.T. Chang. A method for attenuation correction in radionuclide computed tomography. IEEE Tr. on Nuclear Science, NS–25:638–643, 1978.

Acknowledgements

This work was supported by the Ministry of Education and Science of the Russian Federation (agreement No. 14.584.21.0021, identifier RFMEFI58417X0021).

Animal Trials of Wearable Apparatus for Peritoneal Dialysis

N.A. Bazaev, N.I. Dorofeeva, V.M. Grinvald', B.M. Putrya, N.A. Zhilo

National Research University of Electronic Technology. Shokin Square 1, Zelenograd, Russia
Contact: PutryaBM@gmail.com

Introduction

Chronic kidney failure (CKF) is a pathological condition which can be characterized by lowering metabolite and water removal rate and insufficient organism's homeostasis [1]. In 2010 the number of patients suffering from end-stage kidney failure (ESKF) excided two million people [2], [3]. Nowadays kidney transplantation is the only method of ESKF treatment. Alas, the amount of donor kidneys is not enough to supply all patients with donor organs. Organ rejection is another problem which can occur after kidney transplantation. In view of problems listed above renal replacement therapy (RRT) is vital necessity for patient with CKF. Blood purification and ultrafiltration are the main functions of RRT. There are two widespread RRT modalities commonly used nowadays: hemodialysis (HD) and peritoneal dialysis (PD). Although both methods provide sufficient blood purification, they have the following disadvantages: hemodialysis requires about 150 liters of dialysate per procedure, thus this therapy can be performed only in specialized dialysate centers. Moreover HD can cause low blood pressure and blood clots in dialysis access. Peritoneal dialysis requires frequent (4-6 per day) exchange of spent solution for peritoneal dialysis which increases the probability of peritoneal cavity contamination. Peritonitis is the main issue of PD which causes inflammation of peritoneal cavity and makes further PD procedures impossible.

Dialysate regeneration is method of spent solution purification which can potentially solve issues listed above. One of the major challenges of dialysate regeneration is urea elimination, since this metabolite is poorly removed by sorbent materials. Alternative dialysate regeneration methods such enzymatic and electrochemical methods can be use as alternative methods for urea removal; however chemical byproducts of electrolysis and urea hydrolysis are the main disadvantages of these methods. In this case different dialysate regeneration approaches can be combined to overcome these issues. For example combination of enzymatic and sorbent methods provides adequate urea and ammonia elimination and at the same time allows maintaining dialysate ion concentration in wearable artificial kidney (WAK) [4]. Therefore different variations of dialysate regeneration methods can be potentially used in WAK technology.

In this work combination of sorption and electrochemical methods was applied as dialysate regeneration approach. Sorption method can clean waste dialysate from different organic products of patient's metabolism including nitrogen bound substrate such as uric acid and creatinine and aromatic substrates such as phenol and p-cresol [5]. This method can also control ion concentration and pH of the dialysate. However most sorbents including ion exchange resins and majority of activated carbon modification have low capacity for urea, which is the main downside of sorption method. For purpose of urea elimination electrochemical method can be applied. This method can continuously eliminate urea from the solution by means of direct anode oxidation. Urea oxidation rate depends on different parameters such as current density, active anode surface, electrode type, solution ion composition, pH of the solution etc. Ability to regenerate working electrodes and urea elimination effectiveness are the main advantages of this method. However free-chloride and chloride-bound substrates generate during electrolysis. In addition electrochemical method acidifies solution during electrolysis and changes its ion composition. Intensive gas generation should also be taken into consideration. Therefore dialysate regeneration system based on this method requires additional degassing unit, post-treatment sorbent column and pH stabilizer for a proper and save functioning. Preliminary studies of this method were performed in the following papers: [6], [7].

In this study WAK with regeneration unit based on sorbent and electrochemical methods was tested on animals.

Materials and Methods

In this work dialysate regeneration by means of sorbent and electrochemical methods was applied in animal trials. Animal trials were performed with usage of the following solutions for peritoneal dialysis: Fresenius Balance (glucose 1.5 %) and Extraneal (Baxter). Initial pH of both solutions was 5.4. Fresenius contains glucose as an osmotic agent (glucose concentration – 1.5%). Extraneal contains icodextrin as an osmotic agent. Composition of the solutions is presented in tables 1 and 2.

Table 1: Fresenius Balance (glucose 1.5 %)

Ion	Concentration, mmol/l
Calcium (Ca^{++})	1,75
Sodium (Na^{+})	134,0
Magnesium (Mg^{++})	0,5
Chloride (Cl^{-})	103,5

Table 2: Extraneal (icodextrin – 75 g/l)

Ion	Concentration, mmol/l
Calcium (Ca^{++})	1,75
Sodium (Na^{+})	133,0
Magnesium (Mg^{++})	0,25
Chloride (Cl^{-})	96

Peritoneal WAK system with described dialysate regeneration unit was tested on two dogs with weight 15 kg. Dialysate solution changed every 12 hours. Concentration of ions and nitrogen-bound substrates in dialysate was measured every hour. Scheme of the experiment is presented on figure 1.

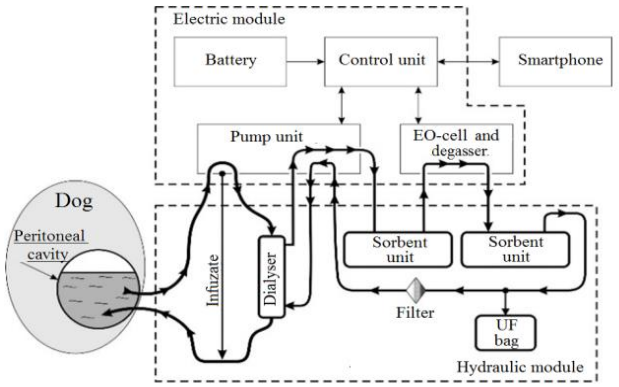

Figure 1: Experimental scheme of animal trials (UF – ultrafiltrate, EO-cell – electrochemical cell)

Experimental set-up included WAK system with dialysate regeneration module connected to dog's peritoneal cavity through catheter, control unit and receiving device (smartphone) for WAK-system control. Dialysate regeneration unit included dialyzer, sorbent units and electrolyzer. Dialyzer blocked protein and high-molecular substrates, thus preventing protein contamination of pumps and electrochemical cell. Sorbent units eliminated uric acid, creatinine and electrolysis byproducts, while electrochemical cell oxidized urea. Regenerated solution then came back to peritoneal cavity. The following materials were used in dialysate regeneration unit: sorbent units were filled with activated carbon FAS (100 g per unit); for urea elimination Ti/Pt electrodes with cumulative surface 300 cm^2 were added in EO-cell. Obtained results were compared with the following referent values [8]: urea 4–6 mmol/l, creatinine up to 176 µmol/l, uric acid up to 160 µmol/l.

Biotechnical system was divided on two parts. The first part was animal peritoneal cavity connected to dialyzer through the catheter (intracorporeal circuit). Fresh dialysate pumped into cavity. Wasted solution then came in the dialyzer where uremic metabolites diffused through the membrane to the dialysate in extracorporeal circuit. In extracorporeal circuit solution circulated through the dialysate regeneration unit. Dialysate circulation was performed by three peristaltic pumps: one in the intracorporeal circuit and two in the extracorporeal circuit.

Acute kidney disease (AKD) was provoked by infusion of mixture of 3 ml Diclophenac and 15 ml Ultravist. AKD was lately confirmed by blood test. To prevent catheter damage and animal injure the subject animal was sedated during the experiment.

Concentration of nitrogen-bound substrates, ion composition and pH were measured on biochemical analyzer Stat Fax 3300. Control of dialysate regeneration unit functioning was performed through the laptop. In particular electrochemical cell performance (such as current density and time of electrolysis) was controlled manually through laptop software.

Results

The main results of medical trials are presented on figures 2 and 3

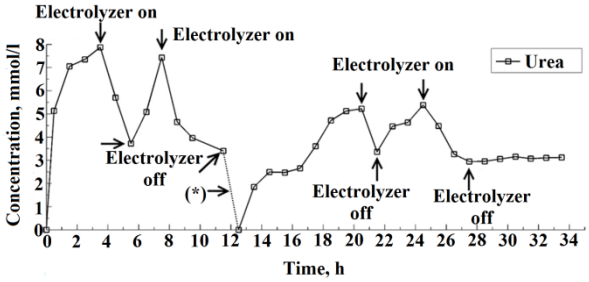

Figure 2: Urea concentration dynamics in the dialysate during WAK animal trials

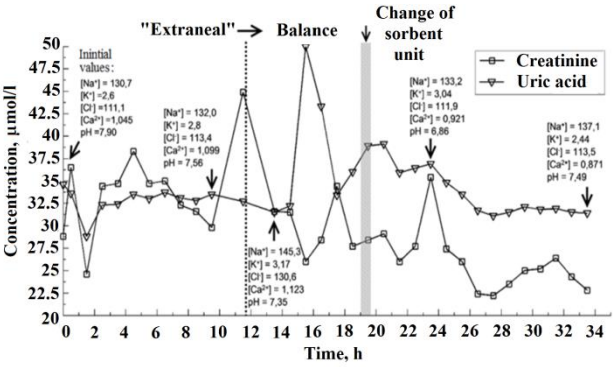

Figure 3: Creatinine and uric acid concentration dynamics in the dialysate during WAK animal trials

Developed dialysate regeneration unit effectively eliminated nitrogen-bound metabolites due to their adsorption on activated carbon and direct anodic oxidation. While creatinine and uric acid concentrations in dialysate solution did not exceed 50 µmol/l, urea concentration increase was observed during the experiment. To prevent intensive chloride byproduct generation EO cell worked only when urea concentration was close to 10 mmol/l. Overall nitrogen-bound substrates concentration stayed on physiological level during the trials and did not exceed critical values.

Necessity of electrolysis time control was the main issue of tested dialysate regeneration unit. In case of low urea concentration free-chloride and chloride-bound substrate generation becomes the main anode reaction. To eliminate these byproducts additional sorbent units are needed [9]. Moreover additional electrodes for urea detection have to be developed and applied to the system. Electrochemical cell functioning thus has to be automated. As a result electrochemical cell should work only if urea concentration in the solution gets close to or exceeds 10 mmol/l.

Another main obstacle of dialysate regeneration was poor potassium elimination. During animal trials potassium concentration increasing was observed. During the first hour of experiment potassium concentration in dialysate drastically increased from 0 to 2.6 mmol/l. After that potassium concentration steadily increased during peritoneal dialysis procedure. Twelve hours later potassium end concentration was 3.17 mmol/l. Next twelve hours after dialysate change potassium concentration continued increasing. In future version of dialysate regeneration unit specialized ion exchange resins will be needed for potassium elimination.

During dialysate regeneration chloride concentration increased which was also observed which can be explained by the following processes: ion diffusion through peritoneal membrane in the solution; ion generation during anode electro-oxidation process. The second phenomena can be explained by low urea concentration in the solution. As urea concentration drops below 6–8 mmol/l, generation of chloride gas, chloride-bound byproducts and chloride ion become the main anode process on anode surface. Thus electrochemical method can be effective in case of high urea concentrations (15 mmol/l and higher). Chloride-bound substrates generation can be decreased by EO-cell working mode control. For that development of specific urea sensor is essential.

Discussion

Overall presented dialysate regeneration unit eliminated nitrogen-bound substrates from spent dialysate and maintained their concentration on physiological level. Activated carbon and sorbent materials in general are effective in case creatinine and uric acid elimination. In addition specific types of activated carbon maintain pH and ion concentration on appropriate level. However sorbent method was ineffective in case of urea elimination. For urea concentration control electrochemical method was applied. Despite of its efficiency this method had following restrictions: chloride gas and chloride-bound substrates are the main byproducts of electrolysis, thus additional dialysate treatment was required; electrochemical method is ineffective on urea concentrations below 5 mmol/l ergo additional urea sensor for EO-cell work is needed. The main disadvantage of presented system – lack of fine-dispersed sorbents for protein elimination, which have to be added in the next step of WAK development. System also requires additional ion-exchange resins for potassium and chloride elimination

Conclusions

Presented dialysate regeneration unit for WAK-system effectively removed nitrogen-bound substrates. It did not affect dog's physiological state; however additional biocompatibility tests are required. For effective electrochemical cell functioning additional urea sensor might be needed. To remove proteins, protein-bound substrate and high-molecular substrates fine-dispersed sorbents are needed. Presented dialysate regeneration unit can be used in further WAK development.

References

[1]. Robert Thomas, Abbas Kasno, John R. Sedor. Chronic Kidney Disease and Its Complications. Prim Care // 2008. – Vol.35. – №2 – P.329–344.

[2]. Maintenance dialysis throughout the world in years 1990 and 2010. Thomas B. [et al]. Journal of the American Society of Nephrology. 2015. Vol. 26. №11. P/ 2631–2633.

[3]. Maria Jafaar. Horizon Scanning Report. Wearable Dialysis Device. // Report No: 006/2016.

[4]. Gura V., Macy A., Beizai M., Ezon C., Golper TA. Technical Breakthroughs in the Wearable Artificial Kidney (WAK) / Clinical Journal of the American Society of Nephrology // 2009 – Vol.4. – №9. – P.1441-1448.

[5]. V. M. Grinval'd, G. M. Leshchinskii, V. V. Rodin, S. I. Strelkov, A. A. Yakovleva. Development and testing of Unit for Electrochemical Oxidation of Products of Hemodialysis. Biomedical Engineering, Vol. 37, No. 2, 2003, pp. 67–72.

[6]. Bazaev N., Grinval'd V., Putrya B. Research of dialysis fluid regeneration methods. Proceedings of the 12th Russian-German Conference on Biomedical Engineering. – Suzdal.– 2016.– P. 289-292

[7]. Bazaev N.A. et al. Mathematical model of a biotechnical system for extrarenal blood purification using portable artificial kidney apparatus. Biomedical Engineering. 2016. Vol. 49. № 5. P.322–326

[8]. W.J. O'Connor. Normal Renal Function: The Excretion of Water, Urea and Electrolytes Derived From Food and Drink. Springer. 2001. P. 249 – 251.

[9]. Removal of urea in wearable dialysis device: a reappraisal of electro-oxidation / Maarten Wester [et al.] // Artificial Organs. 2014. P.1–17

The control method of peripheral venous catheters automatic insertion using force measurement

I.A. Kudashov[1], S.I. Shchukin[1]

[1] Bauman Moscow State Technical University, Moscow, Russian Federation

Contact: kudashov@bmstu.ru

Introduction

The aim of this work is to develope a feedback unit based on a strain gage force sensor integrated into a robot-assisted venipuncture system to control the rectilinear catheter insertion in order to minimize post-injection complications caused by mechanical damage to vessel wall [1-3].

When the carriage of an automated system with a installed catheter moves, the catheter exerts pressure on the strain gage force sensor, which changes its own resistance in proportion to the force acting on it.

Materials and Methods

To obtain the characteristic signals at the moment of vessel wall puncture, a laboratory stand was designed. The mechanical and electrical part of the stand includes: a carriage with guides, a rack gearing, a DC motor with GM12-N20VA gearbox (500: 1 ratio), an L293D motor driver and a signal recording unit. The signal recording unit consists of the following main elements:

- FlexiForce A201 strain gage force sensor (maximum applied force 4 N) from the Tekscan manufacturer, which is attached to the carriage [4];
- inverting voltage converter ICL7660;
- MCP602 operational amplifier for realizing an inverting amplification stage;
- Arduino Nano platform with ATmega 328 microcontroller with built-in 10-bit ADC module.

Experimental studies were conducted on different biological phantoms. A strain-gage force sensor was installed between the carriage, which drives the catheter and the catheter itself. This position allows to achieve the maximum sensitivity of the strain gage sensor to the catheter at the moment of puncture of the phantom. The used biological phantom in the first series of experimental studies is presented in Figure 1, the biological phantom is a gelatin, which simulate the soft tissues and an artificial tissue vessel as well as a sealed food layer in a gelatin.The food sheath was chosen to simulate the vessel wall, because it is structural similarity. In the second and third series of experimental studies, the soft tissues were simulated by a pork meat fragment; the blood vessel in the first case was simulated by a soft rubber tube with an internal pressure of 136 mm of water. (Mean venous pressure), in the second case - using a thin-walled tube made of polyvinyl chloride. The main principle of the three types of phantoms is to simulate the transition from soft tissue to the vascular bed with a higher density border.

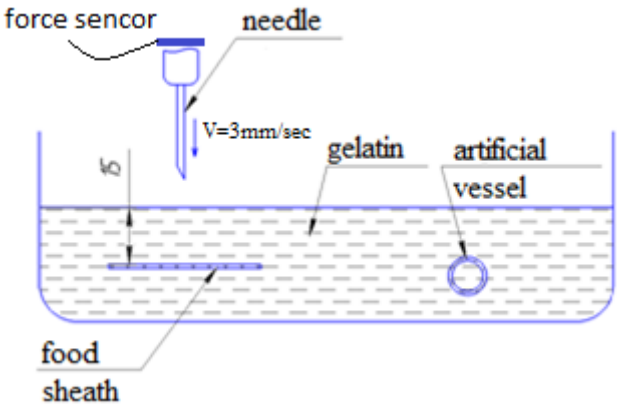

Figure 1: The image of the phantom

Analyzing the obtained signals during the third series of experiments (the characteristic form of signal is shown in Figure 2), it was difficult to uniquely determine the moment of vessel wall puncture. Therefore, it was decided not to use these signals to estimate the characteristic parameters of the signal as well as during the algorithm designing.

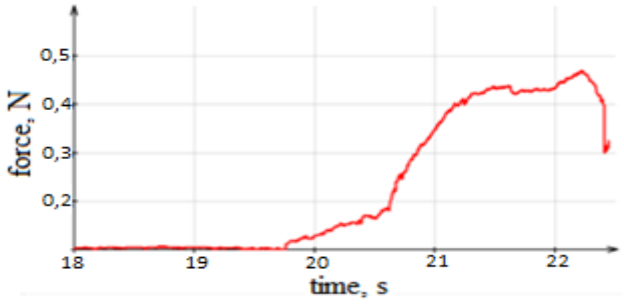

Figure 2: Characteristic signal form

The obtained signals in the first and second series of experiments had a similar shape, which is shown in Figure 3. The following signal characteristic parameters were selected for their further analysis:

- punching duration (deltaT), s;
- peak value, N;
- local minimum after puncture, N;
- the ratio of the maximum and minimum.

The results of the experiments are shown in Tables 1-3.

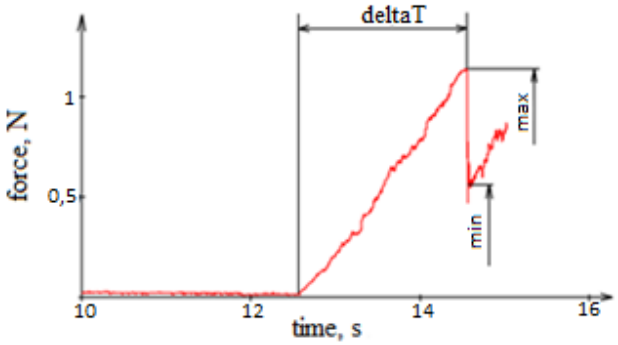

Figure 3: Selected characteristic signal parameters

Table 1: The results of the first series of experiments, the phantom: food sheath

№.	peak value (max), N	local minimum after puncture (min), N	ratio $\frac{max}{min}$	Punching duration (deltaT), sec
01:01	0,97	0,45	2,15	1,96
01:02	1,14	0,55	2,07	1,94
01:03	1,32	0,8	1,65	2,35
01:04	1,19	0,6	1,98	2,17
01:05	1,24	0,61	2,03	1,97
Average	1,17	0,6	1,98	2,08
Deviation	0,131	0,127	0,192	0,178

Table 2: The results of the second series of experiments, the phantom: artifition vessel

№.	peak value (max), N	local minimum after puncture (min), N	ratio $\frac{max}{min}$	Punching duration (deltaT), sec
02:01	0,43	0,25	1,72	1,4
02:02	1,08	0,37	2,92	1,67
02:03	0,76	0,39	1,95	1,38
Average	0,76	0,34	2,2	1,48
Deviation	0,32	0,07	0,64	0,16

Table 3: The results of the third series of experiments, the phantom: a rubber tube with an internal pressure of 136 mm of water article

№.	peak value (max), N	local minimum after puncture (min), N	ratio $\frac{max}{min}$	Punching duration (deltaT), sec
03:01	0,35	0,17	2,06	1,61
03:02	0,48	0,25	1,92	1,76
03:03	0,4	0,2	2	2,312
03:04	0,48	0,33	1,45	2,28
Average	0,43	0,24	1,86	1,99
Deviation	0,064	0,07	0,28	0,36

Results

Based on the results of the experimental studies, discrete signals were obtained, which were used to develop an algorithm for recognizing the vessel wall puncture. The algorithm is based on the analysis of the amplitude-time parameters of the obtained signals. It is shown that the applied electrical circuit for signal recording satisfies the assigned task. It is established that the received signals are qualitatively similar to the signal from the literature sources [5] and have a coincidence in order of the measured value (force acting on the force sensor). Based on the literature data, a conclusion about the permissible adjustment of the measuring equipment was made.

Conclusions

As a result of this study, a feedback module was developed to control the introduction of a peripheral catheter on the basis of a strain gage force sensor capable of detecting the moment of vessel wall puncture.

References

[1] Portable robot for autonomous venipuncture using 3D near infrared image guidance. [Electronic resource] – Access mode: https://www.ncbi.nlm.nih.gov/pmc/articles/PMC4482475/#FD7.
[2] The System Design and Evaluation of a 7-DOF Image-Guided Venipuncture Robot. [Electronic resource] – Access mode: https://www.ncbi.nlm.nih.gov/pubmed/26257588

[3] Real-time Needle Steering in Response to Rolling Vein Deformation by a 9-DOF Image-Guided Autonomous Venipuncture Robot. [Electronic resource]. – Access mode: https://www.ncbi.nlm.nih.gov/pubmed/26779381
[4] Datasheet FlexiForce A201 Sensor. [Electronic resource] URL:https://www.tekscan.com/sites/default/files/resources/FLX-A201-A.pdf
[5] Saito H., Togawa T. Detection of needle puncture to blood vessel using puncture force measurement //Medical and Biological Engineering and Computing. – 2005 –№. 2 – P. 240-244.

Diamond and Platinum Electrodes For Urea Electrochemical Oxidation

N.A. Bazaev, B.M. Putrya, Ye.V. Streltsov

National Research University of Electronic Technology. Shokin Square 1, Zelenograd, Russia
Contact: PutryaBM@gmail.com

Introduction

Dialysate regeneration process can be potentially used in wearable artificial kidney (WAK) development as a method of uremic toxins removal [1–3]. These toxins and metabolites include nitrogen-bound substrates (urea, uric acid, creatinine etc), aromatic substrates (such as p-cresol), phosphates, nitrates etc. For purpose of dialysate regeneration the following approaches can be used: sorbent method [4], electrochemical method [5, 6], enzymatic method [7] etc. Each of them has its own advantages and disadvantages and overall different combinations of methods listed above can be used for effective dialysate regeneration. Nitrogen-bound substrates removal is one of the main issues of dialysate regeneration. While sorbents can effectively remove creatinine and uric acid, they are not effective in case of urea elimination. Thus alternative solution has to be found. In this paper urea electrochemical oxidation on diamond and platinum electrodes was investigated.

This paper is dedicated to electrochemical urea oxidation method. All experiments were performed in acidified solution (pH = 5.4). The following reactions might take place on anode and cathode surfaces and in the solution during electrolysis of acidified solution:

Cathode:	Anode:
H^+, Ca^{2+}, Na^+, Mg^{2+}, Cl^-, H_2O	$(NH_2)_2CO$, H_2O, Cl^-
Reduction of H^+ and water	Oxidation of urea, Cl^- and water

C	3	$2H^+ + 2e^- = H_2\uparrow$ $2H_2O + 2e^- = H_2\uparrow + 2OH^-$	$+ 4e^-$
A	1	$(NH_2)_2CO + H_2O - 6e^- = N_2\uparrow + CO_2\uparrow + 6H^+$ $2Cl^- - 2e^- = Cl_2\uparrow$ $2H_2O - 4e^- = O_2\uparrow + 4H^+$	$- 12e^-$

Molecular formula for anode urea oxidation:

$$(NH_2)_2CO + 3H_2O + 2HCl = 6H_2\uparrow + N_2\uparrow + CO_2\uparrow + O_2\uparrow + Cl_2\uparrow$$

The following reaction might take place in the solution:

$$\overset{0}{Cl_2} + H_2O = \overset{+1}{H}\overset{}{Cl}O + \overset{-1}{H}\overset{}{Cl}$$

Urea hydrolysis in acidified medium can be presented by the following reaction:

$$(NH_2)_2CO + 2H^+ + H_2O = 2NH_4^+ + CO_2\uparrow$$

$$(NH_2)_2CO + 2HCl + H_2O = 2NH_4Cl + CO_2\uparrow$$

Urea reduction can also take place due to urea's reaction with atomic hydrogen during its generation on cathode surface:

$$2\overset{0}{H} + (NH_2)_2\overset{+4}{C}O + 2H_2O = \overset{+2}{C}O\uparrow + 2NH_3\cdot\overset{+1}{H}_2O$$

Urea oxidation can take place in the solution due to its reaction with hypochlorous acid:

$$(\overset{-3}{N}H_2)_2CO + 3H\overset{+1}{C}lO = \overset{0}{N}_2\uparrow + 3H\overset{-1}{C}l + CO_2\uparrow + 2H_2O$$

It should be emphasized that during urea electrochemical oxidation different toxic byproducts (including sodium hypochlorite) are generated and accumulated in the solution. To resolve this problem different types of materials can be used including ion-exchange resins and non-selective sorbents such as activated carbon.

Materials and Methods

In this work dialysate regeneration by means of electrochemical oxidation method has been investigated. Effectiveness of electrochemical dialysate regeneration depends on multiple factors, such as initial ion composition of dialysate solution, initial concentration of nitrogen-bond substrates, pH of solution, solution initial temperature, current density, electrode surface, electrode material etc [8–13]. In this article all experiments were performed in a solution for peritoneal dialysis Fresenius Balance (glucose 1.5 %). Initial pH of the solution was 5.4. The solution contains glucose as an osmotic agent (glucose concentration – 1.5%). Composition of the solution is presented in table 1.

Table 1: Fresenius Balance (glucose 1.5 %)

Ion	Concentration, mmol/l
Calcium (Ca^{++})	1,75
Sodium (Na^+)	134,0
Magnesium (Mg^{++})	0,5
Chloride (Cl^-)	103,5

The model solution contained 30 mmol l^{-1} of urea. Solution was recirculated through hermetic electrochemical cell with rate 50 ml/min. Cumulative anode surface for each electrode type was 150 cm^2. The volume of the model solution was 500 ml.

The following electrode types were chosen for experiment: smooth-platinum films deposited on titanium sub-

strate and boron-doped diamond films deposited on titanium substrate.

Preliminary cyclic voltammetry (CV) for electrode samples was studied. Experimental three-electrode cell for CV is presented on figure 1.

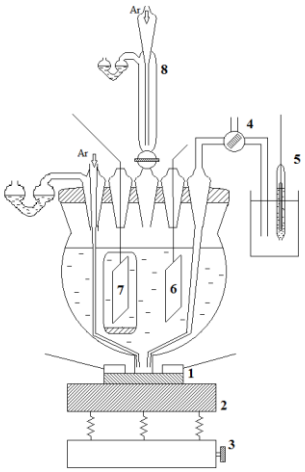

Figure 1: Three-electrode experimental cell for CV studies: 1 – electrode sample; 2 –table; 3 – lifting mechanism; 4 – salt bridge; 5 – reference electrode Ag/AgCl; 6, 7 – auxiliary electrodes; 8 – argon purge system

Cell top had five polished outlets for electrodes and argon flow system. Auxiliary electrode was separated from anode space with glass filter. Argon gas to provide inert medium inside the system was circulating through electrochemical cell. Reference electrode Ag/AgCl was linked to worked electrode through salt bridge filled with saturated solution of potassium chloride.

Experimental set-up is presented on figure 2.

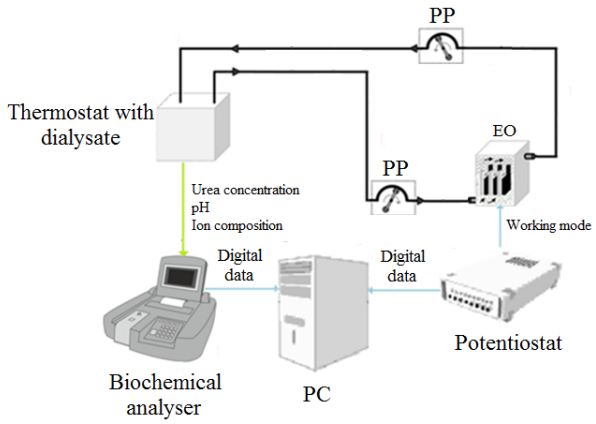

Figure 2: Experimental set-up for electrode samples testing: PP – peristaltic pump; EO – electro-oxidation cell

Urea concentration, pH and ion composition of the solution were controlled on biochemical analyzer Stat Fax 3300. Potentionstat PI-50-Pro controlled electrochemical cell working mode. All gathered data was processed and stored on personal computer. 1 ml of dialysate sample was taken every hour for urea and pH concentration measurement. Current density was 5 mA cm^{-2}.

Results

Cyclic voltammetries for platinum and diamond electrodes were studied.

Figures 3 and 4 present the cyclic voltammetries obtained with diamond and Pt electrodes in the solution for peritoneal dialysis with a scan rate of 10 mV s^{-1} for different urea concentrations.

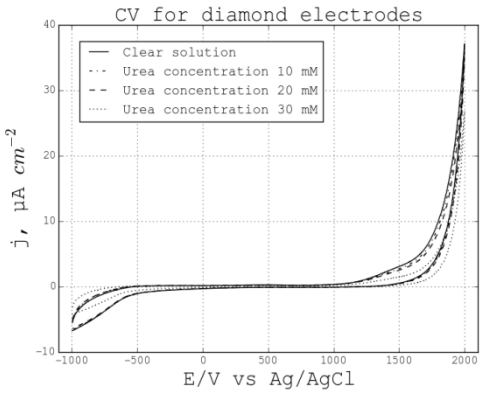

Figure 3. Cyclic voltammetry obtained with diamond electrode in the solution for peritoneal dialysis (Fresenius) for different urea concentrations (scan rate – 10 mV s^{-1})

In case of diamond electrodes, the presence of urea decreases current density in potential regions from -1000 to -500 mV vs Ag/AgCl and from 1000 to 2000 mV vs Ag/AgCl.

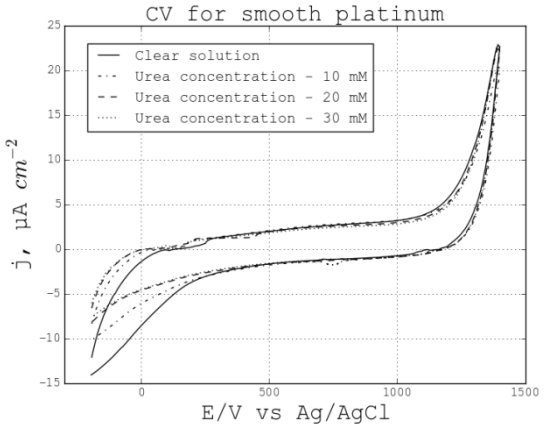

Figure 4. Cyclic voltammetry obtained with smooth platinum electrode in the solution for peritoneal dialysis (Fresenius) for different urea concentrations (scan rate – 10 mV s^{-1})

In case of cyclic voltammetry for smooth platinum electrode urea presence also altered the curve shape. Urea presence changed current density in the potential regions from -400 to 200 mV vs Ag/AgCl. At the same time, no current density change was observed on potential region from 1100 to 1400 mV vs Ag/AgCl. Observed phenomenon on both electrodes can be explained by electrode surface blockage due to urea adsorption on electrodes.

In the next stage urea oxidation rate for different electrode types was studied. Diamond and Ti/Pt electrodes were selected for this purpose. The main results of the experiment are presented on fig. 5.

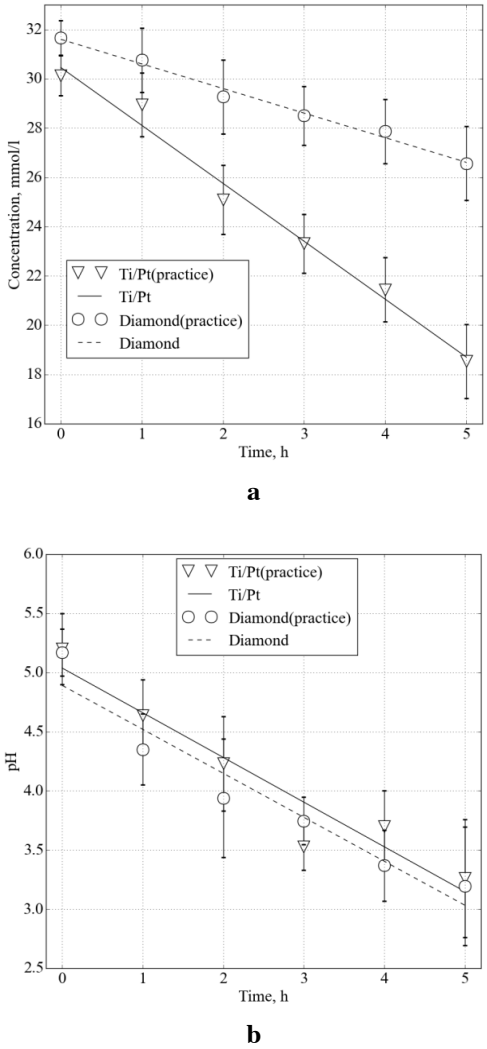

Figure 5. Results of experiment: a) urea concentration as a function of time; b) pH as a function of time

For Ti/Pt electrode urea oxidation rate was 69.54±4.3 mg h^{-1}, while for boron-doped diamond electrodes - 30.60±4.1 mg h^{-1}. The fact that platinum electrodes had higher urea elimination rate in comparison with diamond can be explained by catalytic properties of platinum.

Both diamond and platinum electrodes decreased pH of dialysate from 5.2 to 3.2. Increase of chloride was observed for both electrode samples. The highest chloride increase rate was observed for platinum electrodes (5±1 mM h^{-1}). For diamond electrodes chloride the increase rate was 2±1 mM h^{-1}. Ti/Pt produced 0.142±0.02 mg of sodium hypochlorite during the experiment, while sodium hypochlorite production was not observed for diamond electrodes.

Discussion

Cyclic voltammetries for both platinum and diamond electrodes in the solution for peritoneal dialysis have shown the tendency of urea to be adsorbed by electrode surface, which led to decrease of current density and change of the curve shape. At the same time, it was impossible to estimate what anode potential was preferable for potentiostatic urea oxidation. According to [14] experiments of potentiostatic urea oxidation mode demonstrated that this mode was ineffective due to low reaction kinetics. During the experiment, low urea oxidation rate was observed.

Galvanostatic urea-oxidation mode proved more effective than galvanostatic mode; however, it affected solution ion composition and pH and increased sodium hypochlorite generation in case of Ti/Pt. It is remarkably that hypochlorite generation was not observed for diamond electrodes. It should be also noted that ion chloride concentration increase on diamond was less intense in comparison with Ti/Pt, although diamond acidified solution with the same rate as platinum. These properties could possibly compensate low urea-oxidation rate; however, diamond electrodes were not stable and degraded during electrolysis due to high current density (5 mA cm^{-2}), which excluded diamond electrodes as a candidate for dialysate regeneration.

Ti/Pt electrodes was approved as more stable material with higher urea oxidation rate, but high sodium hypochloride generation rate, electrolysis influence on ion composition and pH of the solution should be taken into consideration. These issues can be resolved by adding ion exchange resins, activated carbon and degasser in dialysate regeneration unit.

Conclusions

Titanium diamond electrodes had lower oxidation rate and did not produce sodium hypochlorite, and at the same time they were unstable and dissolved during electrolysis which made this electrode type inappropriate for dialysate regeneration unit. Ti/Pt was the most stable material in case of electrolysis with higher urea oxidation rate and thus it is still the most prominent material for renal replacement therapy with regeneration.

Urea electro-oxidation on platinum electrodes may be potentially used in case of dialysate regeneration. However, pH stabilization of the solution is required. This issue can be resolved by adding activated carbon column. Future research will be warranted to investigate the possibilities of ion composition and pH control in closed-loop dialysate regeneration system during the process of urea electrochemical oxidation.

References

[1]. Maria Jafaar. Horizon Scanning Report. Wearable Dialysis Device. // Report No: 006/2016.
[2]. A wearable artificial kidney for patients with end-stage renal disease / Gura V. [et al.] // JCI Insight. 2016. P. 1–15.
[3]. Maintenance dialysis throughout the world in years 1990 and 2010. Thomas B. [et al]. Journal of the

American Society of Nephrology. 2015. Vol. 26. №11. P/ 2631–2633.
[4]. John WM Agar. Review Understanding sorbent dialysis systems // Nephrology. 2010. Vol. 15. P.406–411.
[5]. W. Simka, J. Piotrowski, G. Nawrat. Influence of anode material on electrochemical decomposition of urea // Electrochim. Acta. 2007. Vol. 52. P.5696–5703.
[6]. Removal of urea in wearable dialysis device: a reappraisal of electro-oxidation / Maarten Wester [et al.] // Artificial Organs. 2014. P.1–17.
[7]. A wearable haemodialysis device for patients with end-stage renal failure: a pilot study / Andrew Davenport [et al.] // Lancet. 2007. Vol. 370. P. 10
[8]. J.C. Wright, A.S. Michaels, A.J. Appleby Electrooxidation of urea at the ruthenium titanium oxide electrode // AIChe J. 1986. Vol. 32. P.1450–1458.
[9]. Electrocatalytic oxidation of urea on a sintered Ni–Pt electrode / W. Simka [et al.] // J. Appl. Electrochem. 2009. Vol. 39. P.1137–1143.
[10]. B.K. Boggs, R.L. King and G.G. Botte. Urea electrolysis: direct hydrogen production from urine. Chem // Commun. 2009. Vol. 32 P.4859–4861.
[11]. A.T. Miller, B.L. Hassler, G.G. Botte. Rhodium electrodeposition on nickel electrodes used for urea electrolysis // Appl. Electrochem. 2012. Vol. 42. P. 925–934.
[12]. V. Vedharathinam, G.G. Botte. Understanding the electro-catalytic oxidation mechanism of urea on nickel electrodes in alkaline medium // Electrochim. Acta. 2012. Vol. 81. P.292–300.
[13]. V. Vedharathinam, G.G. Botte. Direct evidence of the mechanism for the electro-oxidation of urea on $Ni(OH)_2$ catalyst in alkaline medium // Electrochim. Acta. 2013. Vol.108. P.660–665.
[14]. Electrochemical Removal of Urea from Physiological Buffer as the Basis for a Regenerative Dialysis System / Richard W. Keller [et al.] // J.Electroanal. Chem. 1980. Vol. 116. P.469–485.

Acknowledgements

This work was partly financed by the Ministry of Education and Science of the Russian Federation (project ID RFMEFI57917X0152, Contract № 14.579.21.0152, 26.09.2017).

The influence assessment of reversible chess pattern size and biological object parameters on visual evoked potential detection

I.S.Kuvshinova [1], A.N.Dmitriev[1]
[1]Bauman Moscow State Technical University, Moscow, Russian Federation
Contact: kuvirinaaa@gmail.com

Introduction

The method of visual evoked potentials (VEP) is a measurement of brain bioelectric activity recorded at scalp surface, which arises in response to visual stimulation. Various paradigms are commonly used for visual stimulation: a reversible chess pattern (RCP), a VEP in response to switching on and off a pattern, VEP in response to a flash. Each of these paradigms has its own advantages and disadvantages [1]. In this paper, we propose to use a RCP method for more stable VEP component detection [1,2].
The VEP method is used in clinical practice to assess the optic nerve condition in such cases: traumatic injury, diagnosis of hereditary and other atrophies of the optic nerve (neuritis, demyelinating diseases), diagnosis of toxic neuropathy, assessment of vision in various visual agnosias, functions in patients with impaired consciousness, perimetry and visual field disturbances: hemianopsia, cortical damage, differential diagnosis of lesions at the pre- and post-chiasmal level [2].
The main cause of visual pathway damage is brain vessels blood circulation violation (80%), brain tumors (16%), inflammatory, demyelinating and degenerative processes (4%). Most often affects the cortex of the optic path in the occipital lobe (51 %), visual irradiation (29 %) and the posterior part of the optic tract and the lateral geniculate frame (21 %). The cortex of optic path in occipital lobe (51%), visual radiance (29%) , the posterior part of the optic tract and lateral geniculate body (21%) are most often affected.

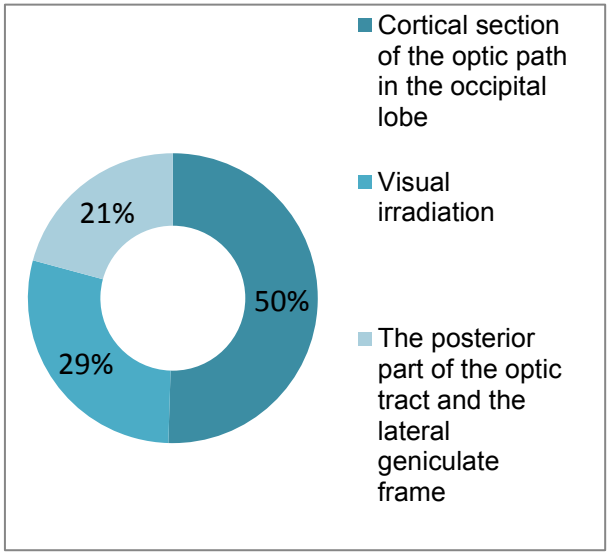

Figure 1: Statistics of lesions of different parts of the visual tract

There are specified recommendation for VEP registration [1,3,4], however, such standards do not take into account influence on the recorded VEP amplitude, which can be occurred by such bioobject parameters as: thicknesses, heterogeneities of various anatomical structures, changes in tissue conductivity under different conditions and else.
Visual stimulation using small photo stimulation matrix sizes (less than 5 °) is also a separate issue, since there is a connection between the stimulation of a certain quadrant of retina and its projection on visual cortex [5]. The development of such technique will increase the accuracy of impaired visual cortex functional activity localization.
The main goal of this work is to estimate the stimulation parameters on the RCP and electro physical parameters for the VEP amplitude.

Materials and Methods

Electrodes are placed according to the international system "10-20", ipsilateral ear electrodes were used as reference electrode; the earth electrode was installed on Nasion (Figure 2).
The EEG recording was performed using "NeuronSpectr-5". The sampling frequency is 500 Hz, the signal was filtered in the frequency band from 0.7 to 35 Hz.
The electrode-skin impedance was measured at the beginning of the experiment and it was checked that the elec-

trode-skin impedance did not exceed 20 kΩ. during the experiment.

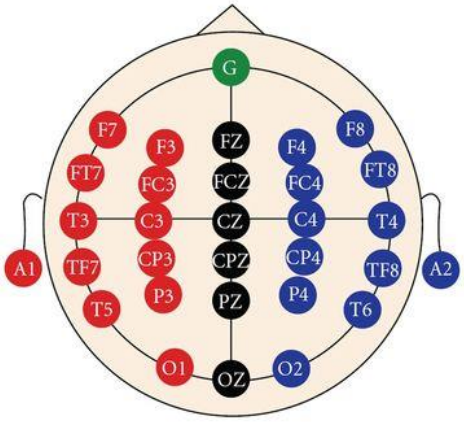

Figure 2: Schematic placement of electrodes «10-20»

In order to evaluate the optimum stimulation parameters, the signal was recorded at 3 different LED matrix sizes (Figure 3), the operating modes of which were changed using the Arduino Uno board.

Stimulation mode:

A) Matrix 3x3, the matrix dimensions is 1 ° x 1 °

B) Matrix 5x5, the matrix dimensions is 1.8 ° x 1.8 °

C) Matrix 8x8, the matrix dimensions is 3 ° x 3 °

To synchronize the LED matrix operation and the EEG registration, a PS / 2 cable was used from the electroencephalograph photo-stimulator, through which a signal was given at the RCP switching time. The EEG signal was recorded from O2A2, OzA2 - leads, where the VEP amplitude are most indicated.

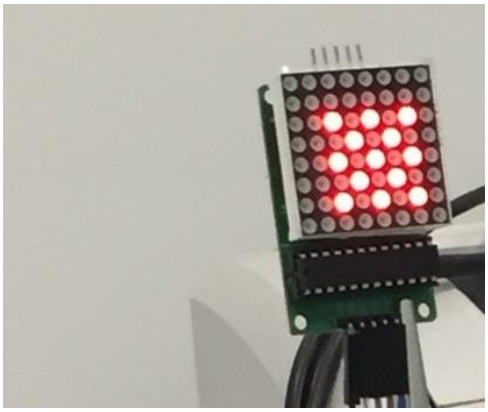

Figure 3: LED matrix in 5x5 mode.

Table 1: Experimental conditions

Age, years	20
Female or male	male
Distance to the matrix, cm	65
Room temperature, °C	24
Illumination of the room, lux	570
Noise in the room, dB	49,5
Stimulation frequency, Hz	1
Time of stimulation, s	200

To assess the influence of skull layer thickness on potential amplitude, a numerical modeling was carried out. An ellipsoidal three-layer model of the head (layers: brain-skull-scalp) has been used in this work. All ellipsoids are concentric. The corresponding semi-axis of ellipsoids are proportional, therefore the scalp layer thickness and the skull bone is constant. As a dipole, a current dipole was used. The dipole is located in the occipital region, at a distance of 2 cm from the inner surface of the skull bone. The main used parameters in the proposed model are indicated in Table 1. The dipole characteristics are taken from literature [2].

Table 2: Basic parameters of model

Title	**Value**
Length of head, m	0.24
Width of head, m	0.144
Head height, m	0.1
Skull thickness, m	0.05
Thickness of scalp, m	0.05
Specific conductivity of the scalp, $(Ohm \times m)^{-1}$	0.33
Specific conductance of bone, $(Ohm \times m)^{-1}$	1×10^{-3}
Specific conductance of brain tissue, $(Ohm \times m)^{-1}$	0.33
The position of the dipole along the x axis, m	0.1
The position of the dipole along the y axis, m	0
The position of the dipole along the z axis, m	0.01
The direction of the dipole along the x axis	1
The direction of the dipole along the y axis	0
The direction of the dipole along the z axis	0
Amplitude of a dipole, A×m	6.4×10^{-8}

Results

Figure 4 shows the visual evoked potentials recorded from O2 electrode. The graph compares the obtained signals in different stimulation modes.

The graphs clearly show the presence of positive peaks in the 100 ms region and negative in 145 ms region.

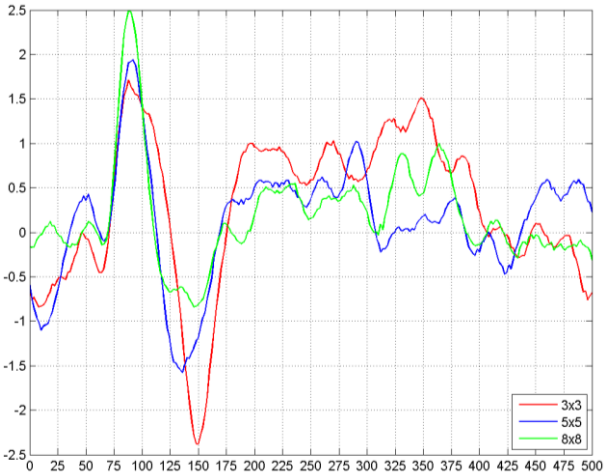

Figure 4: Dedicated signal, registered from O2A2 lead. The Y axis is the EEG amplitude in μV, the X axis is the time at the moment of applying stimulus in ms

Based on the specified parameters in Table 2, a mathematical model was constructed. Figure 5 shows the dependence of potential amplitude in the region of O1 and O2 electrodes and skull thickness. The skullt thickness parameter was ranged from 5 mm to 7 mm in 0.5 increments.

Figure 5: The electric potential amplitude dependence on skull thickness

Discussion

In all stimulation modes, the P100 and N145 peaks are clearly distinguished. The N75 peak is less significant. However, N145 peak latency is shifted for stimulation modes A. Also, for all stimulation modes, there is no increase in P100 latency, but P100 amplitude in stimulation mode A and B is significantly reduced in comparison with the amplitude in mode C. It can be concluded that under the stimulation mode C, the variability of latency decreases and the amplitude of the visual evoked potentials. This can be explained by the involvement of an increasing number of neurons with an increase in the field of visual stimulation. Thus, it is possible to localize functional disturbances in the visual cortex, changing the size and location of the stimulation zone.

According to Figure 5, it can be concluded that the potential amplitude at the location of O1 and Oz electrodes depends on skull thickness, but the changes are small, the indices vary from 2.9 to 3.7 μV, which corresponds to the amplitudes range of visual evoked potentials. The same results were obtained with the dependence of the amplitude on skin thickness and skull conduction. However, the skin conductivity does not affect the amplitude at the electrodes.

Conclusions

On the basis of the theoretical model, an insignificant effect of the skull thickness of the skull on the amplitude of the VEP was shown. The results of the experiment confirmed that with a matrix size of order of 1 °, it is possible to isolate the VEP on the RCP, but with larger matrix size c ore stable VEP amplitudes are obtained.

References

[1] J. Vernon Odom, Michael Bach, Colin Barber. ISCEV standard for clinical visual evoked potentials(update 2009). International Society for Clinical Electrophysiology of Vision in Nagoya. Documenta Ophthalmologica, 120(1):111-119, 2010.

[2] V.V. Gnezditsky. Inverse EEG problem and clinical electroencephalography (mapping and localization of brain electrical activity sources). Medpress-inform, Moscow, 2004.

[3] J. Vernon Odom, Michael Bach, Colin Barber. Visual evoked potentials standard. International Society for Clinical Electrophysiology of Vision in Nagoya. Documenta Ophthalmologica, 108(2): 115-123, 2004.

[4] J. Vernon Odom, Michael Bach, Colin Barber. ISCEV standard for clinical visual evoked potentials (update 2016). International Society for Clinical Electrophysiology of Vision in Nagoya. Documenta Ophthalmologica, 133(1): 1-9, 2016.

[5] A.V. Gustov. Practical Neurophthalmology. NGMA, Nizhny Novgorod, 2003.

Algorithm of physical activity detection according to the accelerometer data of implantable pacemaker with rate-adaptive pacing.

A.V. Krechetova, L.S.Komleva, A.N.Tikhomirov
Bauman Moscow State Technical Unirversity, Moscow, Russian Federation

Contact: Krechetovaanna1995@mail.ru

Abstract

The number of implantable pacemakers increases every year. Rate-adaptive pacing improves the quality of life of patients with implantable pacemakers. The accuracy of current algorithms is not sufficient for a productive life of patients. The object of this article is to demonstrate new algorithm of physical activity detection according to the accelerometer data.

Keywords

Rate adaptation, pacemaker, accelerometer.

1. Introduction

There is a trend towards improvement in quality of life in today's world. Rate adaptation allows patients with implantable pacemakers to bring their life as close to normal as possible. Rate responsive pacemakers allow to increase the heart rate, depending on the patient's physical load. Figure 1 illustrates how pacemaker works without rate adaptation. The frequency of the stimulating pulses remains constant during the day with changes of the physical activity intensity. Figure 2 shows the operation of a pacemaker with frequency adaptation, in this case the frequency of the stimulating impulses is adjusted to the change in physical activity.

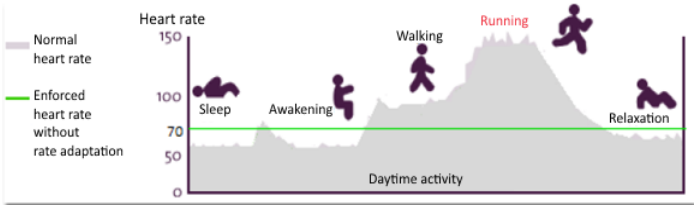

Figure 1 – Enforced heart rate without rate adaptation

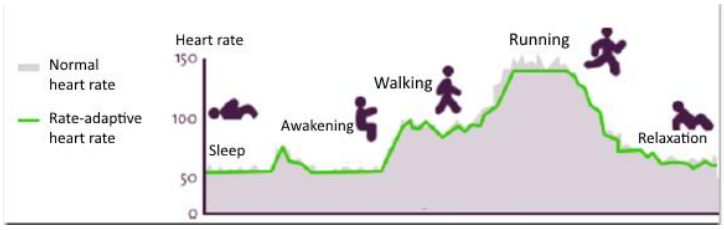

Figure 2 – Enforced heart rate with rate adaptation

This article describes the development of algorithm of physical activity detection according to the accelerometer data of implantable pacemaker. Rate adaptation is achieved by using sensors that determine the parameters related to the load and associate them with the frequency of stimulation. Methods of stimulating impulses frequency adaptation depending on various parameters were examined in the article [1]. Incorrect interpretation of passive movements continues to be a disadvantage of the developed algorithms.[2]

2. Methods and materials

2.1 Experiment description

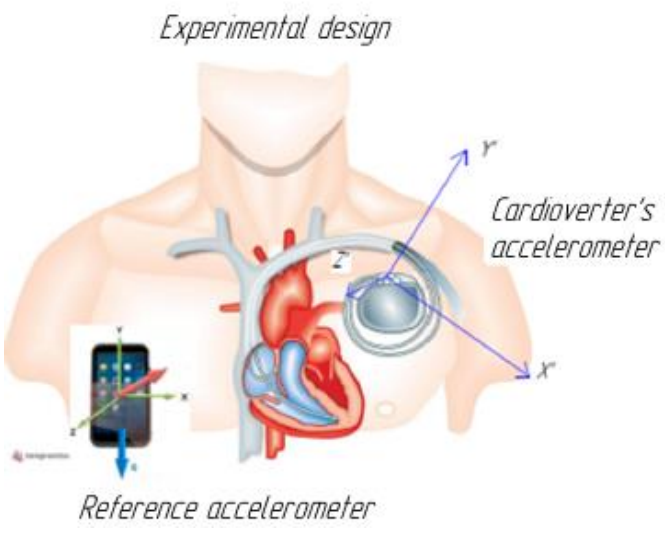

Figure 3 – Experiment setup

The accelerometer sensor was chosen for the experimentation because it directly measures physical activity, unlike other sensors, which measure only the parameters affected by physical activity. The experiment was conducted with the aim of obtaining physical activity data that was used to develop an algorithm.

Two accelerometers were used in the experiment. The first sensor required for accelerometer axes reorientation was fixed on the subject's abdomen so that its axes were directed according to the human body axes. The second sensor, which simulated the accelerometer of implantable pacemaker, was also fixed on the abdomen, but was located at an arbitrary angle in the range of 0 to 90 degrees, the axes of the second accelerometer didn't coincide with the human body axes. (Figure 3)

Accelerometers of the LIS302DL type built into a mobile phone were used for carrying out the experiment. Basic technical specifications of LIS302DL accelerometer are presented in Table 1.

Table 1

Technical characteristic	Value
Sampling frequency	50 Hz
Supply voltage	2.16 V to 3.6 V
Amplitude range of g	± 2g/± 8g

2.2 Database

A database was created according to the results of the experiment for three motion types: running, walking and stair climbing. The experiment was conducted on eight volunteers. Each database file contains data obtained from the accelerometer (time and acceleration in three axes) and the necessary parameters for the information analysis: the motion type, sex, age, weight and height of the test subject.

2.3 Accelerometer axes reorientation procedure

Axes of the implanted pacemaker accelerometer should coincide with the human body axes in order to implement the algorithm of physical activity detection. Calibration is performed by means of external accelerometer during the implantation. The direction of the vector of gravity has to coincide with the vertical axis of the implantable pacemaker accelerometer. For this purpose three experiments were carried out using the external accelerometer, whose data was taken as a reference.

The following matrix equation is used to convert the data obtained from the accelerometer:

$$A = \begin{bmatrix} X1 & X2 & X3 \\ Y1 & Y2 & Y3 \\ Z1 & Z2 & Z3 \end{bmatrix} \begin{bmatrix} X'1 & X'2 & X'3 \\ Y'1 & Y'2 & Y'3 \\ Z'1 & Z'2 & Z'3 \end{bmatrix}^{-1} \quad [3]$$

Where A - coordinate transformation matrix
X,Y,Z – reference accelerometer data
X',Y',Z' – pacemaker accelerometer data.

Computing matrix A is calculated once and loaded into the pacemaker.

Each signal from the collected database contains information from both accelerometers. All signals pass primary processing of accelerometer axes reorientation, which is necessary for further application of the algorithm of physical activity detection.

2.4 Algorithm of physical activity detection.

Threshold algorithms are used to detect the physical activity using an accelerometer sensor.

The data processing begins with dividing the signal received from the accelerometer during the experiment into 3-second intervals in order to reduce the delay time. 3-second delay is optimal, because the change in heart rate after exercise is normal within 3 seconds. [4] The threshold value determined by the experimental data for the sensor signals is 0.25g. The quantity of peaks above the threshold value is calculated. Figures 4 and 5 show peak detection signal processing at the 3-second interval.

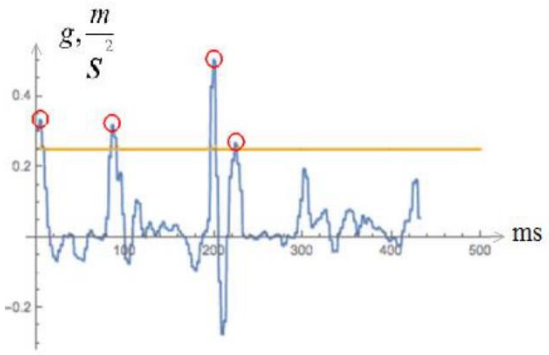

Figure 4 – Quantity of peaks for slow walking motion

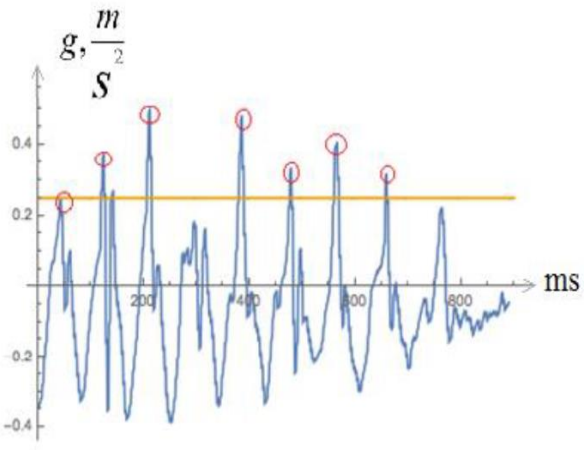

Figure 5 – Quantity of peaks for running motion

The percentage of signal counts over the threshold value to the total number of samples is calculated. This percentage describes the intervals duration above the threshold value and the acceleration increase.

Based on the results of the experiment, a space of attributes was formed for each type of physical activity.

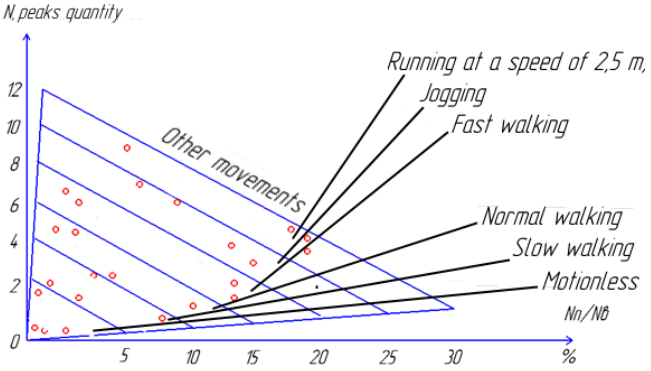

Figure 6 - Diagram of the physical activity detection
The stimulating heart rate is selected in accordance with Table 2.

Table 2 — Dependence of heart rate on physical activity [5]

Motion type	Heart rate, BPM
Slow walking	86
Normal walking	104
Fast walking	122
Jogging	135
Running at a speed of 2,5 m/s	155

3. Results

The space of attributes was formed for each type of physical activity. Another outcome of this work is the generated database. The algorithm of accelerometer axes reorientation was created, that was necessary for application of the physical activity detection algorithm. Algorithm of the physical activity detection was developed.

Table 3. Results of applying the physical activity detection algorithm

Motion type	Total intervals	Intervals recognized	Correctly recognized intervals
Relaxation	4	4	4
Slow walking	4	4	3
Normal walking	4	3	3
Fast walking	4	2	1
Jogging	4	6	4
Running at a speed of 2,5 m/s	4	5	4

The developed algorithm was tested on the collected database.

4. Discussion

As a result of the algorithm application for physical activity detection, 5 out of 24 intervals were determined incorrectly. This may be associated with small difference in the number of peaks above the threshold value for walking fast and jogging motion types. Furthermore, algorithm application errors may be related to the presence of passive movements. At the present time, the possibility is being considered of analyzing the third criterion included into the algorithm with the aim of creating a three-dimensional space of attributes model. It is also planned to add the possibility of recognizing passive movements to the algorithm.

Conclusion

This article describes the development of the physical activity detection algorithm applied with help of accelerometer sensor when using the implantable pacemaker rate adaptation. Preprocessing the data using the algorithm of accelerometer axes reorientation is explained. The features of the experiment for data collection and database formation are described. In the future, it is planned to increase the amount of movements in the database and the number of physical activity detection algorithms.

Reference list

[1] Materialy Vtorogo Vserossijskogo s"yezda aritmologov [Materials of the Second All-Russian Congress of Arrhythmologists]. Moscow, BSCCS Publ., 2007

[2] Wilfried Mullens , W. H. Wilson Tang. Telemonitoring and Sensor Technologies in Chronic Heart Failure Matthias Du- pont .2014

[3] Armin Bolz. Cardiac Pacemaker Systems. Springer-Verlag Berlin Heidelberg 2011

[4] Varma N, et al. Evaluation of ef fi cacy and safety of remote monitoring for ICD follow-up: the TRUST trial. Circulation. 2008

[5] Duperron G.A. Teoriya fizicheskoy kul'tury [Theory of physical culture]. Leningrad, 1927. 210 p.

Acknowledgements

Any acknowledgements may appear here.

Multidiagnostics study of postoperative cognitive disorders

T.V. Istomina[1], A.I. Safronov[2], L.Yu. Krivonogov[3], S.A. Karpitskaja[2], M.N. Kramm[4], N.Yu. Kosenok[1], E.A. Shachneva[3]

[1]FGBOU VO «Penza State Technological University», Penza, Russia

[2] «Penza Institute for advanced training of ministry of health of the Russian federation», Penza, Russia,

[3]FGBOU VO «Penza State University», Penza, Russia
[4]NRU «Moscow Power Engineering Institute», Moscow, Russia

Contact istom@mail.ru

Introduction

The analysis of works of domestic and foreign scientists shows that the results of anesthesia frequently, especially for elderly patients, negatively affect the state of cognitive functions in the postoperative period [1]. Therefore, the modern diagnosis of post-operative cognitive dysfunction (POCD) in the early stages, when changes are potentially reversible, and to develop methods for preventive and corrective cerebroprotective therapy on the background of adequate correction of homeostasis acquire important practical significance.

Objective methods for the assessment of violations of cognitive functions available to the anesthesiologist in everyday practice, does not currently exist. Such methods include electrophysiological assessment of psychomotor functions (the ability to create, save and execute motor program) with the help of stabilography.

As integral characteristics for quantifying the anesthetic component of the operating aggression, the authors propose to use the results of stabilographic studies of the patient in combination with the assessment of his cardiac rhythm, especially with the detection of ventricular extrasystoles (VE). The urgency of the problem of diagnosis is not in doubt due to their high prevalence (more than 62 % of all extrasystoles) and the most important role in the development of sudden cardiac death (SCD), therefore, it is necessary to improve algorithms for the detection of ventricular arrhythmias based on analysis of electrocardiosignals (ECS).

The aim of this work is the search for adequate anesthesia, based on the study of the manifestations of postoperative cognitive dysfunction using the system of «WebMultiMedic» providing a comprehensive assessment of the dynamics stabilographic and electrocardiographic indicators.

Materials and Methods

In result of cooperation authors with LLC «BIOSOFT-M» (Moscow, www.biosoft-m.ru) is developed a unique system of remote multidiagnostic of patients with dysfunctions of the locomotor system during the postoperative period. Technique, implemented in the system allows passing on the empirical, approximate recommendations to the exact values calculated on the basis of multifactorial characteristics of each patient and synchronous recording of the results of complex research of patient by means of computer stabilography, electrocardiography, electromyography, electroencephalography with remote multidiagnostic system «WebMultiMedic» [2, 3]. Rising of the quality of diagnosis is achieved through an integrated synchronous registration, processing and analysis of diagnostic signals of multiple research techniques of body functions as well as through the implementation of remote examination of patients on the basis of mobile data communications via Internet. Force plate, electrocardiograph, electromyograph and electroencephalograph combined on the basis of specialized hardware and software into a single system that performs remote examination of patients outside hospitals or in other places. Authorization of doctor and patient on Web-server is performed automatically by means of the keys that contain identifier codes and licenses for the types of data operations and modes of examination of a patient. Web-server of functional diagnostics implements the infrastructure to support remote communications in online and offline examinations, a set of operations performed by a physician in during the analysis and processing the results of diagnostics, storage of patient data and real-time video communication for remote consultations.

Figure 1

The main software includes the Romberg test, psychological tests, and special research tests designed by original techniques. [4].

The system provides a detailed analysis of the stabilometric parameters and the frequency measurement of heart rate and the amplitude-time parameters of the ECS; performs analysis of heart rate variability, however does not allow to detect ventricular extrasystoles.

Developed an original method of detecting ectopic cardio pulses [5], based on the analysis of the physical nature of the formation of ventricular extrasystoles. Upon detection of ectopic cardio pulses joint processing of the two ECG leads S is performed so that the same QRS-T complexes are mutually compensated. If you experience ectopic complexes the ratio of signals 1 and 2 lead changes, and thus on the signal S appears a surge, which is detected by the threshold device.

One of the variants of implementation of the method is the partitioning of the ECS in each of the leads on the positive and negative components S, and the choice of four weighting factors k1+, k1-, k2+, k2-, so that in the time intervals corresponding to the appearance of the typical complexes, the value of the signal S tends to zero:

$$S = k_1^+ \sum_{i=1}^{N} X_{1i}^+ + k_1^- \sum_{i=1}^{N} X_{1i}^- + k_2^+ \sum_{i=1}^{N} X_{2i}^+ + k_2^- \sum_{i=1}^{N} X_{2i}^-$$

A study of the software implementation of the method showed certain shortcomings:

– not in all cases possible to compensate for typical QRS-T complexes,

– selection of 4 coefficients is complicated and takes a long time.

It is proposed to use the a single factor for what it is expedient for each of the cardiac complex to form mono impulse (monopulse). QRS complexes detection algorithm is based on the ranking procedure MSM (MaxSubMin), performed in a sliding window [6]. This procedure just creates a monopulse signal. MSM procedure is to perform three sequential steps:

finding the maximum value of a discrete reference ECG signal in a sliding size 2s + 1 window;

finding the minimum value of the discrete reference ECG signal in a sliding size 2s + 1 window;

subtracting the minimum value from the maximum value.

Formally MSM procedure is written as follows:

$$y_{\max}(t) = \max(x(t-s),\ x(t-s+1),\ \ldots,\ x(t-1),\ x(t),\ x(t+1),\ \ldots, x(t+s-1),\ x(t+s));$$
$$y_{\min}(t) = \min(x(t-s),\ x(t-s+1),\ \ldots,\ x(t-1),\ x(t),\ x(t+1),\ \ldots, x(t+s-1),\ x(t+s));$$
$$MSM(t) = y_{\max}(t) - y_{\min}(t).$$

Examples of the formation of MSM procedure of monopulse signal and subsequent integration into the sliding window (MSMI) are shown in Figure 2. The blue line represents the input ECG signals, and the red line represents a monopulse signal. Monopulse signal can uniquely detect the QRS complexes in all four cases (ECG signals with high-amplitude T wave, ECG signals with the drift of isoline, ECG signals from motion artifacts, ECG signals with negative QRS complexes).

Figure 3 procedure MSMI window size is 11 samples (s = 5), the size of the integration window 21 samples (frequency for sampling ECG signals fd = 500 samples per second).

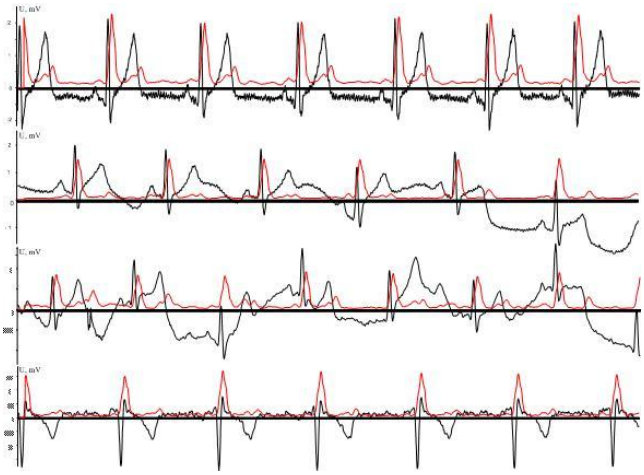

Figure 2

The combination of methods described above allowed to create a method of differential detection of ECG complexes

$$Z(t) = MSMI1(t) - K \cdot MSMI2(t),$$

where K is a tuning factor, which is set at the beginning of the research.

The structure illustrating the proposed method, shown in figure 3.

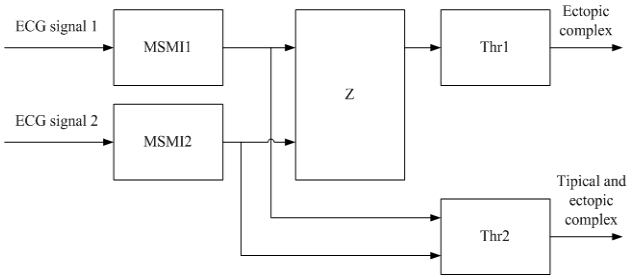

Figure 3

Example of the formation of pulses corresponding to ectopic complexes, shown in figure 4 (output Z).

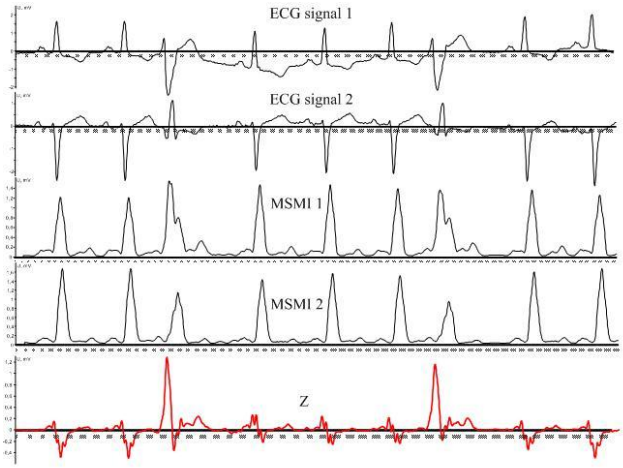

Figure 4

The developed method of differential detection of the QRS complexes is simple and has high performance, it can be implemented in real time. It does not use complex algorithms based on pattern recognition (recognition of many classes with their further classification into normal and ectopic).
Testing the developed method on signals from MIT-BIH Arrhythmia Database showed that the probability of correct detection of QRS complexes (sensitivity), even without pre-filtering is 0,97-0,98.
The application before the procedure MSMI the «hard» filtering with a bandwidth of 2-30 Hz, and the introduction of adaptive threshold improves the probability of correct detection of QRS complexes to 0.99 (when you test on the same signals). The characteristics of detection of ectopic complexes are about the same.
Method recommended for use in the system «WebMulti-Medic» with the aim of improving the quality of ECG-diagnosis.

Results

For analysis of postoperative cognitive dysfunction using stabilographic monitoring of patients operated on for chronic cholecystitis, the study on 29 patients operated at the Penza clinical hospital № 6 named after G. A. Zakharyin.
Studies were conducted with the approval of the Local ethics Committee, and written consent from each patient for the surgery, anesthesia and research.
The choice of patients contingent for the study was determined by the fact that in laparoscopic cholecystectomy a direct impact on the musculoskeletal system is considered to be minimal compared to other interventions, which allows to put the patient on his feet in the first day of the postoperative period.
All patients were divided into 2 groups: group 1 (23 patients in the perioperative period received antioxidant therapy with mafusol and cardioksipin); control group 2 (6 patients, the perioperative period, this therapy was not used).
The surgery was performed under endotracheal anesthesia (a common method of anaesthesia induction and supporting anesthesia with nitrous oxide).
Stabilographic examination of patients was performed before surgery, 24 hours and 48 hours after surgery. The majority of patients were discharged to outpatient treatment within 3-4 days.
In addition to the common in the clinic of the research was determined stabilographic parameters: X is the average position of the center of pressure (CD) on the X-axis (mm); Y – middle position CD along the Y-axis (mm); V – average speed of displacement of the CD (mm/s); S – area of statokinesigram (mm^2) [7] (figure 5).
Revealed the difference of the indices of stabilography: in the control group, the rate of displacement of the center of pressure (V) and area of the stabilogram (S) have a larger spread of values for all modes of study (with open and closed eyes) than in the group of patients who received antioxidant therapy in the perioperative period.

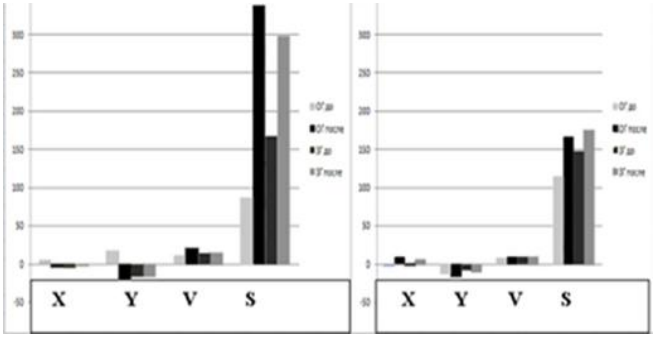

Figure 5

In the course of further studies, we studied in more detail the dynamics of changes in the stabilographic parameters in 120 patients in the perioperative period with laparoscopic cholecystectomy, as a result, a method was patented to reduce the anesthetic risk during laparoscopic cholecystectomy [7].

Discussion

To identify cognitive disorders in clinical practice most commonly used short scale assessment of mental status (MMSE) proposed by M. F. Folsteinи co-authors in 1975 and represents a short questionnaire of 30 items, widely used for the primary assessment of cognitive function and screening of their violations. The diagnostic sensitivity of this technique is not absolute, but is too selective.
Another method for neuropsychological evaluation of cognitive disorders that have a higher sensitivity in comparison with the test ME is MoCA test – the Montreal scale assessment of cognitive disorders (2004) [1].
However, these techniques have a substantial component of subjectivity offer only the qualitative characteristics of the patient.
The sensitivity of the stabilometric method and the quality of information allowed to use this method to determine the current functional state of the patient, the researcher receives information about static and locomotor functions of the patient which cannot be obtained by any other means [8].
In this regard, there is reason to assume that the used during anesthesia medication and other means, affect the static and locomotor functions of the patient and can be measured quantitatively, which may serve as an objective safety criteria conducted anesthesia.
Another important and objective criterion for assessment of postoperative condition of the patient can serve as the parameters characterizing the violation of his heart rate, especially the presence of dangerous ectopic ventricular complexes in the ECS.
Therefore, we believe a promising integrated research stabilographic and cardiological criteria for the assessment of anesthesia that is given undeservedly little attention, by both domestic and foreign researchers.

Conclusions

Thus, the results of the conducted research we can draw the following conclusions.
1. Instrumental method of monitoring based on computerized of stabilography and channel ECG diagnosis system «WebMultiMedic» can serve as a complementary tool of the anesthesiologist in the optimization of General anesthesia in patients during laparoscopic cholecystectomy.
2. The modernization of the ECS channel analysis system «WebMultiMedic», namely, the introduction of differential detector complexes of the ECS, allows high accuracy to detect PVCS and assess the risk of sudden cardiac death.
3. According to the study most informative stabilographic parameters are the velocity of center of pressure on the platform and the area of the stabilogram. It is important that in the control group, the variation rate of displacement of the center of pressure and area of the stabilogram were significantly greater than in the group of patients who received antioxidant therapy in the perioperative period (for all modes of study).
4. The results of these studies quantitatively confirm the feasibility of the use of stabilography as a tool to optimize anesthesiological treatment of patients with laparoscopic cholecystectomy.
5. The research results confirm the feasibility multidiagnostic survey and research of all groups of postoperative patients with a view to detection of postoperative cognitive disorders.

References

[1] Postoperative cognitive dysfunction and the principles of cerebroprotective in modern anesthesiology: a training manual for physicians / ed. by A. M. Ovezova. – Moscow, 2015. – 76 c.

[2] V.V. Istomin, T.V. Istomina, A.V. Kireev and A.I. Safronov, "Methodical software of the system for remote multidiagnostic and rehabilitation of patients after hip replacement," Scient. and Tech. Bull. of the Volga, 1, 113 (2011).

[3] T.V. Istomina, A.V. Kireev, A.I. Safronov, V.V. Istomin and T.V. Karamysheva, Patent for useful model number 122009. Stabilometric simulator, (Russian Federation, 2011).

[4] Istomina T. V., Filatov I. A., Safronov A. I., Istomin V. V., Karpitskaya S. A., and others. Modern equipment for remote Multidiagnostic and rehabilitation of patients with postural deficits // «XXI century: results of the past and challenges of the present plus»: a scientific Periodical. – Penza: Publishing house PenzGTU, 2013. – №09(13). T.1. – C. 64-70.

[5] Patent № 1616600 of the USSR. Detector ventricular extrasystoles / T. V. Istomina, L. Yu. Krivonogov, Yu.V. Polubabkin; publ. 30.12.1990, Newsletter № 48.

[6] Krivonogov L. Yu. System for electrocardiographic diagnosis of critical conditions in terms of the free activity of the patients. Diss. ... Ph. D.: Penza, 2017.

[7] Patent № 2594976 of the RF. A method of reducing anesthetic risk during laparoscopic cholecystectomy» Safronov A. I., Kireev V. A., Vasil'kov V. G., Karpitskaya S. A. egistered in State register of inventions of the Russian Federation of 28 July 2016.

[8] Skvortsov D. V. Stabilometric study: a brief guide / by D. V. Skvortsov, M.: Mask, 2010. — 172 c.

Evaluation of the electrode system pressure force influence on neuro muscular activity signals

A.N. Briko[1], J.A. Chvanova[1], A.V. Kobelev[1], S.I. Shchukin[1]

[1]BMSTU, Baumanskaya 2-ya, 5, Moscow, Russia

Contact: brikoan@mail.ru

Introduction

Full or partial functional loss of upper limb due to amputation or some diseases has a great influence on human ability to do routine tasks.

Active prosthesis and orthosis helps a disabled person to get back after losing the function of a limb. Nowadays there are plenty of different prosthesis for upper and lower limbs. Therefore, an amputee can make a choice according to the desired model's functions and price. Unfortunately, it is more difficult to choose an active orthosis due to limited number of models.

Modern prosthesis and orthosis should correspond to different requirements, such as limb's function substitution and its aesthetic appearance. In particular, active devices with a function of bioelectrical control mostly meet these requirements. It has an external power source and it can be manipulated via biological signals registered by electrode systems.

However, the main disadvantage of using bioelectrical active devices at present is the complexity of their control. Due to the fact that the number of electrode systems is often limited, problems of recognizing precise movements are arising, which leads to the impossibility of using small objects.

Most modern bioelectrical active devices are controlled by signals of surface electromyogram. Such signals of neuromuscular activity, as signals of bioelectrical impedance and myotonic signals, are used in practice much less often. Despite the lower popularity these signals are quite informative, and in some cases may exceed the electromyogram informativity for management tasks.

The aim of the study is to analyze the neuromuscular signals such as electromyogram, bioelectrical impedance and myotonic signals during performing isometric hand grasping with different electrode system pressing force.

Methods

Electromyography

Electromyography (surface) is a non-invasive method for evaluating the activity of skeletal muscle tissue by recording the bioelectric potential. [1]

The advantage of the method is its non-invasiveness and ease of implementation. The disadvantage is the small amplitude and complexity of the interpretation of the signal due to its interference nature, caused by the influence of signals from neighboring muscles.

Myotonic method

The method allows recording the mechanical stresses resulting from muscle contraction. Tension is transferred to the skin, resulting in an effect on the attached sensor. To record these oscillations, special transducers are used: force sensors, accelerometers [2] [3]. The disadvantage of the method is that the signal depends on the sensor pressure of the on the surface of the skin, which can be the cause of the occurrence of artifacts during the action.

Bioimpedance

The bioimpedance signals represent the current level and changes of the impedance of the biological object. The value of tissue impedance $|Z|$ consists of two components: $|Z|=|Zo|+|Z(t)|$, constant - $|Zo|$ and changing over time function - $|z(t)|$. To measure the instantaneous impedance value high frequency alternating current passing through the biological object and the voltage drop is recording on the area. [4,5] The range of alternating current frequencies used in bioimpedance studies is from 1 kHz to 500 kHz, in industrial devices optimum is 30-100 kHz. [4] In experiments was used alternating current with amplitude 1 mA and frequency 100 kHz (at the given frequency the active component of the tissue impedance predominates).

With a muscle contraction, a change in the impedance occurs. The change in such parameters as the thickness of the skin-fat layer, the cross section of muscles, the conductivities and the pressing force of the electrode system lead to a bioimpedance value change during various actions performance. [6]

Research

Experiment

For comparison of different types of biosignals, 4 measurements were made on volunteers with a medium build and an average coverage of the forearm at the place where the electrode system was 34 cm. The signals were recorded using a single electrode system that was located on the surface flexor muscles of the fingers, in place, used to position the electrode systems in modern forearm bioelectric prostheses. Before the installation of the electrode system, the place was scrubbed (by Nuprep Skin Prep Gel) and lubricated with an electrode contact gel (by Geltek Uniagel). An example of the electrode system location is shown in Figure 1.

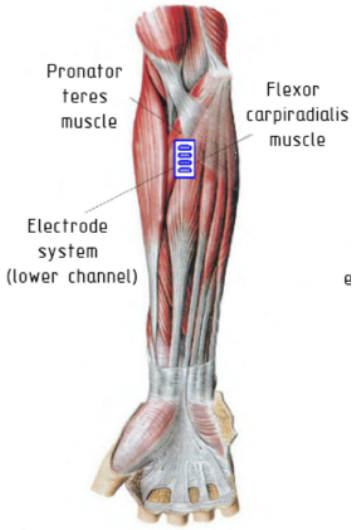

Figure 1: Electrode system placement

The electrode system consisted of reusable electrodes arranged according to the tetrapolar lead-out system (two current electrodes along the edges and two measuring electrodes in the middle) with an inter-electrode distance equal to 10 mm. Such lead system makes it possible to reduce the polarization effect in bioimpedance measurements. The electromyogram was recorded from the same electrode system, from the measuring electrodes. The sampling frequency of the signals was 1 kHz.

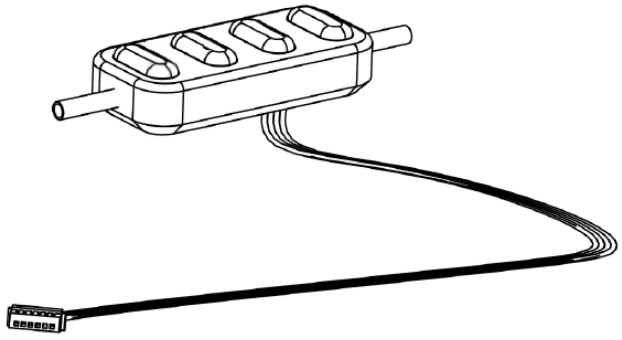

Figure 2: View of electrode system

Myotonic signal was recorded by means of two Honeywell FSG15N1A force sensors (resolution to 1.0g force, maximum overforce 5.5kg, linearity 0.5%, repeatability 0.2%, response time 1ms), which allow recording signals with high accuracy. The force sensors were placed under the electrode system closer to the edges in a special platform in such a way that the electrode system presses on them (Figure 3: 1 - electrode system, 2 - force sensor, 3 - platform, transparent view).

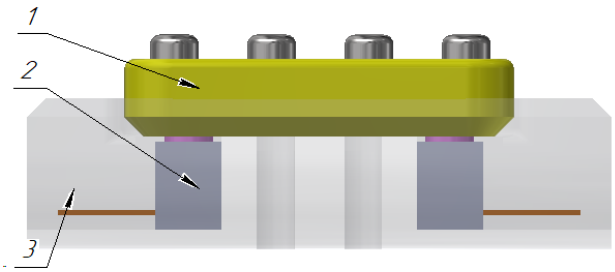

Figure 3: Myotonic signal recording system

During each study, bioimpedance signal, electromyogram and myotonic signal were simultaneously recorded. Network interference was filtered by digital band-stop filter (rejection frequency 50 Hz, 3 dB level on 50±5 Hz, sampling frequency 1 kHz) in recording device. During the experiment, the pressing of the electrode system was successively changed by the control mechanism expanding, a non-stretchable Velcro tape as a belt was used (Figure 4). The mechanism moved apart at a distance of 0cm, 1cm, 2cm.

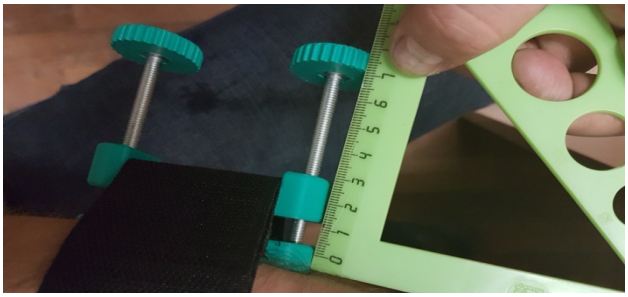

Figure 4: Electrode system pressing control mechanism

To register the force of isometric compression, the special stand was designed (Figure 5: 1,2 - handles, 3 – guideways, 4 - force sensor), which included two parallel force sensors based on the tensoresistors arranged according to the Winston bridge scheme (resolution to 50g force, maximum overforce 20kg, repeatability 0.2%, response time 1ms). The time of each study from the series was 1 minute, during which the following actions were performed: 0-5s - the volunteer does not compress the stand (state without load), 5-10s - the volunteer compresses the stand (load state). The compression force increased iteratively in the framework of one study. During the experiment, the brush was located in a neutral position (between pronation and supination).

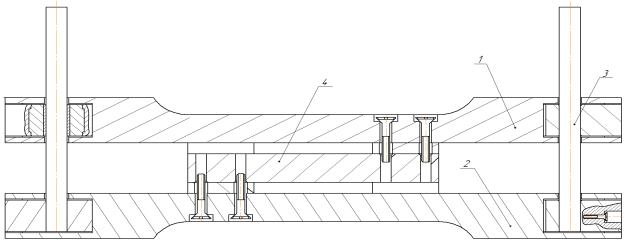

Figure 5: Isometric hand grasp force measuring stand

The force sensors were calibrated by installing laboratory weights of 10 g to 2.5 kg to the center of the electrode system assembled with the platform and to the center of the stand handle. Thanks to the use of two sensors in each case, it became possible to detect skews, however, when conducting studies, skews were not observed and the skew data were not presented in the work. Thus, the average values of the ADC from two sensors were recorded in the experiment and recalculated into force values (daN).

A sample of the recorded signals during one set of measurements depending on the different degrees of compression (which was realized by sliding mechanism) over a particular period of time is shown on Figure 6. An unprocessed electromyogram signal is difficult to analyze. Therefore, it was processed by moving average method with a window length equaled to 100 ms and filtered by a digital Equiripple FIR low pass filter with a cutoff frequency 5 Hz.[8]

Based on the data obtained, a regression analysis was performed, based on which regression curves were plotted with a confidence interval of 95% (Figure 7). As a result of the regression analysis and a least-squares analysis it was obtained, that a straight line is the most accurate for an experimental data interpretation.

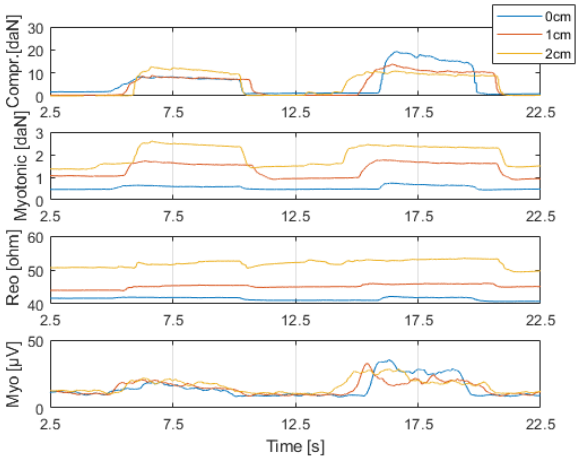

Figure 6: A sample of the recorded signals during one set of measurements

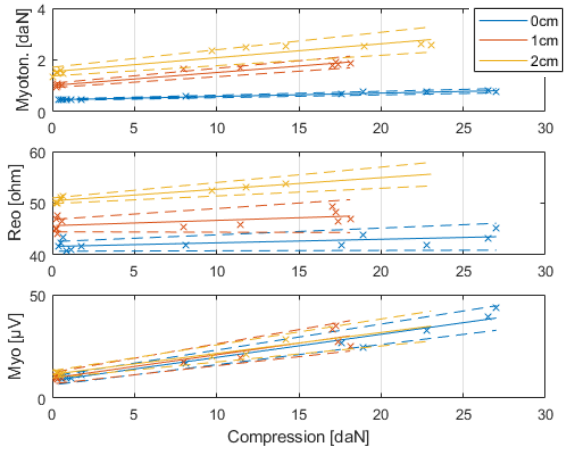

Figure 7: Regression curves with confidence intervals of 95%, based on experimental data

Dependences of regression lines parameters on the electrode system pressure for myotonic signal are shown on Figure 8, Figure 9. Similar dependences for electromyogram and bioimpedance signals are not shown due to its less informative.

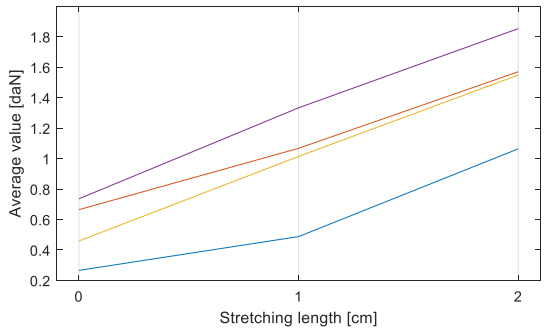

Figure 8: Dependence of the myotonic signal mean value in the condition without load on the electrode system pressure on skin

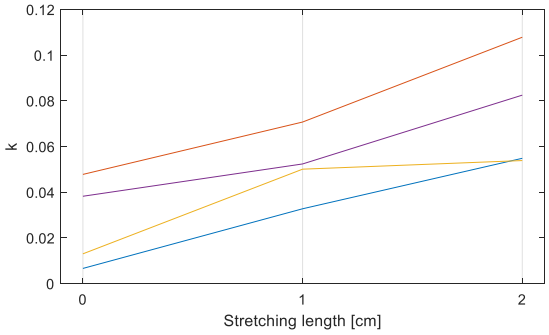

Figure 9: Dependence of the angular coefficient of the regression straight myotonic signal as a function of the electrode system pressing on skin

Discussion

To conduct the investigation, the special stand for measuring isometric hand grasping force with a mechanism for controlling the electrode system pressing force was designed.

Because of using two tension sensors, the grasping force was measured more accurately with an error less than 100g. Moreover, it is possible now to register system imbalances. Guideways usage makes it possible to customize the stand for functioning with different grasping degree.

In spite of widely spread electromyogram usage as a control signal in bioelectrical devices, it was observed, that myotonic method was not less informative type of signal and it could be used as an alternative. The disadvantages of the method are electrode system thickness increase due to force sensor addition and calibration necessity in case of particular force value measurements. Because of myotonic method it is also possible to regulate the electrode system pressure on skin.

Conclusions

As a result of the conducted investigation it can be concluded, that myotonic method is the most accurate among described neuromuscular registering methods. Due to the electrode system pressure on skin increase, signal huge increment was observed with the same grasping force change. However, myotonic signal scatter and amplitude mean value also were increased in the condition without load.

Also, it was determined that increase of electrode system pressure on skin didn't have huge influence on the electromyography and bioelectrical impedance signals. In case of electrode system overpressure, imbalances in the system may appear. It causes additional problems in high quality signal registration.

Therefore, the conducted investigation has shown, that electrode system location is not the only factor which must be taken into account while designing bioelectrical control of different devices. Moreover, the problem of necessary contact providing between an electrode system and skin must also be considered because it should not exceed acceptable pressure value.

References

[1] Seward B. Electrical Impedance Myography: Background, Current State, and Future Directions/ Seward B. Rutkove//NIH Public Access, –2010.-C. 1-20.

[2] Barry, D.T., Cole, N.M., 1990. Muscle sounds are emitted at the resonant frequencies of skeletal muscle. IEEE Trans. Biomed. Eng. 37, 525–531

[3] Morufu Olusola Ibitoye. Mechanomyography and muscle function assessment: A review of current state and prospects/ Morufu Olusola Ibitoye, Nur Azah Hamzaid, Jorge M. Zuniga, Ahmad Khairi Abdul Wahab// Clinical Biomechanics. – 2014. –№ 29. –C. 691– 704.

[4] V.I. Polishuk, L.G. Terehova, Technique and methodology rheography and reopletizmography, (Medicine, Moscow, 1983).

[5] R.M. Rangayan, Analysis of biomedical signals, (FIZMATLIT, Moscow, 2007).

[6] T. Zagar and D. Krizaj "Electrical impedance of relaxed and contracted skeletal muscle", Hermann Scharfetter, Robert Merva (Eds.): ICEBI 2007, IFMBE Proceedings 17 (2007).

[7] A.N. Briko, A.V. Kobelev, S.I. Shchukin " Determining committed action type by dual-channel phase rheogram portrait for bioelectric forearm prosthetics", Proceedings of the 12th Russian-German-Conference on Biomedical Engineering (2016).

[8] M.V. Markova, A.N. Briko, A.V. Kobelev, S.I. Shchukin "Evaluation of informative parameters of the EMG signal for controlling of prosthetic arm in real time", Proceedings of the 11th German-Russian-Conference on Biomedical Engineering (2015).

[9] Y.L. Slavucky, Physiological aspects of bioelectric control of prostheses (Medicine, Moscow, 1982).

A Database with face video images of patients with schizophrenic disorders and control healthy group

E.Yu. Latysheva[1], M.N. Pilipenko[1], A.A. Boiko[1], A.V. Samorodov[1]
M.A. Omel`chenko[2], A.O. Rumyantsev[2], A.M. Ivanova[2], D.D. Volovik[2]

[1]Bauman Moscow State Technical University, ul. Baumanskaya 2-ya, 5, Moscow, Russian Federation
[2]Mental Health Research Center, Kashirskoe shosse, 34, Moscow, Russian Federation

Contacts: kat9.lt@gmail.com, mash_id@hotmail.com, boiko_andrew@mail.ru, avs@bmstu.ru
omelchenko-ma@yandex.ru, rum.a.o@mail.ru, ivalenka13@gmail.com, sweetdiii@mail.ru

Introduction

Schizophrenia is characterized by various negative and positive symptoms and specific incremental changes in personality. Negative symptoms are manifested in behavior, especially in facial expressions. Actual problems today are predicting disease course, evaluation of the effectiveness of treatment, and diagnosis of schizophrenia in preclinical stage of the disease. Development of the automated system of analysis will allow us to study flat affect – one of the negative symptoms of schizophrenia. Consequently, automated facial expressions analysis will make progress in addressing actual problems.

In recent works are reported about using an automated approach to the assessment of facial movements by images for tracking disease course and treatment effectiveness [1, 2, 3]. However, most studies aimed at identifying the differences between healthy group and patients.

The result of different studies (in Canada, India, European countries, Iran) was the discovery of specific anomalies of facial expressions in schizophrenia. Interest in such studies has grown significantly during the last 5 years. In Russia, such studies are still very few.

Patients with schizophrenia have specific anomalies such as a low frequency of positive emotions on certain stimuli and typical movements [4, 5].

Materials and Methods

A database of video images of patients with schizophrenic disorders and in the psychosis high-risk state [6] has been being collected in Mental Health Research Center. A database of control healthy group has been being collected in Bauman Moscow State Technical University.

Stimulant material for the study of facial expressions were three demonstration videos, intended to product emotions of sadness and joy, duration is about 4-5 minutes, and questions on the subject of videos. The first video is neutral, the second one is sad and the last one comprises two parts: neutral part and subsequent funny part. After video demonstration respondents are also asked to estimate their emotional state. A person can choose one or more of the following emotions: happiness, delight, sorrow, worry, sadness, fear, indifference, shame and disgust, – or propose his own variant of emotion. For chosen emotions a respondent has to estimate intensity in the range from one (the weakest intensity) to five (the strongest intensity).

The respondents with schizophrenic disorders first read the text, then watch the video and estimate their emotional state. Thus, following steps of our study were recorded: reading the text, watching the video 1, discussion of the video 1, watching the video 2, discussion of the video 2.

Respondents with schizophrenic disorders were recorded at two time points: the first point is on hospitalization, the second point is on discharge from the hospital.

Medical advisers of our research group conducted standard procedures for evaluating the mental state of patients with schizophrenic disorders on various scales: Positive and Negative Symptoms Scale (PANSS), The Scale of Prodromal Symptoms (SOPS), The Hamilton Rating Scale for Depression (HDRS), Scale of side effects assessment (Udvald for Kliniske Undersogelser Side-Effect Rating Scale, UKU).

Before the first video a respondent of control healthy group is asked to fill out a questionnaire on trait anxiety from state-trait anxiety inventory (STAI-40). After the last video a respondent is asked to fill out a questionnaire on state anxiety from STAI-40, Toronto alexithymia scale questionnaire (TAS-26) and gelotophobia, gelotophilia and katagelasticism questionnaire (PhoPhiKat<30>).

During demonstration respondent's facial image is recorded. For recording we use Logitech C922 Pro Stream webcam. Recorded videos has full HD resolution (1 920 x 1 080 pixels) at 30 frames per second. For each respondent a video of about 2 GB have been recorded.

Conditions of registration is limited to the hospital environment. The patient sits at the table in front of the window while recording the video. Lighting in the room is top and diffused. The patient's face is illuminated evenly, there are no shadows.

The patient sits in front of the laptop with a webcam attached to the top of the screen. Distance from person to camera is from 30 to 90 cm. Face takes up 60% of the image.

Participants

Medical advisers of our research group separated patients into two groups according to clinical observation: patients with schizophrenia and patients in the psychosis high-risk state. 13 respondents are with schizophrenia in the age from 17 to 25 (the average age 20 years), duration from 1 to 24 months, the mean duration is 9 months with normal

or corrected vision, exclusion criteria: severe somatic and neurological diseases, hearing impairment, alcohol and drug addiction in the anamnesis. 30 patients are in the psychosis high-risk state (age from 16 to 25 years, the average age 20 years, disease duration from 3 to 96 months, mean duration of the disease 33 months).
20 respondents aged 20 to 25 years from control healthy group are recorded. Among them six persons are women and fourteen persons are men.

Results

Primary processing of the video images data was performed manually with facial action coding system (FACS) [7]. We made annotation of two intervals: watching the video 1 and watching the video 2. Motion acts over the FACS (yawning, swallowing, tremor, tears) are included during the annotation.
Annotation include the list of action units and motion acts and the number of the beginning and the end of the act. The beginning and the end of our intervals are also marked in the annotation. Furthermore, there are asymmetrical action units and motion acts in the annotation.
Annotation is made by two authors of the thesis. To verify the homogeneity of the annotations obtained, we tested the hypothesis that distributions of each action unit belong to the same distribution. To test the hypothesis, we use the Kolmogorov-Smirnov test. The null hypothesis is that the data in two vectors are from the same continuous distribution. We performed a test with a 5% significance level.
We used such features:
– frequency of action unit η is the ratio of the number of action unit per interval to the duration of the interval;
– percentage of action unit π is the ratio of the sum of the durations of the action unit during an interval to the duration of the interval.
The analysis showed that there are no differences with the 5% significance level. Features without differences are showed with «+» in the table, e.g. see tab. 1. Features are grouped according to the area of the face. Furthermore, appearance of asymmetric action units is marked with letters «R» and «L» corresponding to right and left action units, «n/a» means the absence of asymmetry in video images.

Conclusions

Our first estimation confirms the possibility of solving different tasks with this database and its annotation:
1. Study differences between groups of healthy persons and patients with schizophrenia.
2. Study differences between groups of patients with schizophrenia and patients in the psychosis high-risk state.
3. Investigation of the dynamics of mimic manifestations at the beginning and at the end of treatment.
4. Identification of the relationship between the results of psychological scaling and the severity of psychopathological disorders of facial expressions.
5. Development of an automated approach to the evaluation of facial movements for the study of changes in various time points of the course of a mental illness.

Table 1: Verified Action Units

Action Unit	η	π	η R	π R	η L	π L
Up Face Action Units						
au01	+	+	+	+	+	+
au02	+	+	+	+	+	+
au04	+	+	+	+	+	+
au05	+	+	n/a	n/a	n/a	n/a
au06	+	+	+	+	+	+
au07	+	+	+	+	+	+
Middle Face Action Units						
au09	+	+	n/a	n/a	n/a	n/a
au10	+	+	+	+	+	+
Down Face Action Units						
au11	+	+	+	+	+	+
au12	+	+	+	+	+	+
au13	+	+	n/a	n/a	n/a	n/a
au14	+	+	+	+	+	+
au15	+	+	+	+	+	+
au16	+	+	+	+	+	+
au17	+	+	+	+	+	+
au18	+	+	n/a	n/a	n/a	n/a
au20	+	+	n/a	n/a	+	+
au24	+	+	n/a	n/a	n/a	n/a
au25	+	+	n/a	n/a	n/a	n/a
au26	+	+	n/a	n/a	n/a	n/a
au28	+	+	n/a	n/a	n/a	n/a
au31	+	+	n/a	n/a	+	+
au35	+	+	n/a	n/a	n/a	n/a

References

[1] Benson P.J. et al. Simple viewing tests can detect eye movement abnormalities that distinguish schizophrenia cases from controls with exceptional accuracy. Biological psychiatry, 72(9):716-724, 2012.
[2] Hamm J. et al. Dimensional information-theoretic measurement of facial emotion expressions in schizophrenia. Schizophrenia research and treatment, 2014.
[3] Tron T. et al. Automated facial expressions analysis in schizophrenia: A continuous dynamic approach. In International Symposium on Pervasive Computing Paradigms for Mental Health, pages 72-81, Springer International Publishing, 2015.
[4] Tron T. et al. Facial expressions and flat affect in schizophrenia, automatic analysis from depth camera data. In IEEE-EMBS International Conference on Biomedical and Health Informatics (BHI), pages 220-223, IEEE, 2016.
[5] Dudek A. et al. Analysis of facial expressions in patients with schizophrenia, in comparison with a healthy control-case study. Psychiatria Danubina, 29(3):584, 2017.
[6] Fusar-Poli P. et al. The psychotic high-risk state. JAMA Psychiatry, 70(1):107-120, 2013.
[7] Ekman P., Friesen W.V. Facial action coding system, 1977.

Artificial Muscles with the Possibility of Application in Medical Practice

L.P. Ichkitidze*[1,2], S.V. Selishchev[1], A.Yu. Gerasimenko[1,2], N.A. Demidenko[1]

[1]National Research University of Electronic Technology,
Zelenograd, Moscow, 124498 Russian Federation
[2]I.M. Sechenov First Moscow State Medical University,
Moscow, 119991 Russian Federation

*Contact: ichkitidze@bms.zone leo852@inbox.ru

Introduction

Movement reproduction and control in medical practice is an important technological and engineering task. Recently, the development of artificial muscles (AMs), which are in demand in many fields of medicine, has been in focus of medical professionals and engineers. The research in this direction include concerns creating artificial heart muscle patches and sphincter cuffs for different body parts (urethra, anal canal, and lower esophagus). The AMs are widely used as executive mechanisms (actuators) in prostheses, exoskeletons, implanted drug delivery tools, etc. Medical engineers face the problem of designing light, biocompatible, and reliable AMs, which would be safe for humans and characterized by the low power consumption and acceptable operating temperature. In view of the aforesaid, the properties of various materials, including polymers and nanocomposites, promising for fabricating AMs have been studied. One of the fundamental properties of such materials is their high biocompatibility. It is proposed to use mainly electroactive polymers and nanocomposites containing carbon nanotubes (CNTs). The latter deserve much attention, since they are characterized by the combination of the high strength, flexibility, elasticity, and electrical conductivity.

Here, we made a brief literature review of the current state of research and development in the field of AM drives and prototypes and discuss prospects of their application in medical practice.

Artificial Muscles

A. Pneumatic artificial muscles

The McKibben mechanical drive operates by pumping a fluid or gas under pressure into a chamber bounded by a rigid braid [1]. A new-type McKibben muscle uses paraffin as an expandable material, which is heated to a temperature of 95°C. This type of muscles has certain advantages over the liquid type, but is not compact, hard to control, has a high operating temperature, and, thus, inapplicable in medicine.

A pneumatic artificial muscle (PAM) drive offers great potential for prosthetics, since it is characterized by the high power density ($P_m \geq 4$ kW/kg) and exhibit other properties of natural human muscles [2]. A PAM prosthesis provides a torque sufficient for the knee joint in performing the high-energy human motor functions (fast walking, climbing stairs, etc.) and imitating normal gait parameters [3].

The trigger mechanism for a hydraulic artificial muscle (HAM) is similar to that of a PAM, but the HAM has several advantages, e.g., ductility, low weight, easy maintenance, and low cost [4]. The PAMs and HAMs are designed as drives for robotics and various engineering products. Sometimes, they can be used for external strengthening of human limb movement, but are not intended for invasive use as artificial human muscles.

B. Electroactive polymers

Electroactive polymers (EAPs) have some characteristics similar to those of natural muscles. In particular, they are driven by electric pulses [5]. Usually, the EAP materials are divided into two main groups: electronic (activated by the electrostatic field) and ionic (activated by ion transport). The group-I EAPs are high-voltage ($\geq$ 1 kV), develop a low power ($P_m \leq 0.1$ kW/kg), and exhibit the high efficiency (CE $\geq$ 90%). The group-II EAPs are considered to be low-voltage ($\leq$ 5 V) and have high power and low efficiency (CE $\leq$ 20%).

Obviously, the group-I EAP materials are inapplicable for use in artificial muscles (prosthesis and implants) because of the high-voltage breakdown danger. The EAPs contained in ionic polymer composites and metals are promising for creating various medical products, including electroactive AMs, distributed biomimetic nanoactuators, nanoconverters, nanorobots, and nanosensors. They are characterized by the combination of high load force and low electric voltage (1–3 V) [6]. Ion EAPs is, in fact, functional materials for the development of AMs. Their low-voltage power supply ensures the high safety; the polymer surface electrodes made of noble metals (Au, Pd, Pt, etc.) provide the acceptable biocompatibility and make these materials suitable for use in invasive medical implants. For example, the ionic EAP-based AM is designed to fabricate artificial sphincters of the lower esophagus, anal canal, urinary canal urethra, and heart muscle patches [7]. The EAPs based on the elastic ionic polymers and electrodes are immersed in an electrolyte and all parts are encapsulated in an elastic hermetic. Such a system represents an AM prototype and, depending on its characteristics (mechanical, power, and others), can be used in medical practice [8]. However, this direction is still at the stage of intense research and a practical AM prototype for medical applications has not been fabricated yet.

C. Other artificial muscle materials

The most accessible and simplest is a drive in which nylon and polyethylene fibers woven in a certain way (in spiral springs) contract in length and expand in diameter upon heating. Such drives are controlled using the Joule heat induced by the current transmitted through a conductive coating on the filament surface. The attained drive parameters are a volume energy density of 840 kJ/m^3, an energy density per unit mass of $E_m \sim 530$ J/kg, and a power per unit mass of $P_m \sim 1.0$ kW/kg [9]. These values are at a level of the human heart muscle parameters, i.e., $P_m \sim 0.33$ kW/kg. The inexpensive AMs are fabricated from highly oriented nylon threads [10, 11]. A twisted nylon bundle can lift a load exceeding tenfold the load lifted by a human muscle of the same length. An artificial finger has been demonstrated. However, drives of this type are not suitable for use in AMs for invasive prosthetics in a human body because of their strong overheating.

The high performances are typical of niobium nanofibers; specifically, their conductivity is $\sim 3 \cdot 10^6$ S/m, the tensile strength is up to ~ 1 GPa, and the Young's modulus is 20 GPa.

The twisted nanofiber yarn impregnated with a paraffin wax is strained upon heating and can work as a drive [12]. During the transmission of electric current, the wax melts, expands, and unwinds; the yarn drive does a torsion work.

Numerous actuators based on heating and cooling of intermetallic materials employ the shape memory effect. They develop the high powers ($P_m \sim 4$ kW/kg) and are widely used in robotics [13]. However, despite the very high specific powers developed by the shape memory alloys, their elastic strain limit is 4% [14], while the value for the human muscle tissue is about 20%.

The available AM prototypes cannot simultaneously perform complex deformations (bending, contraction, extension, etc.) attributable to natural muscles. Recently, it has been established that a single-layered lattice microstructure of onion epidermal cells in applied electric voltages of 50–1000 V can simultaneously participate in complex deformations [15, 23]. Currently, this research direction is at the initial stage and its future prospects are still obscure.

D. Carbon nanotube-based artificial muscles

The unique mechanical and electrical properties of CNTs make them excellent candidates for application in AMs for medicine.

The CNT airgel, sometimes referred to as frozen smoke is an ultralow-density solid material [16]. Nanotubes in the airgel layers are arranged parallel and form a sort of framing. In high voltages (1–5 kV), the layers are expanded at a straining rate of $3.7 \cdot 10^4$ %/s, which exceeds many times the known values. The advantages of this material are an energy density per unit mass of $E_m \sim 30$ J/kg and an attainable strain stress reduced to the material density of ~ 15 kPa·m^3/kg. In addition, they have a very wide operating temperature range (80–1900 K) and can develop a force that exceeds that developed by natural muscles with the same cross section by a factor of 30. Undoubtedly, the main mechanical, energy, and temperature parameters of the investigated CNT layers are acceptable for creating AMs, but, to use them in practice, it is necessary to solve the problems concerning the high power-supply voltage, encapsulation, and insufficient safety level and biocompatibility.

The biological polymer chitosan (nanocomposite) films saturated with single-walled CNTs (SWCNTs) exhibit a strain of ≤ 5 V under the action of a voltage pulse [17]. The electrothermal generation of mechanical movements, simplicity of controlling, and biocompatibility make these nanomaterials promising for application in AMs. The complication of a nanomaterial composition aimed at increasing its specific conductivity will help significantly reduce an existing SWCNT concentration of 25 wt.% and, consequently, further enhance the safety and biocompatibility of the proposed AMs. Test drives from multi-walled CNTs (MWCNTs) and niobium nanowires were fabricated [18]. The muscular structure matrix used is made of a heat-sensitive paraffin wax. As metal fillers, tungsten or NiTi alloy nanowires are used, which induce the Joule heating of the matrix. The proposed drives have the higher mechanical characteristics as compared with nylon filament-based actuators, but their drawback is the high operating temperature.

A nanocomposite consisting of a nanogel, which contains boric acid, hyaluronic acid, and MWCNT nanowire strands, was used for creating a drive [19]. A MWCNT strand immersed in the nanogel swells and execute a torsion motion due to the internal anion charge variation. Such a drive can be used for implementing torsion movements, is sensitive to glucose, and has the high potential for application in AMs. In addition, such an AM can work as a glucose sensor (in the range of (55–100)·10^{-3} M), which automatically releases the medication when needed.

In a liquid electrolyte, the twisted CNT strands can generate rotational motion and length shortening. Owing to these properties, the novel materials are capable of lifting loads that are heavier than those lifted by a human skeletal muscle of the same size by a factor of 25 [20–22]. To control their operation, low voltages (≤ 5 V) can be used. With these materials, a rotational speed of 590 rpm and a maximum reversible rotation angle of 15000° were attained. The high developed power, fast response, and low supply voltage are positive indicators for creating AMs; however, it remains difficult to convert the rotational motion into other motion forms.

In an electrolyte consisting of KOH in a concentration of 1M, the SWCNTs coated with platinum nanoparticles ensure a desired deformation in low applied electrical voltages (≤ 1.5 V) and currents (≤ 0.08 A) [23]. The proposed principle of generating the mechanical deformation due to the charge redistribution in the electrolyte is promising for the development of AMs, including those for medical applications.

A new-type AM with artificial absorption of a solvent is highly efficient without changing the temperature [24]. Such AMs are driven by rubber swelling in a nonpolar solvent. The calculated CE value is ~16%, which is similar to an CE value of ~20% of the human muscle tissue [25].

Polyhydroxylated fullerene added to the sulfonated polyetherimide matrix increases the ionic conductivity

and this effect can be further enhanced by coating nanotubes with platinum particles [26]. The obtained energy of $E_m \leq 10$ J/kg is lower than the energy $E_m \sim 40$ J/kg generated by a human skeletal muscle [25]. The developed power ($P_m \sim 0.1$ kW/kg) is also lower than a value of $P_m \sim 0.3$ kW/kg of the human heart muscle tissue.

The operational principles of AMs discussed in reviewed works [18–23, 26] are common and analogous to those of natural muscles. These are the redistribution of ions under the action of current pulses in an electrolyte, straining a CNT filament, and plate motion. Therefore, these research directions are promising for creating AMs for use in medicine.

Conclusions

The analysis of available literary data allowed us to draw the following conclusions:

- Artificial muscles operating on the basis of the flow dynamics laws (pneumatics and hydraulics [1–4]) can develop extremely high specific powers ($P_m \geq$ 4kW/kg) and are suitable for robotics and external prosthetics of human limbs. However, it is hard to use them as invasive implants because of their unacceptable energy supply and insufficient biocompatibility.
- The AMs made of electroactive ionic polymers ([1–8]) are characterized by a power of $P_m \sim 1.0$ kW/kg, an energy of $E_m \sim 530$ J/kg, and an efficiency of CE $\leq$ 20 %, which are analogous to the human muscle tissue parameters ($P_m \sim 0.33$ kW/kg, $E_m \sim 39$ J/kg, and CE ~ 20%). However, the structural components used (electrolytes, polymers, electrodes, etc.), high cost, and limited durability of the available AM prototypes do not meet the medical requirements.
- The actuators based on the laws of conversion of the electrical energy into mechanical one (nylon and polyethylene fibers [10,11], niobium nanofibres [12], and shape memory materials [13]) have operating temperatures of $\geq 60°$ C and, certainly, cannot be used in invasive medical implants.
- Carbon nanotubes and their layers immersed in an electrolyte deform in the course of the chemical reaction and generate mechanical movement [18–23, 25], analogously to mammal muscles. To date, the test parameters of an AM artificial muscle prototype are inferior to the natural muscles.

Thus, the intense research and development directed to improving the characteristics of drives based on ionic electroactive polymers and composite nanomaterials containing carbon nanotubes will make it possible to create invasive muscles for medical purposes. Solving the existing problems in this way is claimed by the modern state of medicine and, especially, the need for treating the heart diseases. Now, heart failure is a cause of about 10 million people die around the world and the creation of an artificial muscle as an auxiliary part instead of a damaged heart site will save numerous lives.

References

[1] D. Sangian, S. Naficy, and G. Spinks. Thermally activated paraffin-filled McKibben muscles. Journal of Intelligent Material Systems and Structures, 27(18): 2508–2516, 2016.

[2] G. Waycaster, S. Wu, X. Shen. A pneumatic artificial muscle actuated above-knee prosthesis. Dynamic Systems and Control Conference, 1: 12–15, 2010.

[3] Y. Park, B. Chen, D. Young. Bio-inspired active soft orthotic device for ankle foot pathologies. International Conference on Intelligent Robots and Systems, 2011.

[4] R. Tiwari, M. Meller, K. Wajcs, C. Moses, I. Reveles, E. Garcia. Hydraulic artificial muscles. Journal of Intelligent Material Systems and Structures, 23(3): 301–312, 2012.

[5] F. Carpi, R. Kornbluh, P. Sommer-Larsen and G. Alici. Electroactive polymer actuators as artificial muscles: are they ready for bioinspired applications? Bioinspiration & Biomimetics, 6: 045006 (10 pp), 2011.

[6] V. Palmre, D. Pugal, K. Kim, K. Leang, K. Asaka, A. Aabloo. Nanothorn electrodes for ionic polymer-metal composite artificial muscles. Scientific Reports, 4: 6176 (10 pp), 2014.

[7] M.S. Banik. Electroactive polymer based artificial sphincters and artificial muscle patches. Patent US #7128707.

[8] L. Rasmussen. Electrically driven mechanochemical actuators that can act as artifical muscle. Patent US #7935743.

[9] S. Mirvakili, A. Ravandi, I. Hunter, C. Haines, and et al. Simple and strong: Twisted silver painted nylon artificial muscle actuated by Joule heating. Electroactive Polymer Actuators and Devices, 9056: 905601–10, 2014.

[10] S. Mirvakili, I. Hunter. Multidirectional Artificial Muscles from Nylon. Advanced Materials, 201604734 (7 pp), 2016.

[11] S. Aziz, S. Naficy, J. Foroughi, H. Brown, G. Spinks. Characterisation of torsional actuation in highly twisted yarns and fibres. Polymer Testing, 46: 88–97, 2015.

[12] S. Mirvakili, A. Pazukha, W. Sikkema, C. Sinclair, and et al. Niobium Nanowire Yarns and their Application as Artificial Muscles. Advanced Functional Materials, 23(35): 4311–4316, 2013.

[13] A.P. Kamantsev, A.M. Zhikharev, V.V. Kolodov, E.V. Morozov, S.V. Von Gratovsky, R.A. Antonov, V.G. Shavrov, A.V. Shelyakov. Actuator based on functional material. Patent RU #2539605.

[14] A. Villanueva, C. Smith, S. Priya. Shape memory alloy (sma) actuators and devices including bio-inspired shape memory alloy composite (bismac) actuators. Patent US 20120174571.

[15] C. Chen, W. Shih, P. Chang, H. Lai, and et al. Onion artificial muscles. Applied Physics Letters,106: 183702 (5 pp), 2015.

[16] A. Aliev, J. Oh, M. Kozlov, A. Kuznetsov, and et al. Giant-Stroke, Superelastic Carbon Nanotube Aerogel Muscles. Science, 323(5921): 1575–1578, 2009.

[17] Y. Hu, W. Chen, L. Lu, J. Liu, C. Chang. Electromechanical Actuation with Controllable Motion Based on a Single-Walled Carbon Nanotube and Natural Biopolymer Composite. ACS Nano, 4(6): 3498–3502, 2010.

[18] S. Mirvakili, I. Hunter. Fast Torsional Artificial Muscles from NiTi Twisted Yarns. Appl. Mater. Interfaces, 9(19): 16321–16326, 2017.

[20] J. Lee, S. Ko, C. Kwon, M. Lima, R. Baughman, S. Kim. Carbon Nanotube Yarn-Based Glucose Sensing Artificial Muscle. Small, 12(15): 2085–2091, 2016.

[21] J.A. Lee, Y.T. Kim, G.M. Spinks, D. Suh, X. Lepró, M.D. Lima, R.H. Baughman, S.J. Kim. All solid state carbon

nanotube torsional and tensile artificial muscles. Nano Lett., 14: 2664–2669, 2014.
[22] J. Lee, Y. Kim, G. Spinks, D. Suh, and et al. All-solid-state carbon nanotube torsional and tensile artificial muscles. Nano Letter, 14(5): vol. 14, no. 5, 2664–2669, 2014.
[23] S. Lu, B. Panchapakesan.Hybrid platinum/single-wall carbon nanotube nanowire actuators: metallic artificial muscles. Nanotechnology, 17(3): 888–894, 2006.
[23] M. Lima, M. Hussain , G. Spinks , S. Nafi, and et al. Efficient, Absorption-Powered Artificial Muscles Based on Carbon Nanotube Hybrid Yarns. Small, 11(26): 3113–3118, 2015.
[24] R.K. Josephson. Contraction Dynamics and Power Output of Skeletal Muscle. Annual Review of Physiology, 55: 527–546, 1993.
[25] J. Helmer, K. Hughes. Artificial muscle. Patent US # 3882551.
[26] J. Foroughi, G. Spinks1, G. Wallace, J. Oh, and et al. Torsional Carbon Nanotube Artificial Muscles. Science, 334(6055): 494–497, 2011.

Acknowledgements

The work was carried out with the partial financial support of the project of the Ministry of Education and Science of the Russian Federation (agreement No. 14.578.21.0234, RFMEFI57817X0234).

Optimization of the prophylaxis of critical ischemia of lower extremities on the basis of fuzzy models for assessing the dynamics of the disease

A.V. Bykov [1], N.A. Korenevsky [2], S.A. Parkhomenko [3], I.I. Khripina [2]

[1]Consultative clinic of the BMU "Kursk Regional Clinical Hospital" of the Kursk Oblast Health Committee, 305007, Kursk, Russia

[2]FGBOU VO " Southwest State University", 305040, Kursk, Russia

[3]FGBU "3 A.A. Vishnevsky Central Military Clinical Hospital", 143430, Moscow, Russia

kstu-bmi@yandex.ru

Introduction

Critical ischemia of the lower extremities (KINK) is considered to be one of the serious diseases of the cardiovascular system, leading to disability and even death. One of the ways to struggle this disease is an accurate and timely assessment of the patient's condition and analysis of the dynamics of the pathology under examination with the subsequent choice of prophylaxis and treatment schemes.

The analysis of known evaluation methods of the dynamics of the development of KINK showed that the existing mathematical models do not provide the necessary accuracy of decision making because of the fuzzy representation of the criteria for classifying the different types of dynamics of the disease even at the expert level [1, 2. 3]. The experience in solving the same data structure problems at the Department of Biomedical Engineering of the Southwest State University has shown that achieving moderately good solutions for the medical practice is possible by using methods of synthesis of hybrid fuzzy decision rules aimed at solving problems that are unrepresentable in formal characterization [4, 5]. With this in mind, the aim of the research is to improve the quality of medical care for patients suffering from KINK through the use of hybrid fuzzy models in combination with the fuzzy modification of the theory of measurement of latent variables, allowing to determine the composition of informative signs and rational prophylaxis and treatment schemes under the conditions of the absence of analytical relationships between medical purpose and descriptive criteria [4, 5].

Materials and methods

In accordance with the general methodology of synthesis of hybrid fuzzy decision rules described in [4, 5], the first stage of our study at the expert level, with the use of the Rasch measurement in the field of Item Response Theory, and implementation of the interactive software system RUMM2020, has found that for the evaluation dynamics of the development of KINK it is necessary and satisfactory to use informative signs in the composition: x_1 - prothrombin ratio; x_2 - homocysteine; x_3 - antithrombin; x_4 - activated partial thromboplastin time; x_5 - dimer molecule; x_6 - platelets.

At the second stage of the synthesis, using the informative characteristics of x_i as the basic variables, the membership functions $\mu_{ПД}(x_i)$ are determined positive (in the matter of the tendency towards improvement of the patient's condition) dynamics (class $\omega_{ПД}$) of development of KINK.

At the third stage, aggregation of the membership function in the integration model of confidence assessment in the predicted dynamics of the PDR of the development of the KINK of the following form is performed:

$$PDR(q+1) = PDR(q) + \mu_{\omega_{ПД}}(x_{i+1})[1 - PDR(q)] \quad (1),$$

where q - is the iteration number in the PDR calculation that coincides with the number of the feature being analyzed:

$$PDR(1) = \mu_{\omega_{ПД}}(x_1).$$

In the fourth stage, three classes of dynamics of the development of KINK are defined on the base variable PDR: negative dynamics (class β_o); stable state (class β_c); positive dynamics (β_n) with the corresponding membership functions $\mu_o(PDR)$, $\mu_c(PDR)$ and $\mu_n(PDR)$.

The decision on the patient's belonging to one of the predictable classes of states is determined by the maximum value of the membership function $\mu_\lambda(PDR)$, and the confidence in the classification U_λ is determined by the expression:

$$U_\lambda = \max[\mu_o(PDR),\ \mu_c(PDR),\ \mu_n(PDR)]\ . \quad (2)$$

At the fifth stage of the synthesis, the experts using Delphi technology for each of the identified predicted classes of states identified prevention schemes optimized using the RUMM2020 package. As a result, a table algorithm for selecting the optimal preventive regimens was presented in tab 1.

Table 1. Table algorithm for selecting the optimal preventive regimens

PDR range	Preventive regimen
PDR≤0,4	Cardiomagnyl 100 mg/a day – 6 months Fraxiparine 0,6 s/c №10, then: Vessel due f 2,0 i.m. 2 times a day №20, then 2 tablets 2 times a day – 2 months. Wobenzym 3 tablets 3 times a day – 2 months
0,4<PDR≥0,6	Cardiomagnyl 100 mg/a day – 6 months Vasonit – 1 tablet 2 times a day – 2 months; then Vessel due f 2,0 i.m. 2 times a day
PDR>0,6	Cardiomagnyl 100 mg/a day – 3 months then Vessel due f 2,0 2 tablets 2 times a day for 2 months

The results of mathematical modeling show that the predictive confidence in the correct decision making exceeds 0.9, which is a good result for the investigated class of problems.

Experimental part

Mathematical models and algorithms for the selection of prophylaxis schemes available from the synthesis of hybrid fuzzy decision rules in accordance with the recommendations [4] were tested in the case management of 400 patients of the Kursk Regional Clinical Hospital No. 1 for 5 years. In the course of the experiment, the validity of the work of predictive decision rules (1) and (2) was verified on representative control samples and the results of observations were compared for patients with KINK using traditional treatment regimens described in [1, 2, 3] and using the proposed prevention algorithm (Table 1).

During the verification of the reliability of the decision rules (1) and (2), the calculation of such quality indicators as diagnostic sensitivity, specificity, efficiency and prognostic significance of positive and negative results was carried out.

During the statistical tests it was found that all the quality indicators exceed the value of 0.85, which is a good indicator for prognostic tasks.

In the course of testing the algorithm for selecting preventive regimen, 130 people received traditional treatment regimens [2], and 170 people were treated according to the prevention scheme attached in table algorithm.

During the three-year observations it was established:

1. The use of complex schemes (ver + $\underrightarrow{ae}$), containing antiaggregants, anticlotting agents and fixed-dose combination (Vessel due f) reduces the number of amputations by 65%;
2. Correction of abnormality of hemorheology in 75% of cases provides prophylaxis of severe forms of KINK.
3. 80% of hemostatic system derangements are the key link in the pathogenesis of KINK.

4. 50% of severe forms of KINK against the background of algorithmic therapy of pathological changes in the hemostasis system regress to the lungs that do not require amputation.

5. 60% of the forms of moderate severity of KINK pass into subcritical ischemia against the background of improvement of hemorheology.

The models and algorithm obtained make up the main part of the knowledge base of the decision support system for cardiovascular surgeons and angiologists that is developed at the Southwest State University in cooperation with the Kursk Regional Clinical Hospital No. 1 and A.A. Vishnevsky Central Military Clinical Hospital.

Conclusions

In the course of the research, the mathematical models for predicting the dynamics of the development of critical ischemia of the lower extremities were obtained and an algorithm for selecting the optimal preventive regimens for this disease was synthesized. It was possible to reduce the number of amputation of the lower extremities by 65% using the latter, 75% of the cases had a correction of hemorheology, and in 50% of cases the heavy forms of KINK turn into lighter forms.

The obtained models and algorithm can be implemented both on modern smartphones and tablets, and as part of powerful decision support systems for vascular surgeons and angiologists.

References

1. A method for treating chronic critical ischaemia of lower extremities of different genesis // Patent of the Russian Federation No. 2421221 June 20, 2011 Bul. No. 17 / Lavrenko VA, Nikolaev SB, Bystrova NA, Konoplya A.I.

2. Saveliev VS, Koshkin VM, Karalkin A.V. Pathogenesis and conservative treatment of severe stages of obliterating atherosclerosis of the arteries of the lower extremities: A guide for physicians. - M .: LLC "Medical Information Agency". - 2010. - 216 pp.

3. Vascular surgery. National leadership. Short edition / under. Ed. V.S. Savelieva, A.I. Kirienko. - Moscow: GEOTAR-Media, 2014. - 464 p.

4. Korenevsky NA, Shutkin AN, Gorbatenko SA, Serebrovsky VI Assessment and management of the state of health of students on the basis of hybrid intellectual technologies: monograph, 2016. -Stary Oskol: TNT. -472 p

5. Korenevsky N.A. Use of fuzzy decision logic for medical expert systems // Medical technology. -2015. - №1. - P. 33-35.

Arrhythmia Analysis in a Non-contact cECG Chair using Convolutional Neural Network

A. Pomprapa[1], W. Ahmed[1], A. Stollenwerk[2], S. Kowalewski[2], S. Leonhardt[1]

[1]Chair for Medical Information Technology, RWTH Aachen University, Aachen, Germany
[2]Informatik 11 Embedded Software, RWTH Aachen University, Aachen, Germany
Contact: pomprapa@hia.rwth-aachen.de

Introduction

Arrhythmia is a cardiac-related condition with certain irregular patterns of a heartbeat, caused by abnormal contraction sequence of the heart. The efficiency of blood pumping can significantly be reduced and it may lead to some other life-threatening conditions such as stroke or heart failure in many cases. Arrhythmias can usually be detected by a traditional electrocardiogram (ECG) record so that the electrical activity in the heart can intensively be analyzed. Therefore, the analyses of P wave, QRS complex, T wave, or R-R interval are of great importance. For instance, the increasing amplitude of P wave (> 0.25 mV) indicates right atrial enlargement [1] or the variation in R-R intervals more than 120 ms corresponds to sinus bradycardia (the slow heartbeat of below 60 bpm).

For processing a large volume of ECG signals or big data, various system platforms and algorithms have been implemented for automatic detection and classification of arrhythmias in order to save the cost in healthcare and to optimize medical decisions. Classical classification techniques have been implemented by performing feature extraction and processing further decisions based on the extracted features. Various feature extraction techniques are for example autocorrelation function [2], time-frequency analysis [3], Fourier-transform neural network [4], and wavelet transform [5]. Additionally, a statistical modelling technique has been applied based on Hidden Markov Models (HMM) [6]. The modern technique based on learning algorithms is also applied such as genetic algorithm [7] or least-squares support vector machine (LS-SVM).

In this particular work, the combination of feature extraction and a supervised learning algorithm using a convolutional neural network (CNN) is proposed for the classification of arrhythmia in a non-contact capacitive electrocardiogram (cECG) system, which is set up in a chair for real-time analysis. The system should be able not only to classify every single heartbeat into four different categories i.e. normal (N), left bundle branch block (LBBB), right bundle branch block (RBBB), and premature ventricular contraction (PVC), but also to transfer the data into a cloud storage for further possible batch processing as well as to represent the real-time stream data in a tablet. This work is to demonstrate that cECG signals can be used for predicting cardiac arrhythmias and they can be applied in many clinical scenarios such as for elderlies at home, in a car seat, in a pilot seat, or even in a passenger seat, where medical attention is required. The proposed system should ultimately support industry 4.0 and medicine 4.0 [8], respectively.

Materials and Methods

Hardware Platform

A set of non-contact cECG electrodes and a driven ground plane have been set up in a chair for data acquisition. Two electrodes were symmetrically positioned at the level of a heart with the distance of 15 cm between each other. The size of each electrode was 7.7 cm x 3.7 cm and this resulted in the area of 28.49 cm^2 for one electrode. The distance between electrodes was 14.3 cm. The clothing of a subject functions as a dielectric material, which was surrounded by the active electrodes and the skin of the subject acting as conductive plates. These settings formed capacitive sensing surfaces for monitoring electrical activity of the heart.

The acquired ECG signal was then preprocessed and amplified by an analog filter and an amplifier. The filtered signal was subsequently converted into digital signal by an analog-to-digital (A/D) converter. A computer was used for data processing, classification of arrhythmias, monitoring, and data transmission into a cloud storage. In the scope of this work, an Android application was also programmed for monitoring of vital parameters, cECG signals, and labels of arrhythmias. The overall system platform is shown in Figure 1.

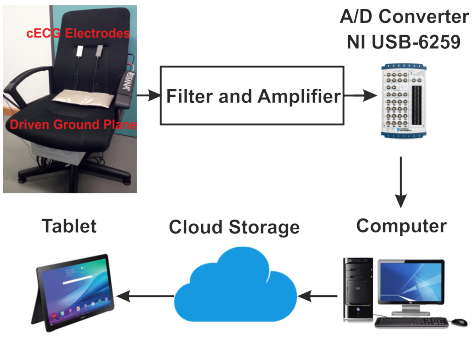

Figure 1: A system platform for arrhythmia analysis.

The personal computer used for this work is based on DELL Intel® Core™ i5-4570 CPU @3.20 GHz, 4 cores with 8 GB random access memory (RAM). The computer is operated under Windows 10. Whilst NEXUS 7 ASUS of quad-core processor is used as a tablet for on-hand data monitoring, where the data are acquired from the cloud storage system.

Software Layers

Python programming language is used for encoding the overall software platform, which consists of three main layers: data layer, processing layer, and diagnostic layer, shown in Figure 2. Since the prediction or classification of arrhythmia is based on a beat-by-beat basis, the cloud storage using InfluxDB database platform is proposed in the data layer for this particular real-time system. InfluxDB developed by InfluxData is an open source database platform for metrics and time series data that is suitable for Internet of Thing (IoT) application and real-time analytics. In this work, a tablet-based application is presented for the data retrieval from the cloud storage and the cECG signals with labels of arrhythmias can be represented on the screen upon request.

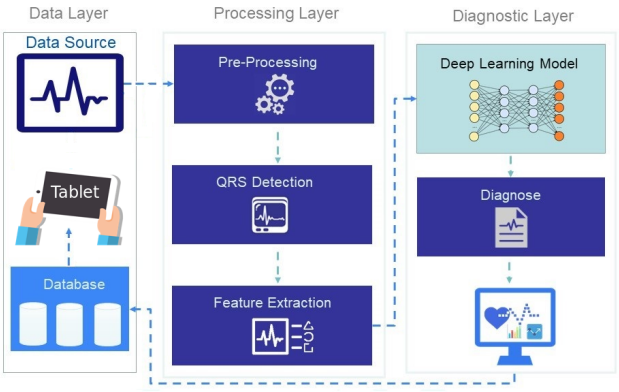

Figure 2: Software layers for real-time processing in arrhythmia analysis.

Once the cECG signal in data layer is acquired from the cECG measurement system, it is transmitted to the next processing layer, where preprocessing and feature extraction are implemented. This layer is a crucial step for the successful prediction of arrhythmia. In processing layer, many processes are implemented, for example, denoising, filtering, normalising, detecting P wave, QRS complex, or T wave, and extracting features (i.e. the amplitude of P wave or R-R interval). Biorthogonal wavelet filter bank has been implemented for specifying the positions of R wave, Q wave, S wave, P wave, and T wave, respectively, so that further feature extraction can be easily implemented. In the last diagnostic layer, a deep learning model based on convolutional neural network (CNN) is designed and trained using Keras (an open source library written with Python and run on top of TensorFlow) from the ECG dataset with the known labels of arrhythmias. The classification is subsequently performed in the diagnostic layer.

Biorthogonal Wavelet Filter Bank

In this article, the discrete wavelet transform was applied to decompose the cECG signals with the main purpose to identify the position of each particular wave, starting from the detection of R wave or the highest amplitude in a cECG beat. Biorthogonal wavelet filter bank is therefore proposed in order to handle the nonstationary cECG signals and to analyse a local area of signals in multiresolution scales. The basic structure of biorthogonal wavelet filter bank is shown in Figure 3. It consists of the following filters.

- Analysis filters that split the input signal into mutually orthogonal subbands (low-pass filter and high-pass filter) and the filtered signals are then downsampled by two.
- Synthesis filters that upsample the input signals and reconstruct the original input signals $x(n)$ by combining both subbands.

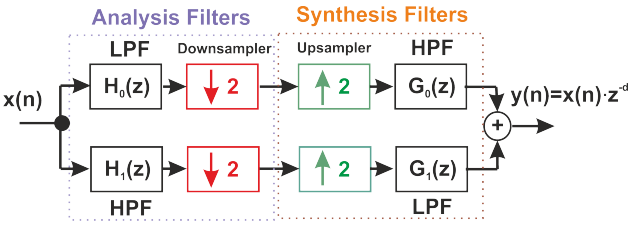

Figure 3: One stage biorthogonal wavelet filter.

There are a number of mother wavelet families that contain energy spectrum concentrated at the low-frequency band similar to the cECG signals. In this study, we use biorthogonal spline wavelet by Mallet pyramid decomposition. These filters are $H_0(z)$ and $H_1(z)$ in the analysis phase and $G_0(z)$ and $G_1(z)$ in the synthesis phase, which are defined by the following equations using Z transforms.

$$H_0(z) = \frac{1}{4} + \frac{3}{4}\cdot z^{-1} + \frac{3}{4}\cdot z^{-2} + \frac{1}{4}\cdot z^{-3} \quad (1)$$

$$H_1(z) = -\frac{1}{4} - \frac{3}{4}\cdot z^{-1} + \frac{3}{4}\cdot z^{-2} + \frac{1}{4}\cdot z^{-3} \quad (2)$$

$$G_0(z) = H_1(-z) = -\frac{1}{4} + \frac{3}{4}\cdot z^{-1} + \frac{3}{4}\cdot z^{-2} - \frac{1}{4}\cdot z^{-3} \quad (3)$$

$$G_1(z) = -H_0(-z) = -\frac{1}{4} + \frac{3}{4}\cdot z^{-1} - \frac{3}{4}\cdot z^{-2} + \frac{1}{4}\cdot z^{-3} \quad (4)$$

These kernels [9] have the structure of symmetric half-band polynomial and an important property of regularity (smooth scaling). For detecting the best position of R peak, further decomposition levels must be chosen by iteration of higher stages of biorthogonal wavelet filter after analysis filter at the low-pass filter (LPF) or the approximation subband, resulting in a tree structure.

Architecture of Deep Learning Model

With the purpose of classification, deep learning model comprises numerous levels of representation by organizing nonlinear modules that transform the representation starting from the raw input into a representation at a higher level with slightly more abstraction [10]. With the sufficient composition of such transformations, the underlying complicated functions can be learned or identified. We typically require supervised learning approach with a huge data set. The MIT-BIH Arrhythmia dataset [11] is therefore used for the model training. It contains 48-h records of 47 subjects. All of the records have two signals, namely modified limb lead II (MLII) and a lead V5, with a 30-min time frame. The sampling rate is 360 samples per second per channel. The deep learning model based on convolutional neural network (CNN) is applied for the classification of arrhythmia, shown in Figure 4.

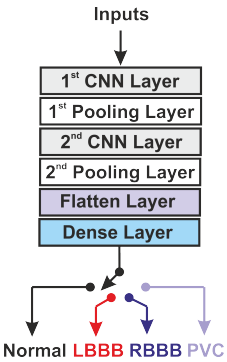

Figure 4: A proposed deep learning model of six layers for the classification of cardiac arrhythmias.

In this particular problem, one-dimensional convolution layer is applied for the beat-by-beat classification. The details of all layers are specified in Table 1.

Table 1: Defined parameters in the deep learning model.

Type	No. of Filters	No. of Parameters
1st CNN Layer	64	256
1st Pooling Layer	64	0
2nd CNN Layer	32	6,176
2nd Pooling Layer	32	0
Flatten Layer	-	0
Dense Layer	-	9,640

The first and the second CNN layers have kernel size of 3. This deep learning model requires the optimisation of overall 16,036 parameters: 256 in the first CNN layer, 6,176 in the second CNN layer and 9,640 in the dense layer. The activation functions in both CNN layers are set to the rectified linear units (ReLU). CNN layers compute the output of neurons. Each CNN layer is directly followed by a pooling layer, which performs a downsampling operation. In flatten layer, it converts the output of convolutional part into one-dimensional feature vector and the final classification is carried out in a dense layer. Both flatten and dense layers utilize softmax activation function. With the proposed model, the batch size of 1,000 samples is used for training the model using categorical cross-entropy loss function and Adam algorithm to optimise the CNN model.

Results

Detection of R-peaks

Based on the physiobank, MIT-BIT Arrhythmia Database [11] is used for selection of typical patterns. Biorthogonal wavelet filter bank is applied up to the fourth scale and the first derivative is carried out for each scale. The extreme values in the first derivative of different scales can then be localised. R-peaks are defined at the zero crossing points between maximum and minimum points of the first derivative curve at the third or the fourth scales. Using this approach, it can identify the onset of R-peaks and some of the results are shown in Figure 5.

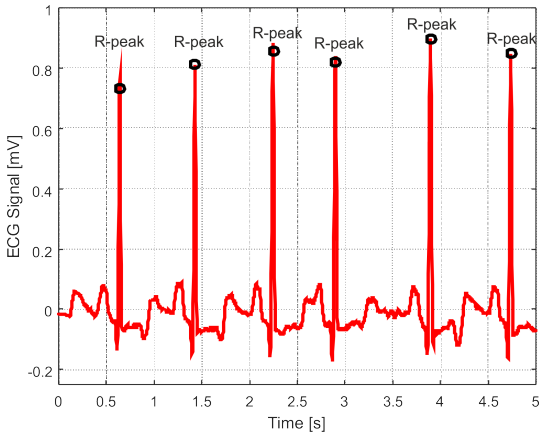

Figure 5: Feature extraction of R-peaks [12].

With similar procedure by defining appropriate window size, the onsets of other waves (i.e. Q waves, S waves, P waves, and T waves, respectively) can be detected and further feature extraction can be implemented such as the amplitude of P waves, R-R intervals, or the heart rate.

Training of the Deep Learning Model

The data of 16,415 ECG records are separated into 67% for the training of this deep learning model and 33% for model validation. The training performance is stable after the 30 iterations or epochs with the best accuracy of 99.2%.

Model Prediction

Based on the validation data of 5,417 records, it consists of the following dataset: 1,648 normal records, 1,308 LBBB records, 1,285 RBBB records, and 1,176 PVC records. The classification performance is summarised in Table 2.

Real-time Detection of Arrhythmias

Grafana is an open platform for analytics and monitoring of time series data. In this work, the dashboards were de-

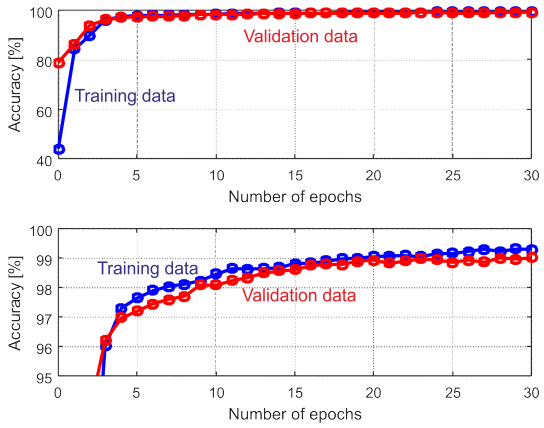

Figure 6: Training performance of the model [12].

Table 2: Classification performance of the CNN model.

	Normal	LBBB	RBBB	PVC	Total
Correct Prediction	1,643	1,302	1,277	1,153	5,375
Accuracy [%]	99.7	99.5	99.4	98.0	99.2

signed to represent the cECG signals with classification based on the trained CNN model. The result of this work is given on the monitor of the personal computer in Figure 7.

Figure 7: Online classification of arrhythmias on a Grafana platform [12].

In addition, an Android application has been implemented to retrieve the dataset from a cloud storage based on a NEXUS 7 ASUS tablet, shown in Figure 8.

Conclusions

Deep learning model of six layers has been applied for the classification of arrhythmias into four main categories, namely normal, left bundle branch block (LBBB), right bundle branch block (RBBB), and premature ventricle contraction (PVC) with the average accuracy of 99.2%. We also demonstrated that the real-time monitoring and classification of arrhythmias can be accomplished using the proposed architecture on a beat-by-beat basis based on a non-contact cECG system with the aid of biorthogonal wavelet filter bank at the fourth level. The classification data was

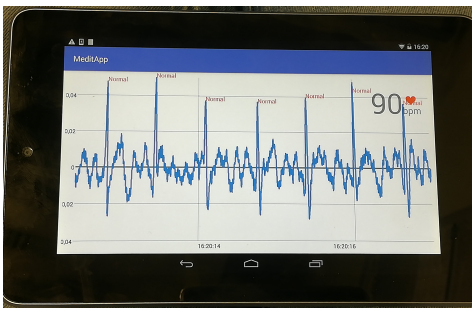

Figure 8: Real-time classification of arrhythmias [12].

directly stored in a cloud storage for evaluating them in real-time as well as in historical records.

References

[1] W.C. Reeves, W. Hallahan, E.J. Schwiter, T.J. Ciotola, E. Buonocore, and W .Davidson. Two-dimensional echocardiographic assessment of electrocardiographic criteria for right atrial enlargement. *Circulation*, 64:387–391, 1981.

[2] S.G. Guillén, M.T. Arredondo, G. Martin, and J.M.F. Corral. Ventricular fibrillation detection by autocorrelation function peak analysis. *J Electrocardiol*, 22 Suppl:253–262, 1989.

[3] V.X. Afonso and W.J. Tompkins. Detecting ventricular fibrillation, selecting the appropriate time-frequency analysis tool for the application. *IEEE Eng. med. Biol. Mag.*, page 152–159, 1995.

[4] K. Minami, H. Nakajima, and T. Toyoshima. Real-time discrimination of ventricular tachyarrhythmia with fourier-transform neural network. *IEEE Trans. Biomed. Eng.*, 46:179–185, 1999.

[5] L. Khadra, A.S. Al-Fahoum, and H. Al-Nashash. Detection of life threatening cardiac arrhythmias using the wavelet transformation. *Med. Biolo. Eng. Comput.*, 35:626–632, 1997.

[6] D.A. Coast, R.M. Stern, C.G. Cano, and S.A. Briller. An approach to cardiac arrhythmia analysis using hidden markov models. *IEEE Trans Biomed Eng*, 37(9):826–836, 1990.

[7] H.A. Guvenir, B. Acar, G. Demiroz, and A. Cekin. Supervised machine learning algorithm for arrhythmia analyis. In *Proceedings of the 24th Annual Meeting on Computers in Cardiology*, pages 433–436, sep 1997.

[8] G. De Micheli. Cyber-Medical systems: Requirements, Components and Design Examples. *IEEE Transactions on Circuits and Systems*, 64(9):2226–2236, 2017.

[9] C. Wang, Y. Lu, and Y. Huang. Using biorthogonal wavelet filter bank for ECG detection and reconstruction. *Beijing Biomedical Engineering*, (1):25–28, 2001.

[10] Y. Lecun, Y. Bengio, and G. Hinton. Deep learning. *Nature*, 512:426–444, 2015.

[11] G.B. Moody and R.G. Mark. The impact of the mit-bih arrhythmia database. *IEEE Eng in Med and Biol*, 20(3):45–50, 2001.

[12] W. Ahmed. Deep learning of cardiac-related conditions using a non-contact multisensor system. Master thesis, RWTH Aachen University, 2018.

Apnea Detection in a Contactless Multisensor System using Deep Learning Algorithm

A. Pomprapa[1], M. S. Sayani[1], T. Anwar[2], A. Stollenwerk[3], S. Kowalewski[3], S. Leonhardt[1]

[1]Chair for Medical Information Technology, RWTH Aachen University, Aachen, Germany
[2]Universiti Teknologi Petronas, Perak, Malaysia
[3]Informatik 11 Embedded Software, RWTH Aachen University, Aachen, Germany
Contact: pomprapa@hia.rwth-aachen.de

Introduction

Obstructive sleep apnea (OSA) is an ordinary breathing disorder, causing a temporary blockage of the upper airway during sleep. It usually stops breathing for 10 seconds or longer and the apnea episodes may regularly happen from 5 to 100 times an hour. The severity criteria can be assessed by Apnea-Hypopnea Index (AHI) or Respiratory Disturbance Index (RDI) in three main categories: mild (5-15 events an hour), moderate (15-30 events an hour), and severe (more than 30 events an hour) [1]. The signs include loud snoring, restless sleep, or daytime sleepiness. If it remains untreated, OSA can lead to many possible serious health complications, such as depression, mood disorders, and heart disease. It can also bring about drowsiness with the uprising risk of accidents while driving and working.

In this work, a prototype of contactless multisensor chair was set up in order to detect vital parameters and a deep learning algorithm based on a hybrid model of convolutional neural network (CNN) and recurrent neural network (RNN) was applied for the detection of apnea in a sitting position, simulated scenarios such as in a pilot seat, in a seat of truck driver or in any types of passenger seat, where a big data can be collected during a flight or a journey, processed in real-time for prewarning or alarms, and transmitted to a cloud storage at a medical center. The main objective of this work is to set up a new software architecture for data acquisition and vital parameter extraction and to demonstrate the integration of deep learning algorithm for the detection of apnea.

To realise this system for the digital lifestyle, a modified λ architecture is proposed with a compromise between real-time processing and restricted computational resources. This software structure offers the benefits not only to a real-time stream processing but also a batch or a large volume of collected data processing. Typically, this approach tries to balance throughput, fault-tolerance, and latency (or time interval) in batch processing.

This contribution is organized as follows. In the section of "Materials and Methods", it begins with a hardware configuration for data acquisition based on multiple devices for the monitoring of heart and lung activities. It also provides a software architecture using λ architecture as well as a deep learning algorithm. The results of our experiments are then given in a subsequent section, namely "Results", followed by a section of "Discussion". The article ends in the last section with the conclusions and future works.

Materials and Methods

Hardware Configuration

A hardware system consists of a number of unique contactless sensors mainly produced in the Chair of Medical Infomation Technology (MedIT), including a magnetic induction (MI) sensor for the monitoring of breathing [2], a cECG system for the monitoring of heart activity [3], a smart photoplethysmography (PPG) [4], ballistocardiography (BCG) [5], and a thermal camera (Seek Thermal Compact) with a micro-USB connector. The additional analog/digital (A/D) converter was set up by using NI USB-6259 as an interface for cECG and BCG measurements with a sampling frequency of 1,000 Hz. All devices are then connected to a FUJITSU desktop computer (Intel® Core™ i5-3470 CPU @3.20 GHz, 4 cores with 14 GB random access memory (RAM)).

Data Flow with System Interface

All signals are acquired through different communication ports and socket. Signal processing and feature extraction were carried out in all channels and passed directly to Kafka producer. The producer consists of a pool of buffer space, which can hold records that have not been transmitted to the server. Apache Kafka is able to handle these big data with very low time interval or latency with a range in milliseconds. The data flow of system interface is shown in Figure 1.

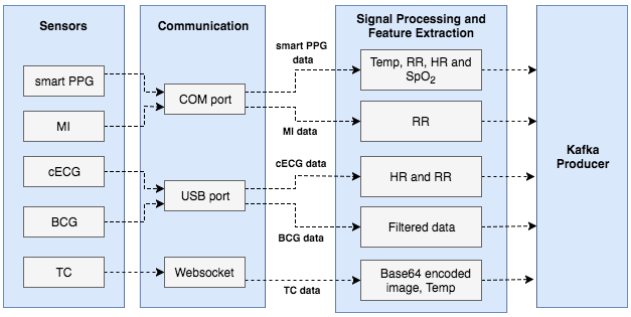

Figure 1: Data flow with system interface in a contactless multisensor system [6].

However, in this article, we mainly focus on the signal acquired from a MI sensor, where respiratory rate (RR) is extracted and the preprocessed signals are used for the detection of apnea.

Software Architecture

To process and analyse big data, the state-of-the-art λ architecture [7] is proposed as demonstrated in Figure 2. The software is programmed by Java programming language for data acquisition. With the proposed architecture, Apache Kafka and Apache Spark worked underground to manage the data in two main layers, namely speed layer and batch layer. The speed layer supports stream processing where fast data is being processed in real-time. While batch layer handles all stored records for batch or large collection processing. The deep learning model can use both data from speed layer and batch layer for apnea detection. With limited computational resources, the full functionality of deep learning algorithm in the batch layer had not been implemented in this work. The visualisation of real-time data and apnea detection was set up using Kibana with the aid of AngularJS, which integrated into a serving layer. In our configuration, Elasticsearch was used as a search engine or a master database in this work.

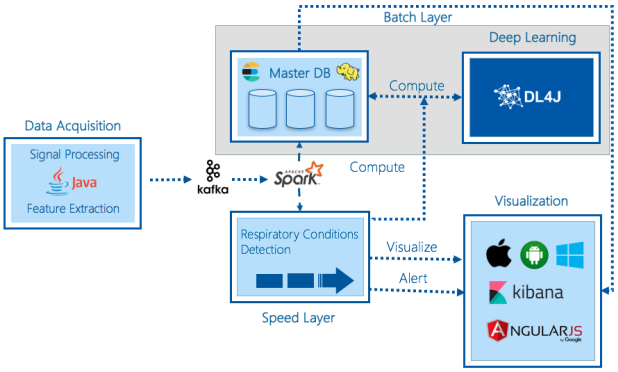

Figure 2: λ architecture for apnea detection using a deep learning algorithm [6].

Deep Learning Model for Apnea Detection

In this work, two different structures of deep learning models have been implemented, namely convolutional neural network (CNN) [8] and a hybrid model of CNN and long short-term memory (LSTM). This was implemented under a Java-based framework using Deeplearning4j, which is a deep learning library for integration, vectorisation, modeling, and evaluation. Since the performance of the hybrid model is significantly better than the proposed CNN model, only the hybrid deep learning model is presented in this article. LSTM can be classified as a recurrent neural network (RNN) [9]. It offers a feedback structure of neural network whilst CNN provides a feedforward neural network. LSTM is explicitly designed to prevent the long-term dependency problem. However, it might have a convergence issue during model training. The designed hybrid deep learning model with 9 layers is given in Figure 3. It contains 3 CNN layers, 3 max subpooling layers, 1 dense layer, 1 LSTM layer and 1 last RNN output layer.

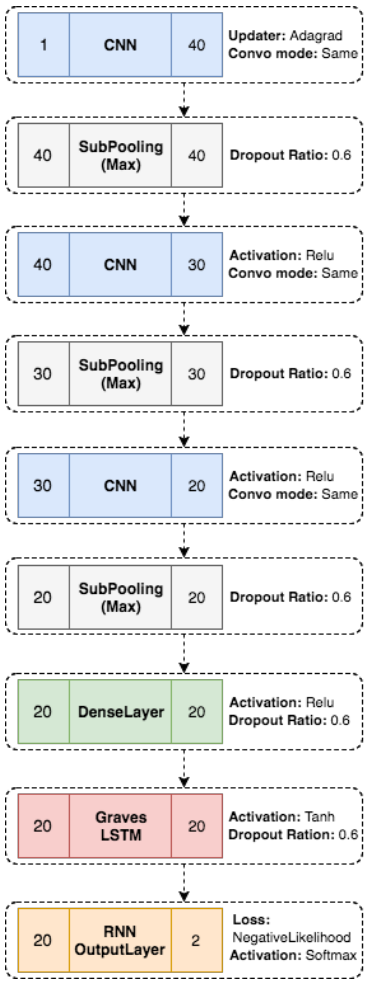

Figure 3: Deep learning model based on the multi-layer hybrid architecture [6].

The MI input signals were divided into chunks of 2,000 points or 20 seconds. The classification was carried out in order to detect normal breathing or apnea from a machine perspective. In this particular system, Xavier weight initialisation method was defined with adaptive gradient algorithm [10] as an update strategy, negative log likelihood as a loss function, softmax activation function in the final RNN output layer with 0.01 learning rate.

The apnea data were collected mainly by a MI sensor from five healthy male subjects at the rest position and they were requested to mimic central apnea by holding their breathing for short periods irregularly. These generated the database of breathing patterns over seven hours. The starting and stopping periods of mimic apnea were labels as used as a supervised learning. 70% of the dataset (976 records) were used for training the deep learning model for detection of

apnea based on the MI sensor and 30% of the dataset (416 records) were applied for validation purpose.

Results

Data Acquisition

The primary signals were acquired from three main sensors i.e. photoplethysmography (PPG) sensor, magnetic induction (MI) sensor, and cECG system. All of these signals can be used for the extraction of respiratory signals [11], [12], [13]. The original signals were acquired and given in Figure 4. These signals can be preprocessed using appropriate filters or techniques for feature extraction. In this work, only a second-order Butterworth bandpass filter was applied to the processing of MI signals. The passband was designed in the range between 0.1 Hz and 1 Hz, corresponding to the breathing frequency of 6 bpm to 60 bpm.

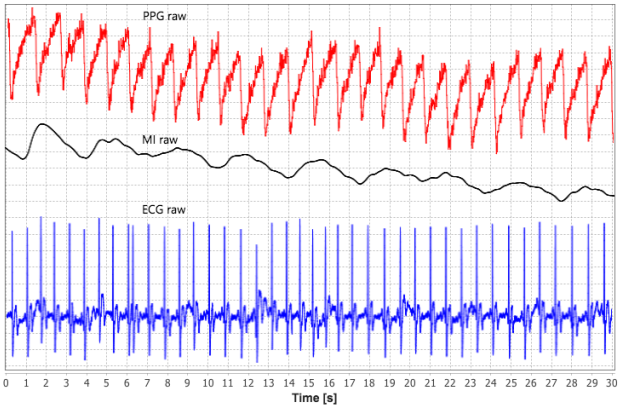

Figure 4: A sample set of primary sensors acquired from MI, cECG, and PPG sensors for 30 s [6].

In this work, a peak detection algorithm was performed in order to estimate the respiratory rate (RR) based on a moving window of 10 s [14]. The estimation of RR was mainly for data representation and this feature was not used for training the hybrid deep learning model.

Training Performance of the Deep Learning Model

The overall 1,392 breathing records were applied for the evaluation of the proposed hybrid deep learning model. Each record contained the breathing data of 20 s. 70% of the dataset was used for training the CNNs and RNNs. The training was performed to update the model parameters, resulting in one cycle or an epoch. The repetitive training was activated one after another to update the new model parameters in order to achieve higher accuracy with no overfitting. In this particular work, the training was carried out for 34 epochs with the highest accuracy of 92% and the performance of the model is shown in Figure 5. The rest 30% of the dataset was utilized for validation purpose and its highest accuracy in the validation dataset was 90% at the 34th epoch. These two datasets were selected randomly.

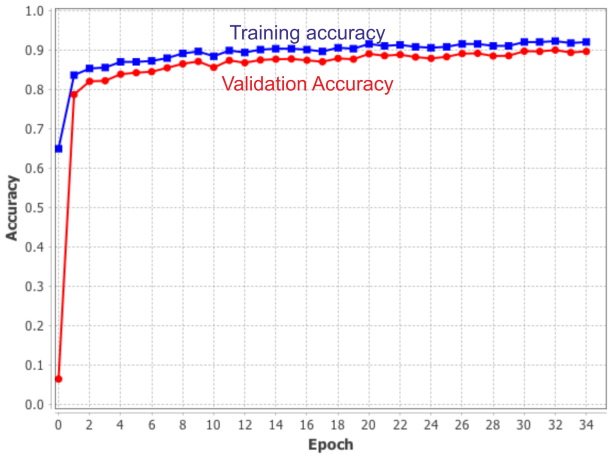

Figure 5: Training performance of the model [6].

Visualisation of Apnea Detection

The data from the speed layer were stored in a database, handled by Elasticsearch. For visualisation of streaming data, Kibana dashboard was designed for real-time visualisation of all acquired signals and AngularJS was used as a platform for building web applications. In Figure 6, the upper curve showed the original MI signal for 60 s, which contained mimic apnea and the respiratory rate of 12 bpm was shown at the top right corner, which was computed based on the peak detection algorithm during feature extraction.

Figure 6: Visualisation of magnetic induction (MI) signal based on Kibana visualisation plugin for Elasticsearch and AngularJS platform [6].

The middle curve in Figure 6 represented a filtered MI signal based on the designed second-order Butterworth filter. The red part is highlighted using Java programming for the detection of apnea episode in real-time processing. Therefore, the system can effectively recognise the mimic apnea and it should be able to detect apnea in various scenarios for

real-time warning and for investigation of historical records in batch processing.

Discussion

Due to the fact that typical respiratory rate for a healthy adult at rest is approximately 12-18 bpm, one breathing cycle thereby takes 3.3-5 s. Since a fixed 20-s window was implemented for the evaluation of apnea episode, 4-6 breaths are contributed to this timeframe. The detection of apnea based on this window size can be activated when the state of stopping breath minimally takes longer than 10 s. In other words, this system can detect apnea whenever there was no breathing cycle for 2-3 breaths. The adjustment of window size may be made for the notification of an apnea episode, however, the proposed window size was reasonable for the implementation of apnea detection.

Because there was no data available for the detection of respiratory patterns using a MI sensor, we, therefore, set up the measurement with a random mimic of apnea and only 1,393 breathing records were acquired and stored in the database. They included normal breathing as well as the mimic apnea. They were used for the training of the proposed deep learning model with the highest accuracy of 92% in the training dataset and 90% in the validation dataset. These accuracies should be improved by collecting a larger quantity of data.

Convolutional neural network (CNN) is a type of feed-forward artificial neural network and is usually applied to two-dimensional signals i.e. images. However, it can also be applied to time series like in this case. While long short-term memory (LSTM) network is a special kind of recurrent neural network (RNN) with a smart dynamical feedback structure to form short memory in the networks. Based on the dataset, the hybrid model of CNN and LSTM provided much better performance for the apnea detection than a CNN model. In this article, the hybrid model was therefore presented.

Conclusions and Future Works

A hybrid deep learning model based on CNN and LSTM has been implemented for the detection of apnea with the dataset measured from 5 healthy volunteers. The highest accuracy was 92% and 90% in the training dataset and in the validation dataset, respectively. With the aid of λ architecture, streaming data and batch data can be processed in real-time and apnea detection can be realised in the proposed contactless multisensor system, which can be used for an immediate alarm or long-term medical diagnostics.

There are many aspects in which this contactless multisensor system can be extended. The following points should be implemented in the future:

1. Classification of apnea into three main categories, namely mild, moderate, and severe
2. Comparison and evaluation of different deep learning models (i.e. CNN, LSTM, and a hybrid model of CNN and LSTM) with other classification algorithms such as random forests, decision trees, or nearest neighbors.
3. Implementation of robust sensor fusion for the detection and classification of apnea.

References

[1] V. Tsara, A. Amfilochiou, M.J. Papagrigorakis, D. Georgopoulos, and E. Liolios. Definition and classification of sleep related breathing disorders in adults. *Hippokratia*, 13(3):187–191, 2009.

[2] D. Teichmann, J. Foussier, J. Jia, S. Leonhardt, and M. Walter. Noncontact monitoring of cardiorespiratory activity by electromagnetic coupling. *IEEE Transactions on Biomedical Engineering*, 60(8):2142–2152, 2013.

[3] B. Eilebrecht, J. Henriques, T. Rocha, M. Walter, S. Paredes, P. de Carvalho, M. Czaplik, and S. Leonhardt. Automatic parameter extraction from capacitive ecg measurements. *Cardiovascular Engineering and Technology*, 3(3):319–332, 2012.

[4] D.U. Uguz. Design of a multipurpose photoplethysmography sensor to assist cardiovascular diagnosis. In *Proceedings of the International Student Scientific Conference Poster 2017*, May 2017.

[5] C. Brüser, S. Winter, and S. Leonhardt. Unsupervised heart rate variability estimation from ballistocardiograms. *International Journal of Bioelectromagnetism*, 15(1):1–6, 2013.

[6] M.S. Sayani. Deep learning of respiratory-related conditions using a non-contact multisensor system. Master thesis, RWTH Aachen University, 2018.

[7] N. Marz and J. Warren. *Big Data: Principles and best practices of scalable realtime data systems.* Manning Publications, 2013.

[8] J. Patterson and A. Gibson. *Deep Learning: a practitioner's approach.* O'Reilly Media, Inc., 2017.

[9] S. Hochreiter and J. Schmidhuber. Long short-term memory. *Neural Computation*, 9(8):1735–1780, 1997.

[10] J. Duchi, E. Hazan, and Y. Singer. Adaptive subgradient methods for online learning and stochastic optimization. *Journal of Machine Learning Research*, 12:2121–2159, 2011.

[11] D. Teichmann, A. Kuhn, S. Leonhardt, and M. Walter. The main shirt: A textile-integrated magnetic induction sensor array. *Sensors*, 14:1039–1056, 2014.

[12] R. Ruangsuwana, G. Velikic, and M. Bocko. Methods to extract respiration information from ecg signals. In *IEEE International Conference on Acoustics Speech and Signal Processing*, March 2010.

[13] M.V. Madhav, M.R. Ram, E.H. Krishna, N.R. Komalla, and K.A. Reddy. Estimation of respiratory rate from ecg, bp and ppg signals using empirical mode decomposition. In *IEEE Instrumentation and Measurement Technology Conference*, May 2010.

[14] J. Six, O. Cornelis, and M. Leman. Tarsosdsp, a real-time audio processing framework in java. In *Proceedings of the 53th AES Conference*, 2014.

A Noninvasive Glucose Estimation based on Near Infrared Spectroscopy and Pulse-Echo Ultrasound

S. Nandi[1], Y. Zhan[2], J. Xia[2], T. Singh[1], L. Mastrandrea[3]

[1]Department of Mechanical & Aerospace Engineering, University at Buffalo, Buffalo, USA
[2]Department of Biomedical Engineering, University at Buffalo, Buffalo, USA
[3]School of Medicine & Biomedical Sciences, University at Buffalo, Buffalo, USA
Contact: tsingh@buffalo.edu

Introduction

Management of Diabetes has become a world-wide issue affecting patients of wide age ranges. To avoid diabetes induced complications from hyper and hypo-glycemia, patients need to frequently monitor their blood sugar levels multiple times. However, the most prevalent method of blood glucose monitoring is invasive [1, 2], which is uncomfortable to patients, carries risk of skin infections, and is inconvenient for long-term usage. As has been mentioned in multiple review articles [3,4], the development of a reliable noninvasive glucose meter (NGM) has vast market potential and is urgently needed. Currently, major challenges to overcome in NGM are the low signal to noise ratio and poor accuracy: introduced by variable temperatures and skin surface humidity etc., necessitating additional calibration among individuals [5]. Fortunately, recent studies found that the efficiency of NGM could be significantly improved by integrating multiple sensing techniques [6, 7].

In this study, we combine two technologies: namely the Pulse-Echo Ultrasound (PEU) and Near-Infrared Spectroscopy (NIRS), to measure blood glucose level noninvasively. These technologies are based on the essential properties of light and ultrasound transmission in tissue. For PEU, an ultrasound pulse is generated using an ultrasound pulser and transmitted through the tissue. A smooth metal disk reflects this signal and transmits the sound back to the source where it is detected by a transducer. The echo arrival time is dependent on the speed of sound in the tissue. As the speed of sound now depends on the glucose concentration, the time of arrival of the reflected signal (also referred to as time lag) becomes a proxy variable for glucose concentration [8]. For NIRS, light attenuation in tissue can be expressed as: $F_{out} = F_{in}e^{-\mu_{eff}d}$ where F_{in} & F_{out} are the incident and output light fluencies, $\mu_{eff} = \sqrt{3\mu_a(\mu_a + \mu_s')}$ is the effective attenuation coefficient, μ_s' is the reduced scattering attenuation coefficient and μ_a is the absorption attenuation coefficient [9]. Scattering and absorption varies with glucose concentration for near infrared light [10]. It is also known from Kirill's work that transmitted optical signal intensity decreases when glucose concentration increases [2]. Hence by monitoring attenuation of an optical signal through a tissue, we can potentially determine glucose concentration levels.

Since both these methods use distinct measures (time of arrival and effective optical transmission) to estimate blood glucose level, PEU and NIRS in conjunction provide a reliable method to estimate glucose levels non-invasively. In vitro experiments are done to collect data, two modelling techniques are investigated to estimate glucose levels and resulting prediction results are presented.

Experimental Setup

Figure 1 shows a schematic of the system. For ultrasound detection, the sound wave is detected by a piezoelectric disk whose central frequency is 4.25 MHz (7×0.5 mm R Wire Leads, Steminc). An ultrasound pulser (5055 PR, Panametrics) is connected to disk to generate the ultrasound pulse. An oscilloscope is used to acquire the PEU data (TDS5054 digital phosphor oscilloscope, Tektronix). For the NIRS part: a laser diode of 950 nm is used. The laser diode is controlled by a Laser Diode Combi Controller (ITC510, Thorlabs) which is modulated by a function generator (SDG2042X, Siglent) with a 100 Hz sine wave output. Transmitted near infrared light is detected by a InGaAs Switchable Gain Amplified Detector (PDA10CS, Thorlabs). Glucose solution is contained in a lab made tank (blue block in the schematic) of dimensions $200 \times 100 \times 20$ mm, with a window size of 100×70 mm. The window is covered with plastic membrane whose thickness is 0.3 mm. The laser detector and piezoelectric disk are placed on one side of the tank, whereas the ultrasound reflector for ultrasound and laser diode is placed on the other side. Gel is used to couple the piezoelectric disk to the tank to facilitate efficient acoustic transmission. To reduce system size, the laser output is routed through an optical fiber. During the in-vitro experiments, the tank was filled with serum-glucose solution with a pre-determined glucose concentration and was maintained at a constant $20°C$ temperature. The setup can easily be adapted for in-vivo experiments by switching the arrangements shown in the red dotted boxes.

Data

PEU Dataset

PEU data is collected in the following way. An ultrasound signal is sent from the transducer (from one side of the tank). This signal is reflected back from the other side of the tank and is detected after a specific time interval. This time interval is now dependent on the speed of sound inside the tank medium which in turn is dependent on the glucose concentration inside the tank. Therefore, by ob-

The first two authors contributed equally to this work.

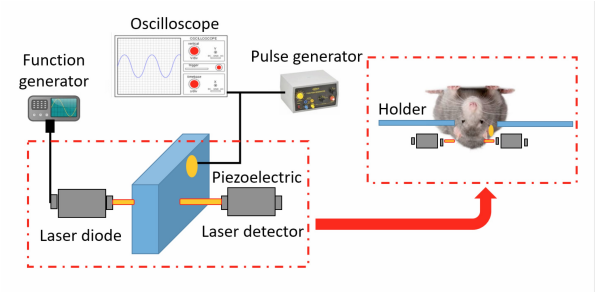

Figure 1: Experimental Setup Schematic

serving the time intervals, it is potentially possible to determine the glucose concentration.
For illustration, 13 different glucose levels were selected at which the time intervals are determined. At each of these glucose levels the experiment was repeated 15 times. By observing the cross correlation data between the emitted signal and the reflected signal, it was possible to determine values of the time lags.
Figure 2 presents the collected data, i.e. the value of the mean time lags at each glucose level. It is evident that there is a clear unique relationship between the glucose level and the time lags.

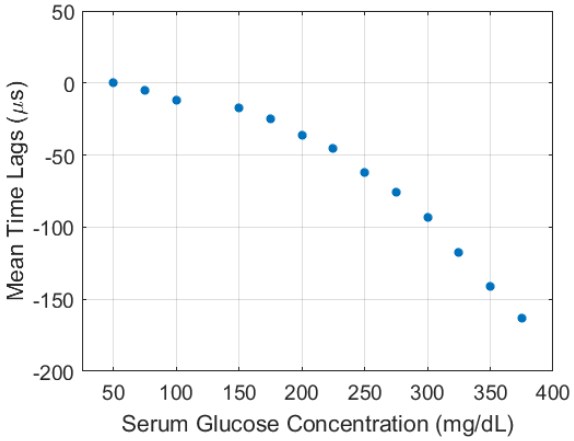

Figure 2: Mean Time Lags vs Glucose Concentration

NIRS dataset

NIRS data was collected in the following way. At each of the glucose concentration levels, an optical signal (with the help of a laser) was emitted from one side of the tank. This signal was then detected at the other end of the tank. Since the attenuation in the detected signal is known to be dependent on the glucose concentration, the RMS value of the attenuated signal can now serve as a modelling parameter for glucose concentration. The collected data has been presented in Figure 3. Once again, we observe a unique relationship between glucose concentrations and the RMS values.
It is interesting to note from Figures 2 and 3 that the two

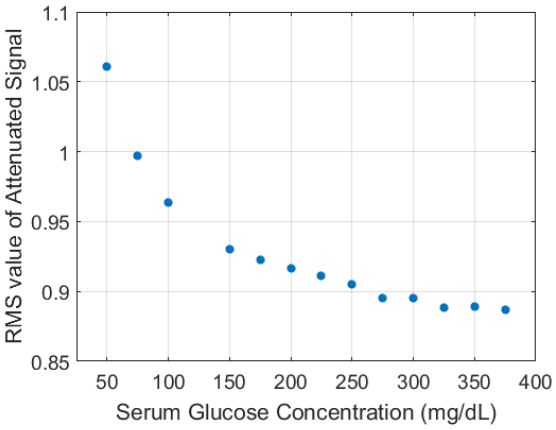

Figure 3: RMS value vs Glucose Concentration

methods PEU and NIRS are most sensitive to different regions of the glucose spectrum. This is evident in the slope of the plots. PEU is seen to be most sensitive in the high glucose region while NIRS is seen to be most sensitive in the low glucose concentration region. In fact, this complementing sensitivity makes these two techniques suitable for combined use. It should be noted that the data for PEU as well as NIRS was collected simultaneously on the same serum samples.

Modelling and Prediction

The in-vitro experiment yielded $N = 13$ data points. This dataset is divided into two groups: namely the training data (S_{train} where $|S_{train}| = n_{train}$) and the testing data (S_{test} where $|S_{test}| = n_{test}$). The idea now is to develop a prediction model using the training dataset and validate its performance on the testing dataset. Note that $n_{train} + n_{test} = N$.
Independent prediction models are developed for PEU and NIRS which estimate the respective glucose levels ($\hat{G}_{PEU}$,$\hat{G}_{NIRS}$) as well as their uncertainties in terms of variances ($\hat{\sigma}^2_{PEU}$,$\hat{\sigma}^2_{NIRS}$). The final glucose estimate ($\hat{G}$) is evaluated simply using an inverse variance weighted technique

$$\hat{G} = \frac{(\hat{\sigma}^2_{PEU})^{-1}\hat{G}_{PEU} + (\hat{\sigma}^2_{NIRS})^{-1}\hat{G}_{NIRS}}{(\hat{\sigma}^2_{PEU})^{-1} + (\hat{\sigma}^2_{NIRS})^{-1}}. \qquad (1)$$

Two modelling techniques have been investigated in this work: Linear Regression and Gaussian Process Model.

Linear Regression Model (LRM)

In this work, a linear regression cubic polynomial model of the form

$$\hat{G}_{PEU/NIRS} = a_0 + a_1 x + a_2 x^2 + a_3 x^3 \qquad (2)$$

is sought where x denotes the independent variable. For PEU, x is the mean time lags and for NIRS is the RMS value of the attenuated signal. For brevity, subsequent development will not include the subscripts $PEU/NIRS$.
The coefficients ($\boldsymbol{a} = [a_0, a_1, a_2, a_3]^T$) are determined by minimizing the sum of squared errors (or residues) in the

dataset S_{train}. The final well known expression is

$$\boldsymbol{a} = (V^T V)^{-1} V^T \boldsymbol{G} \tag{3}$$

where V is the Vandermonde matrix. The i^{th} row of the Vandermonde matrix is given by $V(i,:) = [1, x_i, x_i^2, x_i^3]$ and the i^{th} element of $\boldsymbol{G}$ vector is given by G_i where $(x_i, G_i) \in S_{train}$.
The covariance of the estimated coefficients are then given by $\hat{\sigma}_{\boldsymbol{a}}^2 = s^2 (V^T V)^{-1}$ where $s^2 = \frac{\Sigma_i^{n_{train}} r_i^2}{n_{train} - |\boldsymbol{a}|}$ and r_i is the residue for the i^{th} data point in S_{train}, i.e.

$$r_i = G_i - (a_0 + a_1 x_i + a_2 x_i^2 + a_3 x_i^3). \tag{4}$$

It should be noted that $|.|$ operator represents cardinality and in this case $|\boldsymbol{a}| = 4$.
Finally, the prediction of glucose at an unknown point x_0 can be made simply using the model, i.e.

$$\hat{G}_{PEU/NIRS} = a_0 + a_1 x_0 + a_2 x_0^2 + a_3 x_0^3. \tag{5}$$

The uncertainty in prediction $\hat{\sigma}^2_{PEU/NIRS}$ is given by:

$$\hat{\sigma}^2_{PEU/NIRS} = \boldsymbol{V}_0^T \hat{\sigma}^2_{\boldsymbol{a}} \boldsymbol{V}_0, \tag{6}$$

where $\boldsymbol{V}_0 = [1, x_0, x_0^2, x_0^3]^T$. A prediction $\hat{G}$ at x_0 can now be made by using equation (1).

Gaussian Process

In this method of prediction, it is assumed that the output variable (i.e. glucose concentration in our case) for the training data set (S_{train}) as well as the point at which a prediction is to be made (for example a sample point in S_{test}) are both part of a joint Gaussian probability distribution function. A linear predictor is then designed such that the predicted output ($\hat{G}_{PEU/NIRS}$) is a linear combination of the observations in the training dataset (i.e. $G_i \in S_{train}$).
It can be shown that the predicted output ($\hat{G}_{PEU/NIRS}$) at an unknown point x_0 is given by:

$$\hat{G}_{PEU/NIRS} = \boldsymbol{V}_0^T \hat{\boldsymbol{a}} + \boldsymbol{R}_0^T R^{-1} (\boldsymbol{G} - V\hat{\boldsymbol{a}}) \tag{7}$$

and the associated uncertainty is given by:

$$\hat{\sigma}^2_{PEU/NIRS} = \hat{\sigma}^2_{\hat{\boldsymbol{a}}} (1 - \boldsymbol{R}_0^T R^{-1} \boldsymbol{R}_0 + \boldsymbol{u}_0^T (V^T R^{-1} V)^{-1} \boldsymbol{u}_0), \tag{8}$$

where $\boldsymbol{u}_0 = V^T R^{-1} \boldsymbol{R}_0 - V_0$. $\boldsymbol{G}$, V and $\boldsymbol{V}_0$ are defined as mentioned previously. The matrix $R \in \mathrm{R}^{n_{train} \times n_{train}}$ is introduced to capture spatial correlations between sample points in S_{train}. The elements of R are determined using various spatial correlation kernels studied throughout the Gaussian Process literature. In this work, a squared exponential autocorrelation function kernel was used, i.e. the elements of R were calculated using the relation

$$R_{ij} = e^{-(\frac{x_i - x_j}{l})^2} \tag{9}$$

for all $i = [1 : n_{train}]$ and $j = [1 : n_{train}]$; where R_{ij} represents the i^{th} row j^{th} column element of R, $x_i \in S_{train}$ and $x_j \in S_{train}$ and l is a scale parameter that needs to be determined. The vector $\boldsymbol{R}_0$ whose i^{th} element ($\boldsymbol{R}_0(i)$) is defined through

$$\boldsymbol{R}_0(i) = e^{-(\frac{x_i - x_0}{l})^2} \tag{10}$$

represents the spatial correlation of the training set to x_0.
Before the final expressions (in equations (7) and (8)) can be calculated, the values of $\hat{\boldsymbol{a}}$, $\hat{\sigma}^2_{\hat{\boldsymbol{a}}}$ and parameter l needs to be evaluated. Once again, there are a number of ways outlined in the literature by which they can be determined. The approach used in this work is that of a Maximum Likelihood estimator (MLE). The MLE algorithm can be shown to yield closed form expressions for $\hat{\boldsymbol{a}}$ and $\hat{\sigma}^2_{\hat{\boldsymbol{a}}}$ and an optimization problem to determine l. The results have been presented in equations (11) through (13):

$$\hat{\boldsymbol{a}} = (V^T R^{-1} V)^{-1} V^T R^{-1} \boldsymbol{G} \tag{11}$$

$$\hat{\sigma}^2_{\hat{\boldsymbol{a}}} = (\boldsymbol{G} - V\hat{\boldsymbol{a}})^T R^{-1} (\boldsymbol{G} - V\hat{\boldsymbol{a}}) / n_{train} \tag{12}$$

$$l = arg \ \ min_l \ \ \hat{\sigma}^2_{\hat{\boldsymbol{a}}} (det(R))^{1/n_{train}}. \tag{13}$$

Once the above values are known for PEU and NIRS, a prediction $\hat{G}$ at x_0 can now be made using equations (7), (8) and (1). Details of the Linear Regression method as well as the Gaussian Process prediction can be found in [11].

Results

In this work, n_{train} was selected to be 10 (therefore $n_{test} = 3$). The division of the data points between the two groups was done randomly. Then the datapoints in S_{train} were used for modelling and the models were used to predict the glucose levels at the datapoints in S_{test}. The predicted values were then compared to the true values. Performance of both the prediction algorithms were tested and compared.
Figures 4 and 5 show the PEU and NIRS model developed using linear regression on a sample training set respectively. The red squares bordering the blue circles represent the training set. The black curve denotes the predicted line (or the regression line). The grey band shows a $3-\sigma$ band about the prediction line.

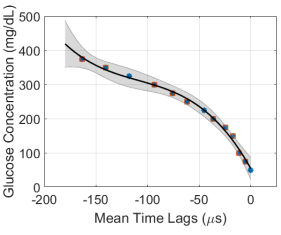

Figure 4: PEU LR Model

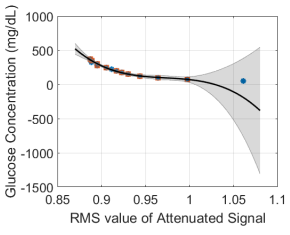

Figure 5: NIRS LR Model

Figure 6 shows the PEU model developed using Gaussian Process modelling on the same sample training set. A similar plot of NIRS Gaussian Process model has been presented in Figure 7. It should be mentioned that the models

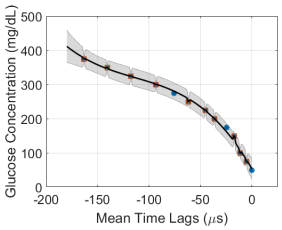

Figure 6: PEU GP Model

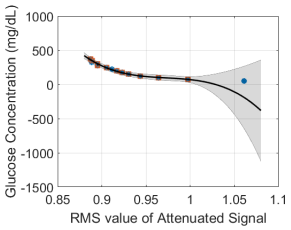

Figure 7: NIRS GP Model

are seen to predict negative values (for NIRS) at the edges. This is primarily due to poor extrapolation capacity of the models and should be ignored.
The linear regression models are then combined (using equation (1)) to predict the glucose levels at the n_{test} points. The same predictions are also made by combining the Gaussian process models. Table 1 lists the corresponding results. Columns 4 and 5 in the table represent the percentage error in prediction from both the methods.

True Glucose	LR	GP	% Var (LR)	% Var (GP)
50	62.25	52.58	24.50	5.16
225	219.64	220.65	2.38	1.93
325	336.59	333.47	3.57	2.61

Table 1: Prediction results from Linear Regression (LR) and Gaussian Process (GP) Modelling

We can see from the table that, in this particular example both the algorithms are successfully able to predict the glucose concentration within an error of $25 mg/dL$.
In order to determine quantitatively which algorithm performs better on average, a Monte Carlo based simulation was done. The division of the data set into the training set and testing set was repeated 1000 times. For each of these cases the prediction errors from Linear Regression and Gaussian Process modelling were recorded. The results were organized into two matrices E_{LR} and E_{GP}. $E_{LR} \in \mathrm{R}^{n_{test} \times 1000}$ where each column represents the Linear Regression prediction error from each Monte Carlo trial. Similarly each column of E_{GP} represents the Gaussian Process model prediction error from each Monte Carlo trial. Finally to compare the two methods, the following metric

$$J_{LR/GP} = \sqrt{\sum_{i}^{n_{test}} \sum_{j}^{1000} E_{LR/GP}(i,j)^2} \qquad (14)$$

was defined to evaluate which algorithm did better on average. $E_{LR/GP}(i,j)$ represents the i^{th} row j^{th} column of the error matrices E_{LR} and E_{GP}. It was found that $J_{LR} = 650.4864$ and $J_{GP} = 452.5926$. Hence, we can conclude from the values that the Gaussian Process model performs better and should be used for all successive predictions.

Conclusions

In this paper, combining two modes of non-invasive glucose concentration sensing to improve accuracy of prediction has been investigated. In-vitro experiments were done to establish that this method is not only possible but could also be potentially state of the art. Two different modelling techniques (Linear Regression and Gaussian Process modelling) are explored and variance weighted data fusion is used to make final predictions. Both methods have shown promise although a Monte Carlo based simulation suggested the Gaussian Process works better on average. This work provides the foundation to go further and perform in-vivo experiments and address the issues associated with that.

References

[1] Sandeep Kumar Vashist. Non-invasive glucose monitoring technology in diabetes management: A review. *Analytica chimica acta*, 750:16–27, 2012.

[2] Kirill V Larin, Mohsen S Eledrisi, Massoud Motamedi, and Rinat O Esenaliev. Noninvasive blood glucose monitoring with optical coherence tomography: a pilot study in human subjects. *Diabetes care*, 25(12):2263–2267, 2002.

[3] Timothy M Dall, Wenya Yang, Pragna Halder, Bo Pang, Marjan Massoudi, Neil Wintfeld, April P Semilla, Jerry Franz, and Paul F Hogan. The economic burden of elevated blood glucose levels in 2012: diagnosed and undiagnosed diabetes, gestational diabetes mellitus, and prediabetes. *Diabetes care*, 37(12):3172–3179, 2014.

[4] Ilana Harman-Boehm, Avner Gal, Alexander M Raykhman, Jeffrey D Zahn, Eugene Naidis, and Yulia Mayzel. Noninvasive glucose monitoring: a novel approach, 2009.

[5] Sandeep Kumar Vashist. Continuous glucose monitoring systems: a review. *Diagnostics*, 3(4):385–412, 2013.

[6] Praful P Pai, Arijit De, and Swapna Banerjee. Accuracy enhancement for noninvasive glucose estimation using dual-wavelength photoacoustic measurements and kernel-based calibration. *IEEE Transactions on Instrumentation and Measurement*, 67(1):126–136, 2018.

[7] Zhihong Gao, Mitsuru Taniwaki, Hiromi Shimada, Sayaka Ishihara, Makoto Nakauma, Takahiro Funami, and Kaoru Kohyama. Ultrasound analysis of the effects of food bolus volume on tongue movement at the initiation of swallowing. *Journal of texture studies*, 44(5):387–396, 2013.

[8] Graham H Thomas, Roger M Watson, and J Oakey Noell. Method and apparatus for non-invasive monitoring of blood glucose, June 9 1992. US Patent 5,119,819.

[9] Omar S Khalil. Spectroscopic and clinical aspects of noninvasive glucose measurements. *clinical chemistry*, 45(2):165–177, 1999.

[10] Praful P Pai, Pradyut K Sanki, and Swapna Banerjee. A photoacoustics based continuous non-invasive blood glucose monitoring system. In *Medical Measurements and Applications (MeMeA), 2015 IEEE International Symposium on*, pages 106–111. IEEE, 2015.

[11] Vincent Dubourg. *Adaptive surrogate models for reliability analysis and reliability-based design optimization*. PhD thesis, Université Blaise Pascal-Clermont-Ferrand II, 2011.

Acknowledgments

This material is based upon work supported by the University at Buffalo: Innovative Micro-Programs Accelerating Collaboration in Themes (IMPACT) program.